Oxygen Consumption in the Nervous System

Suzan Özugur, M. Sc.

Graduate School of
Systemic Neurosciences
LMU Munich

Dissertation der
Graduate School of Systemic Neurosciences
der Ludwig-Maximilians-Universität München

9. November, 2020

Supervisor:
Prof. Dr. Hans Straka
Department Biology II
Ludwig-Maximilians-Universität München

First Reviewer:	Prof. Dr. Hans Straka
Second Reviewer:	PD Dr. Lars Kunz
External Reviewer:	Prof. Dr. Ansgar Büschges

Date of Submission:	09.11.2020
Date of Defense:	25.01.2021

Abstract

Neuronal activity in the brain depends to a large extent on adenosine triphosphate generation and thus on the availability of oxygen. This makes oxygen a highly relevant readout for studying neuronal metabolism. To evaluate the dependency of neuronal activity on oxygen availability, semi-intact *in vitro* preparations of *Xenopus laevis* tadpoles with functional central and peripheral nervous systems were studied. Trochlear motor nerve spike discharge served as a physiological correlate for neuronal activity. O_2-concentrations in the bath chamber and the brain were concurrently monitored using Clark-type oxygen microsensors during superfusion of Ringer solution with various concentration levels of oxygen. The O_2-concentration was accurately set to a defined value by aeration with carbogen (95 % O_2, 5 % CO_2) or nitrogen. In air-saturated Ringer solutions (290 µmol/l O_2), the IVth ventricle was devoid of oxygen due to consumption by adjacent brain tissue and an O_2-concentration of zero was measured. At elevated oxygen bath concentrations of >290 µmol/l, the ventricular oxygen level was considerably augmented (> 0) while spontaneous burst discharge of the trochlear nerve caused a transient drop of the oxygen level within the IVth ventricle, indicating a neuronal activity-related increase in the demand for oxygen. In contrast, decreasing the concentration of oxygen in the Ringer solution below ∼40 µmol/l completely ceased trochlear motor nerve activity. Oxygen delivery is limited by metabolic processes and diffusion, which are often impaired following injury in the brain, largely due to scar tissue formation or caused by associated diseases, such as lung impairments or during stroke. A good model for pathological condition are *in vitro* experiments, as oxygen delivery through the blood is absent. Therefore alternative delivery methods are required. Aiming at a spatially more accurate and faster means for the modulation of the oxygen level in the brain, the natural capability of algae and cyanobacteria to produce oxygen upon visible light illumination via photosynthesis was exploited. Injection of the green algae *Chlamydomonas reinhardtii* or the cyanobacteria *Synechocystis* sp. into the vascular system of *Xenopus* tadpoles prior to the generation of the semi-intact preparation distributed these single celled organisms throughout the vasculature of the entire brain. This new approach is termed 'Symbiotic Oxygen Supply' (SOS). External induction of hypoxia caused an oxygen depletion within the IVth ventricle and a subsequent trochlear motor nerve activity abolishment. Illumination with visible light activated algal photosynthesis and increased the oxygen level in the brain, leading to a restart of motor nerve activity upon illumination within about 20 min. This suggests that SOS is sufficient to restore energy equivalents required for maintained neuronal activity in oxygen depleted environments. Accordingly, introduction of algae or cyanobacteria and illumination represents a promising method to augment the oxygen

level in any diffusion-limited *in vitro* neuronal preparation devoid of a functional circulation and potentially also under *in vivo* conditions.

Aim of this Study

The present study aims at identifying the oxygen dynamics in the brain of *Xenopus laevis* larvae, including the major O_2-consuming pathways in energy metabolism and the contributions to neuronal activity. Further, this study focuses on the quantification of brain O_2-consumption under resting conditions and during increased neuronal activity and monitors the influence of external O_2-concentration on O_2-consumption and neuronal discharge rate. Furthermore, as an alternative oxygen supply, the final aim of this thesis is to test the use of photosynthetically derived oxygen from algae and cyanobacteria as an intrinsic oxygen source in the *Xenopus laevis* larvae.

Contents

1. Neuronal Oxygen Consumption

Pathological conditions such as loss of balance, diabetes, neurodegenerative diseases, or hearing loss often have their cause in disturbances in the energy supply of cells [1–3]. For cells to function properly, it is crucial that every step in energy-deriving pathways work with high accuracy to deliver the required energy for full cell functionality. There exist energy-providing pathways which allow the cell to get energy during short-term shortage, and thus avoid long-term damage associated with such shortage. Such pathways are conserved in all cell types, and thus also in neurons. The brain in particular is very vulnerable to changes in oxygen availability and even minute deviations from an optimal energy supply could restrict cell function and can cause drastic effects on health.

Compared to its fraction of total body mass, the brain requires a disproportionately large amount of energy [4]. This large amount of energy ensures proper maintenance of functional characteristics of the brain's cellular constituents, such as neurons and glial cells [5], which in turn leads to a considerable O_2-consumption by this organ [6]. At the molecular level, oxygen deprivation prevents cells from producing adenosine triphosphate (ATP) and leads to disturbed cell function, which can cause neuronal damage. The major ATP pools in cells derive from oxidative phosphorylation (OXPHOS), the energy cycle located in the mitochondria [7]. As mitochondrial functionality has a great dependency on oxygen availability, it is consequential that the majority of ATP generation is coupled to oxygen availability. This makes oxygen a key molecule in energetic processes. To prevent the cause, or to treat the effect, of energy shortage in the brain, it is necessary to get a full understanding of the influence of oxygen on neuronal activity, how the activity changes during shortage to identify critical events, and possible points of intrusion. An ideal model system to study the fundamentals of energy consumption, energy shortage, and their relation to neuronal activity are vertebrates such as fish or amphibians. These vertebrates have a simpler neuronal organization, and their energy-deriving pathways are well understood, enabling experiments at a very fundamental level.

In the course of the present work the O_2-consumption of the brain and the contribution of oxygen shortage to neuronal activity were investigated. To analyze oxygen dynamics in the brain's fourth-ventricle, mitochondrial activity was inhibited (potassium cyanide (KCN) application) and samples from dead brains (ethanol (EtOH) fixed) were

used. Further, the contribution of neuronal activity to O_2-consumption was quantified following inhibition of neuronal activity by the voltage-dependent sodium channel blocker MS-222, as well as during periods of increased neuronal activity, i.e. spontaneously appearing bursts. The present study shows that air-saturated oxygen levels in the Ringer (a salt solution in water similar to the physiological composition of brain fluids to prolong the survival time of excised brain tissue) are critical and the brain could consume more oxygen provided more oxygen is available. Furthermore, under hypoxia, i.e. oxygen deprivation, neuronal activity ceased completely but could be rescued with externally provided oxygen. However, this process is very slow. In the course of this work, a new approach using algal photosynthesis was established where the preparation becomes independent of external oxygen sources and, moreover, neuronal rescue under hypoxia is faster compared to conventional oxygen supply. Algal photosynthesis was used to produce oxygen upon light illumination. Therefore, algae or cyanobacteria were injected into the vasculature of the larvae to have the micro-oxygen-machinery's spread through the entire vascular system, also reaching the brain. This novel method is termed 'Symbiotic Oxygen Supply', or short 'SOS'. SOS was able to rescue the neuronal activity in *Xenopus laevis* larvae under hypoxia simply by light illumination.

1.1. Hypoxia in the Brain

Like any cell function, also neuronal functionality depends on oxygen. Thereby, the neuronal O_2-consumption can be analyzed as a proxy for energy requirements during specific activity. Since amphibians are quite robust and tolerate low oxygen in the environment, studying their oxygen needs for neuronal functionality allows to draw conclusions for the mammalian system, as neuronal pathways are conserved through vertebrate species. For example, striking parallels between hypoxia tolerant adult animals and mammalian newborns [8] could help to understand compensating mechanisms and to develop strategies to avoid neuronal damage.

Hypoxia is important to study since a hypoxic environment is common among embryonic vertebrates at a distinct stage without negative effects, such as the oxygen poor environment inside the egg. At this early embryonic stage no neurons have developed yet, and will only at a later developmental stage. If hypoxia appears after embryonic stages and as early as at larval, adolescent, or adult stages, long term damage could lead to irreversible neurological damage, and even lead to neuronal death [9]. Causes of hypoxia can be grouped into external or internal origin. Examples for external origin include deep-water diving, flying at high altitudes, and strangulation. Examples for internal origin include smoke inhalation, exposure to toxic chemicals, drug abuse, asthma, stroke,

and shock. Especially in the brain, hypoxia causes severe injuries. Cerebral anoxia occurs when the brain lacks oxygen, leading to neuronal cell death if the oxygen undersupply is prolonged. If there is not a complete anoxic condition, but only an inadequate oxygen supply, Hypoxic Ischemic Encephalopathy (HIE) will occur [10]. The major occurrence of HIE is during birth, when oxygen is limited. This could be due to low maternal blood pressure, hypoventilation, premature separation of placenta, or cord knotting around the neck. As a consequence, organs could be harmed, including some of the most importantly functioning organs such as the heart and the brain. The O_2-concentration in the brain is considered as 'normal' with 95 % - 100 % oxygen saturation, as 'mild and moderate hypoxic' with 86 % - 45 %, and as 'sever hypoxic' below 45 % oxygen saturation [11]. While for mild and moderate hypoxic instances the damage is restricted to the duration of oxygen shortage, under severe hypoxic conditions the damage will be permanent.

In children or adults, the first symptoms indicative of hypoxia of the brain are difficulties in learning tasks and problems in retrieving short-term memory, followed by decreased motor control, or cognitive affections [12]. If oxygen depletion is prolonged, loss of consciousness, coma, and brain death could occur [10]. Depending on the affected region, oxygen depletion in the brain can lead to disturbances throughout the whole body. If on the left side of the brain Broca's area or Wernicke's area are affected by hypoxia, speech and language problems will occur [13]. On the other hand, if the lesion affects the motor cortex, motor control impairments such as Epilepsy could evolve [14]. Finally, if the limbic system is affected by hypoxia, emotions and understanding will be impaired, that could develop further into depression, schizophrenia, Alzheimer's disease, or autism [15].

A treatment of hypoxic brain injuries of newborn infants is cooling the body temperature to 33 °C for three days [16]. Newborn mammals survive lower body temperatures more easily than adults [17]. The reduction of body temperature leads to a reduction in the metabolic rate [8] and therefore decreases the oxygen need. This prevents long-term damage, if the treatment accrues before normal blood flow reaches damaged cells within 6 hours after the hypoxic condition [18]. In adults, however, oxygen levels in the brain need to be restored. This could be achieved, in mild and moderate cases, by removing the cause of the hypoxia and by inhaling oxygen. One method is the hyperbaric oxygen therapy, where patients inhale pure oxygen to increase blood oxygen delivery to the injured tissue. This therapy requires 30 - 40 repeated sessions [19] where patients are hospitalized, which is time and cost expensive. However, in severe hypoxic cases, even those methods are insufficient. This is why new methods and fast applications are required to prevent harmful aftereffects of oxygen depletion in the brain. This requires a fundamental understanding of neuronal circuits and their respective oxygen dependency.

1.2. *In Vivo* vs *In Vitro* Brain Studies on O_2-Consumption

In vivo and *in vitro* studies both come with advantages and disadvantages. While *in vitro* measurements reveal easy and fast experimental data, *in vivo* measurements are the most realistic monitoring for normal function and behavior. However, most *in vivo* brain studies are performed in rodents and require training and most often surgery on the animal before experimentation. On the other hand, *in vitro* brain studies are mainly performed on brain slices and only possible for a short time period after surgery, when the cells are still active.

In vitro measurements are the dominant method when it comes to study the O_2-consumption in the brain. O_2-turnover has been used in a number of experimental and theoretical studies to estimate the cost of neuronal activity from single cell conductance to network computations. Rat hippocampal brain slices showed at air-saturated artificial cerebrospinal fluid (CSF) significantly reduced gamma oscillations, which are linked to sensory perception and memory formation. Moreover, during air-saturated artificial CSF spontaneous network activity is decreased, compared to conditions with increased external oxygen. This was shown in multi- and single-unit recordings, where the strongest decrease of gamma oscillations was reached after 30 min - 60 min of low oxygen in the CSF [20]. Huchzermeyer *et al.* showed that at 20 % O_2-concentration, which corresponds to air-saturated conditions, mitochondrial function is limited [20]. Likewise, in rat hippocampal brain slices, 20 % oxygen saturation was found to be insufficient to activate a maximal nicotinamide adenine dinucleotide (reduced form: NADH) response [21]. Brosel *et al.* studied the oxygen and energy consumption in different brain regions in gerbil slices and showed that the energy demand is dependent on neuronal cell type and thus on a particular brain region [22]. Further, they showed that 80 % of the ATP production is covered by OXPHOS [22]. Monitoring O_2-concentration in the lateral superior olive (an auditory brainstem nucleus) during stimulation with 100 Hz caused an oxygen drop of 129 µmol/l. As the stimulation with 10 Hz lead to an oxygen drop of 8 µmol/l, this showed a strong stimulus dependent O_2-consumption [22]. Setting the excitatory postsynaptic potential (EPSP) amplitude in relation to O_2-consumption, Galeffi *et al.* measured in rat hippocampal slices that a 90 s lasting activation at 10 Hz results in an oxygen drop of 200 mmHg, while for the same stimulation for 25 s the oxygen drop was only 120 mmHg [23], which, following Schneider *et al.* [24], corresponds to 273 µmol/l and 88 µmol/l, respectively. In the mouse hippocampal CA3 region, oxygen monitoring yielded to an O_2-consumption of 145 µmol/l during the resting state and an additional oxygen need of 245 µmol/l due to increased neuronal activity (calculated from [24, 25]).

The key message from the studies above is that the O_2-concentration in the Ringer has an impact on mitochondrial function and spontaneous network activity, which is also dependent on the brain region. Air-saturated external Ringer levels are too low to achieve maximal energy production and neuronal response.

The different approaches in oxygen monitoring make it hard to compare values or set them into relation to other studies. However, studies using brain slices yield an important insight at the cellular level. Patch-clamp recordings allowed analyzing the response and dynamics of single cells due to stimulation or drug application. Drug application in slices is simple and fast, such that the latency time is easily determined. Further, the washout is fast and efficient as the slice is thin. Studies with reversible inhibitor application are beneficial on brain slices. Mathematical models can be applied to single cell studies and their results allow to draw conclusions that are also valid for cell types, such as neurons or glial cells, for vascular interactions and feedback [26], or contribution of the energy pathways underlying nicotinamide adenine dinucleotide phosphate [NADP(H)] production [27]. However, slice recordings are in some aspects far away from *in vivo* physiology, because in slice recordings cells are remote from a natural environment, lacking blood circulation and thus the supply of nutrients and oxygen. This is why in slice studies everything is limited through diffusion processes. Reduction of the slice thickness helps to guarantee diffusion in adequate time. However, the thinner the brain tissue the less natural is the environment in which the cells are embedded, especially on the surface. Cells on the surface of the slice have a high nutrient supply, that under normal conditions would be absent. This could stress the cells and lead to production of stress factors, which cells in the vicinity would detect and react to. Further, cells on the surface are most probably damaged by the slicing procedure and show round and detached structures, that also most likely lead to a production of stress or death signals, which influence neighboring cells. Additionally, the introduction of measurement instruments into the tissue of a slice will unavoidably damage cells at the insertion site.

On the other hand, studies on *in vivo* models such as rodents or humans are difficult to perform and *in vivo* collected data are often difficult to interpret, due to the special circumstances of the experiment and the therefore small field of application. Animal *in vivo* experiments take a long pre-experimental time to set up the whole procedure. Further, the experimental procedures are very sensitive and have to be performed in exactly the same way for every animal in a study. The data collected from an *in vivo* experiment could range from behavioral studies to cell and network influences and has almost no limitation. However, the animal most likely has to undergo surgery before the experiment, allowing monitoring of fluorescent dyes in the brain through a cranial window or electrode placement within the brain with head fixation on e.g. a treadmill.

This intervention is difficult and often very stressful for the animal, which will probably never fully recover from this intrusion, thus not showing the normal behavior.

Since measurements in slices are hardly comparable to *in vivo* or *in vitro* whole brain preparations and *in vivo* data collection is complex and expensive, studies in an intact system would be beneficial. Additionally, studying an intact system—such as in semi-intact *in vitro* preparations including the brain—allows making assumptions for human physiology, since the brain and the central neural network is still intact, which is not the case for slice experiments, where only a distinct mechanism or cycle can be monitored but without the interaction of the whole neuronal network in the brain. Furthermore, slice studies in the past used electrical stimulation to provoke a specific neuronal response, which is hard to compare to natural stimuli. Action potentials in slices were recorded extracellularly [24] or by local field potentials and changes in extracellular potassium concentration were monitored [20]. Motor nerve activity as a behavioral readout was not recorded, as this is not possible in slice recordings. However, the potential of nerve responses and thus behavioral readouts in an experiment is not to be underestimated. Especially when correlating the magnitude of neuronal discharge and concurrent oxygen consumption in the intact brain. In an intact *in vitro* preparation, natural stimulation and motor nerve activity can be monitored simultaneously. Furthermore, the O_2-consumption of a distinct neuron or neuronal population is crucial to estimate the neuronal dynamics on a cellular basis. However, in order to get an idea of how neuronal activation accounts for oxygen dynamics, it is necessary to study the oxygen dependency in an intact brain, such as present in semi-intact *in vitro* preparations.

1.3. *Xenopus laevis* as an Animal Model

As mentioned in the very beginning of this chapter, vertebrates such as fish and amphibians are ideal candidates for studying oxygen dynamics in the brain. The importance of studying different species besides mammals is due to the fact that these vertebrates have a simpler organization such that it is much easier to access neuronal pathways. However, among vertebrates, amphibians earn special notice for several reasons. Amphibians are truly experts in survival in regard to temperature changes, tolerance for low oxygen, and extreme environmental changes, such as changing their habitats from water to land. Further, amphibians undergo metamorphosis, a physiological change that is associated with organogenesis or tissue differentiation and could give important insights into evolutionary steps [28].

Among these amphibians is the African clawed frog—*Xenopus laevis*—that is used in research in several fields, including neurobiology. In 2012, Straka and Simmers described

the advantages of semi-intact *in vitro* preparations of *Xenopus laevis* with functional sensory organs and motor effectors [29]. These semi-intact *in vitro* preparations allow filling the gap between *in vitro* slice recordings and *in vivo* experiments. They remain (almost) fully functional up to 5 days [30], allowing longer recordings. Temperature adaptation is quite unique in amphibians and show no influence on viability between 2 °C and 26 °C [30]. The ability to perform a range of *in vitro* experiments with this semi-intact preparation enables studies that in other vertebrate models can only be performed *in vivo* [29]. Since the preparation gives access to all brain areas, the semi-intact *Xenopus laevis in vitro* preparation is a powerful model to study central neural networks and their development, as well as the functional establishment of sensory-motor transformations [29]. This preparation shows a robust and intact vestibulo-ocular reflex and functional sensory motor behavior [31], thus enabling to study the transformation of vestibular sensory signals into motor commands for gaze-stabilization [32]. The activation of the vestibulo-ocular reflex can be triggered by angular or linear motion, which activates semicircular canal and otolith organs in corresponding alignment [33]. A wide variety of *Xenopus laevis* neuronal projections have been investigated in the past [31, 33–38] and show a well organized network. Vestibular nuclei, located in the hindbrain, are activated by semicircular canals, the utricle, the lagena, and the saccule. Efferent fibers connect the vestibular nuclei with the extraocular motor nuclei, i.e. the abducens, the trochlear and the oculomotor nuclei. The abducens nerve is involved in lateral eye movements, through contractions of the lateral rectus eye muscles. The trochlear nerve innervates the superior oblique muscle that causes an upward rotation of the eyes. The oculomotor nerve innervates superior- (upward eye motion), medial- (nasal eye motion), and inferior rectus muscles (downward eye motion), and inferior oblique muscles (downward eye rotation) [31]. These spatially selective motor commands can be used to analyze the structure and network of the brain [31, 34], or the extraocular motor activity available as readout during imposed head motion [39], or during swimming behavior [40]. Nerve activity can be monitored easily by recording nerve discharge rates, through methods such as intracellular (singe cell) recordings with patch-clamp [41] or extracellular (single- and multi-unit) with hook-techniques [42] or suction electrodes [43]. All approaches have their advantages and depend on the specific research goal. For oculomotor nerve recordings, the hook- and suction electrode method is applicable. Since *Xenopus laevis* larvae undergo metamorphosis, they represent an important model, as their neuronal circuitry has to adapt to the new locomotor style. This functional plasticity during development was studied by Combes *et al.* [44], where they showed that during metamorphosis a switch in locomotor network from axial locomotion to appendicular rhythm generation occurs. Furthermore, electrophysiological recordings, such as action potential recordings from the extraocular motor nerves, allow

the functional structure of circuits to be assessed. Further, it allows the study of synaptic inputs [30], triggered by stimulation or inhibition (translational motion stimulation [45] or drug application [46]).

1.4. Photosynthetic Oxygen from Algae and Cyanobacteria

Oxygen supply is generally limited by metabolic processes and diffusion, which can be disturbed during injury and disease. Also, during *in vitro* experiments, oxygen supply through the blood circulation is absent and oxygen is only delivered by diffusion from the surrounding Ringer solution. This diffusion restricts neuronal activity, especially if there is a higher oxygen need due to enhanced neuronal activity. Aiming at a spatially more accurate and faster means for the modulation of the oxygen level in the brain, the natural capability of algae and cyanobacteria was exploited to produce oxygen upon illumination. Plants perform photosynthesis during light illumination, and as a by-product of their metabolic process, oxygen is produced. A recent study of algal application for local wound recovery showed the benefits of oxygen supply, as it could be delivered locally thus accelerating the healing process [47]. As some nutrients like oxygen have a small diffusion distance in the tissue of only $\sim 30\,\mu m$ - $40\,\mu m$ [25], a local supply is beneficial to guarantee fast and adequate delivery. Wound healing in human patients for instance relies on various factors, i.e. oxygen supply, immune cells, growth factors, as well as the patients own regenerative capacity [48]. However, this capacity could be reduced during aging, inadequate nutrition, and chronic diseases such as diabetes or peripheral arterial diseases [49, 50]. *In vitro* designed transplant material is used clinically, but comes along with some downsides such as chemical degradation, toxic metabolites, and a limited capacity of oxygen carriers [51]. A previously established approach showed the advantage of light activation of microalgae for oxygen production [52]. This is used in artificial tissue constructs based on fibroblasts with integrated algae, that can satisfy the metabolic needs to accelerate wound healing. These constructs are biocompatible [53], release oxygen with no capacity limitation of oxygen carriage [47], and could be removed rapidly without the necessity of surgical interventions. The ability of *Chlamydomonas reinhardtii* (*C.reinhardtii*) to produce oxygen upon light illumination was used in previous studies in symbiosis with fibroblasts [54], in zebrafish, and mice [52].

However, limitations arise if the application area is not superficial but internal, and the diffusion of metabolites from the tissue constructs cannot reach intrinsic targets. Since artificial tissue modified with algae is proven to be safe for *in vivo* approaches

and does not trigger an immune response [52], Alvarez *et al.* designed chimerical plant-vertebrate organisms (plantebrates) with injections of *C.reinhardtii* into zebrafish embryos [53]. Their hypothesis is that it might be possible to engineer a vertebrate which is potentially independent on external oxygen supply.

In this dissertation, the delivery of microorganisms *Chlamydomonas reinhardtii* and *Synechocystis* sp. through the vascular system into the brain was performed in amphibian *Xenopus laevis* larvae. The distribution through the brain vasculature enabled a fast oxygen delivery for neuronal cells, by a new approach called 'Synthetic Oxygen Supply' (SOS). This approach is an ideal model to study the sufficiency of algal-produced oxygen for maintained neuronal activity under hypoxia. *Xenopus laevis* has generally a high hypoxia tolerance, which potentially is the reason that semi-intact *in vitro* preparations can sustain the isolation for a considerable amount of time. Application of photosynthetic organisms into the vascular system and distribution throughout the body including the central nervous system could potentially further enhance the survival of such a preparation. Algae and cyanobacteria are capable of photosynthesis when exposed to light, using the photosystem I and II (phototrophic growth), and are able to maintain the activity of their ATP machinery during dark phases, using OXPHOS and glycolysis (Gly) (heterotrophic growth). This means that oxygen will be consumed by the algae or cyanobacteria in darkness. Since the total oxygen production of such microorganisms is higher than the self-consumption, the focus was on the oxygen production that is provided to the brain to cover the respective oxygen needs. For the experimental approach to test the beneficial implications of oxygen supply through photosynthetic microorganisms that are inserted into the vascular system, *in vitro* preparations obtained from *Xenopus laevis* larvae are excellently suited.

1.5. Outline

The present work is structured as follows. In Chapter 1, a general introduction to brain oxygen dependency is given and the need for this study is explained. Further, effects of hypoxia are described, and *in vivo* vs *in vitro* hypoxia studies are emphasized. The employed *Xenopus laevis* animal model system is introduced and the ability to use photosynthetic oxygen from algae or cyanobacteria for neuronal rescue under hypoxia is described.

Next, in Chapter 2 (Background) the energy metabolism in a cell is defined (Sec. 2.1). Hypoxic conditions in the animal kingdom, as well as the evolution and oxygen adaptation are discussed (Sec. 2.2) and especially oxygen robust species, such as *Xenopus laevis*, are reported (Sec. 2.3). The symbiosis with microorganisms in nature and lately for clinical use as oxygen supply are outlined (Sec. 2.4).

Chapter 3 (Experimental Methods) describes the experimental methods of the animal model *Xenopus laevis* and the semi-intact *in vitro* preparation and its benefits are explained (Sec. 3.1). The preparation of algae and cyanobacteria in culture (Sec. 3.2) and the implementation of the injection of algae or cyanobacteria into the *Xenopus laevis* larvae (Sec. 3.3) are presented, including the experimental setup, recording conditions (Sec. 3.4), and data analysis (Sec. 3.5).

Chapter 4 (Experimental Results) describes oxygen depletion around the preparation, especially in the IV$^{\text{th}}$ ventricle, where the O_2-consumption of brain tissue is recorded (Sec. 4.1). The correlation of neuronal activity to this depletion and a quantification of oxygen need during increased neuronal activity is discussed (Sec. 4.2). The visualization of algae and cyanobacteria in the brain vasculature is shown, as well as the oxygen production via photosynthesis in isolated and injected form (Sec. 4.3).

This is followed by a discussion (Ch. 5), where the results of this study were interpreted and suggestions for further studies were made (Ch. 6).

2. Background

Before the development of new techniques to facilitate oxygen delivery to injured tissue for a faster recovery, a full understanding of the pathways and circuits in the brain is crucial to identify critical events and possible intrusion points, when treatment becomes necessary. In this process, general conditions such as the optimal oxygen level, oxygen delivery, and diffusion into tissue, as well as resulting events have to be considered.

2.1. Energy Metabolism

Oxygen delivery to injured tissue is limited. For a proper healing process, however, higher oxygen levels are needed. Especially in older adults, chronic wounds (including vascular disease and diabetes) are more frequent, as compared to younger individuals [49]. Gould *et al.* investigated the fundamental questions about the effect of aging on wound healing and claim that during wound repair, energy needs are increased. They further reported mitochondria overuse, avoided by a shift from oxidative phosphorylation (OXPHOS) to glycolysis (Gly) [49], satisfying the energy needs. Since this shift is also a shift to lower oxygen dependency for adenosine triphosphate (ATP) production, wound recovery could also be impaired due to a lack of oxygen.

Energy-deriving pathways allow the cell to obtain energy during short-term shortage, to avoid long-term damage. Such pathways are conserved in all cell types, including neurons. As mitochondria play a major role in energy supply [55], mitochondrial malfunction leads to various symptoms and diseases such as hearing loss [56] or neurodegenerative disorders [2, 55]. Baloh *et al.* found an increased mitochondria population after a loss of balance and the occurrence of oscillopsia, indicating a compensatory mechanism due to mitochondria dysfunction [57]. Mitochondria and other cellular processes are dependent on oxygen availability, making oxygen a key molecule in energy supply. However, the energy cycles are also flexible, as more than one cycle contributes to ATP production. The energy-deriving cycles work continuously to produce ATP and supply the cell with energy as shown in Fig. 2.1. The cycles consist of the following steps:

- ATP derives from different metabolic cycles (the Gly, tricarboxylic acid (TCA) cycle, and OXPHOS) which are linked together, building a functional ATP production machinery.
- Gly is located in the cytoplasm, the TCA cycle and OXPHOS are both located in the mitochondria. A majority of ATP resolves from mitochondria, and further mitochondria activity is dependent on oxygen availability, making mitochondria cellular oxygen sensors.
- In mitochondria, OXPHOS oxidizes each mol of Glucose using 6 mol O_2 to produce 34 mol ATP, which is the highest contribution to ATP production. The TCA cycle and Gly contribute with only 2 ATP each.
- Key molecules, such as glucose and pyruvate, function as metabolic fuel and therefore regulate metabolic pathways.
- Other cycles interact with these main cycles and promote their functionality by providing additional energy derivatives (nicotinamide adenine dinucleotide in its oxidized: NADH; or reduced form: NAD^+, flavin adenine dinucleotide ($FADH_2$) or intermediate molecules, such as fatty acids, sugars, and amino acids. The pentose phosphate pathway (not shown here), promote Gly in producing glyceraldehyde 3-phosphate and fructose 6-phosphate, which are directly processed into Gly. Further, 2-Nicotinamide adenine dinucleotide phosphate (reduced derivative: NADPH) and $FADH_2$ production occurs in the Gly and TCA cycle, driving OXPHOS to produce ATP.

In detail, during Gly, 1 molecule glucose is transformed into 2 molecules pyruvate, producing 2 ATP and 2 NADH as energy source. During normoxia, the 2 pyruvates are transported into mitochondria and 2 Acetyl CoA are produced, as 2 NADH. Followed by the TCA cycle, where 2 Acetyl CoA break down into 4 CO_2 yields 2 CoA, 6 NADH, 2 $FADH_2$, and 2 ATP. Whereas the TCA cycle occurs in the mitochondria inner matrix, OXPHOS takes place in the intermembrane space, where the membrane is folded into so called cristae. NADH and $FADH_2$ provide hydrogen ions (H^+), which are required to start OXPHOS. Electron transport systems pump hydrogen ions (H^+) into cristae, where they become concentrated. When H^+ moves under osmotic pressure into the matrix, the ATP synthase uses this gradient to produce ATP. From the one mol glucose so far 10 NADH and 2 FADH were produced, which will be converted in OXPHOS to 34 ATP, producing in total 38 ATP from 1 mol glucose. As final action, electrons are transmitted onto O_2, O^{2-}, and H^+ to produce H_2O [58].

During hypoxia, the step where oxygen is necessary to continue with pyruvate transportation into mitochondria is prevented, thus leading to anaerobic lactate production. Therefore only the glycolysis is possible, which requires no oxygen, but 2 NAD^+ to gen-

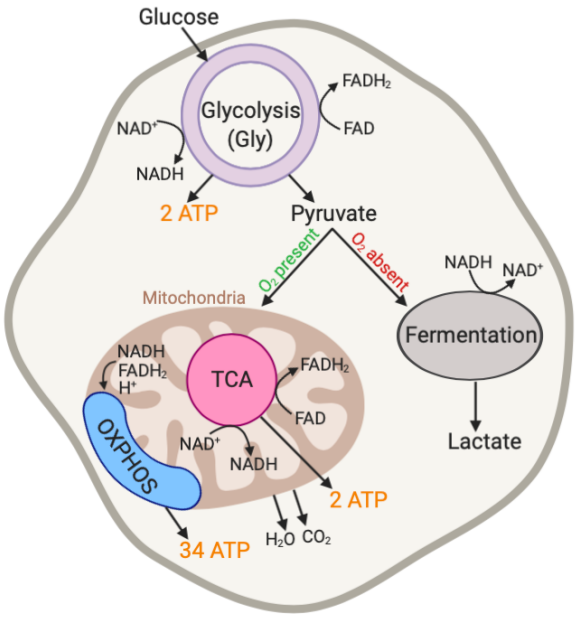

Figure 2.1.: Energy deriving pathways – Glucose conversion into pyruvate during glycolysis producing ATP, NADH, and $FADH_2$. If oxygen is present, pyruvate will be transferred into mitochondria, where ATP, NADH, and $FADH_2$ is produced by the TCA cycle and further downstream OXPHOS consumes NADH and $FADH_2$ to produce ATP. Whereas a lack of oxygen leads to a conversion of pyruvate into lactate during fermentation and NADH production, but no further ATP production occurs. Schematic created with ©BioRender - biorender.com.

erate 2 ATP. In the fermentation cycle the formation of NADH to NAD^+ requires the addition of electrons to pyruvate to produce lactate [58, 59].

Working continuously, these cycles produce ATP and store it for high energy demands during increased cell activity [60]. Oxygen, as a key molecule in the energy cycles, is important for undisturbed cell function. Therefore, on the one side, oxygen is an essential molecule, especially in terms of aerobic respiration. On the other hand, cumulative oxygen causes oxidative stress and could lead to cell death. During oxidative stress, reactive oxygen species (ROS) such as O^{2-}, H_2O_2, OH^-, and $^1O_2$ are produced. Those harmful molecules with reactive, unpaired oxygen electrons attack DNA and proteins, leading to dangerous changes and malfunction in the genome. Up to 3 % of oxygen taken up during respiration will end in ROS [61]. Cells struggle to obtain enough oxygen for generating ATP while minimizing the accumulation of oxygen that might lead to harmful cellular stress and damage. Therefore, oxygen balance is a critical and strictly controlled mechanism. The respiratory organ for this reason could be seen as 'gatekeeper', whose major function is to balance cellular oxygen delivery against oxidative damage [62].

The whole metabolic network is set up early in development and is maintained through-

out adulthood. Hence, precise tuning of the network is important for cells to outlast external changes and to guarantee energy availability for adequate cell function and survival. Different hypotheses exist on how the energy consumption in the brain is distributed. In 1981, Astrup *et al.* showed that 45 % of the energy is used for non-signaling processes [63]. Howarth *et al.* assumed that neuronal activity is expensive in ATP consumption [64], and in a recent study Zheng *et al.* stated that neuronal activity particularly relies on OXPHOS [55]. However, Sick *et al.* assumed only 50 % of energy demand is covered by OXPHOS and the other 50 % is supplied by Gly.

The link between O_2-consumption and neuronal activity was made by Hall *et al.*, when they showed that an increased ATP production via OXPHOS leads to a reduction of oxygen in rat hippocampal slices [21]. Further, measurements of NADH and FAD autofluorescence showed an 80 % reduction during inhibition of OXPHOS, demonstrating that ATP production occurs mainly by OXPHOS [22]. As neuronal activity influences the O_2-consumption in slice preparations [21], the question arises of how this dependency of neuronal activity and O_2-consumption is reflected in the intact brain. This question has been addressed in one of the studies of the present thesis, see Sec. 4.2.

2.2. Hypoxic Conditions in the Animal Kingdom

In the animal kingdom, some species are naturally accustomed to hypoxia, with some of them having even adapted to live permanently in oxygen poor environments. Under hypoxic conditions, the brain is inundated with ROS [65]. However, some species are able to suppress ROS overproduction and protect their brain from damage. The ability to tolerate hypoxia could arise from various adaptations. Examples include natural habitats in subterranean environments where oxygen is limited or fully absent (e.g. naked mole rat), the ability to perform long dives (e.g. whale, aquatic frog), or the biological need for hibernation where metabolic rates are decreased to a minimum (e.g. arctic ground squirrel) [9].

2.2.1. Evolution and Oxygen Adaptation

In order to understand the tolerance of hypoxic conditions of some species, we have to go back in time to learn how the need for oxygen evolved. The first oxygen appeared two billion years ago as a result of photosynthesis by cyanobacteria [66]. That molecular oxygen changed organisms into multicellular eukaryotic organisms over the next 700 million years, and anaerobic into aerobic eukaryotes within the next 2 billion years [67]. Oxygen as source for aerobic metabolism is 20 times more efficient with respect to en-

ergy production [68] than an anaerobic metabolism. Additionally, air breathing is much more effective than water breathing for the following reason: In water, the ventilatory rate is much slower than breathing in air. Further, the solubility rate of oxygen in air is 30 times higher than in water and the diffusion rate in air is 8×10^3 faster. When 200 g water contains 1 ml oxygen, 7 g air contains the same amount of oxygen. That makes water breathing more expensive with regard to the production of the equivalent amount of oxygen [68]. Thus, evolutionary development of lungs appeared to be a necessary step. Much earlier than expected, lung development began in water [68]. But first, blood circulation and therefore hemoglobin appeared before gills or lungs developed. 370 fish species are known as air breathers [69], and developed respiratory organs such as the suprabranchial chamber membrane or the labyrinth apparatus, a highly vascularized respiratory epithelium that allows oxygen extraction from air [70]. During fish or amphibian development, early larval stages obtain oxygen only through diffusion through the skin. At later stages external and internal convection occurs, to the point of water ventilation. Until that stage, some species, such as amphibians, are inside of eggs with limited oxygen availability. After hatching, fish development stops at that stage, but amphibians will develop further and transit from water- to air-ventilation during their last step of metamorphosis. The O_2-consumption during metamorphosis in larval anurans increases with (body mass)$^{0.83}$ [28]. Nevertheless, a huge increase in body size even after metamorphosis challenges amphibians in aerobic and anaerobic environments [28]. This is the reason why amphibians change from primary skin breathing to gill ventilation as body surface increases, in particular increasing gill surface, which results in a shorter blood-water diffusion distance [28]. How fast this transition is accomplished is seen in *Bufo americanus*. The larvae develops during metamorphosis with non-functional lungs within a few days to exclusively air-breathing juveniles [28]. The appearance of oxygen changed the development of (almost) all species on earth. Not only oxygen breathing was involved, but also the oxygen need for cell activity and later for brain functionality.

2.3. Amphibians and *Xenopus laevis*

The relevance of oxygen for neuronal processes is important to study, as fundamental mechanisms in amphibians allow to draw conclusions for human oxygen pathways. There are several animal models that can be used as a simplification of human biology. The animal model of choice for a certain study then depends on the experimental approaches. The African clawed frog (*Xenopus laevis*) has found its way into science a long time ago. Originally *Xenopus* habituated South African rivers and were first used as pregnancy test back in 1930 by Hogben, a zoologist studying hormones by injecting them into frogs [71].

Today, *Xenopus laevis* is a promising model for limb regeneration studies [72], wound healing [73], and axon regeneration studies [74]. *Xenopus* have a large brood size of about 500 - 3000 eggs, are low in housing costs, and have easily accessible embryos. The life cycle is relatively short compared to other amphibians, with 7 days to tadpole stage 48 and 12 months to an adult, fertile froglet. Further, they can live for up to 30 years in captivity. Their eggs are big (>1 mm diameter) with huge nuclei of 0.5 mm, thus allowing microsurgery and experiments on embryos. With hormone injections, *Xenopus laevis* reproduce all year (every 3 - 4 months) [75]. The staging table of *Xenopus laevis* is shown in Fig. 2.2. *Xenopus laevis* larvae are fast growing, reaching metamorphic stages (stage 52, see Fig. 2.2) only 21 days after hatching. Anesthesia for experiments can be applied easily and safe in a bath solution. The larvae are transparent, facilitating experimental access, for example to the vestibular sensory system or ocular motor nerves [29]. Further, for experiments on the labyrinthine organs the bony bulla is easy to open as it consists of cartilage.

The morphological changes during metamorphosis makes *Xenopus laevis* a highly interesting animal model for studying development and locomotor circuits during this transformation. While the young larvae have a tail-based swimming only, advanced larvae with hindlimbs start using a mixed tail- to limb-based locomotion, until the adults resorb their tail and have a limb-based locomotion only [77]. This developmental shift has also an influence on gaze stabilization during locomotion [29, 31] and is important for understanding human diseases such as vertigo and dizziness. Further, gaze-stabilization is used for studying the adaptation in intrinsic extraocular motor coupling mechanisms [29]. The first *in vitro* preparation of the frog brain was performed by Hackett [78]. This preparation has been used so far for pharmacological studies, such as by Cochran *et al.* who studied the synaptic transmission onto second-order vestibular neurons [79], or Straka *et al.* who investigated semicircular canal-specific excitation and inhibition of second-order vestibular neurons [35]. Retrograde and anterograde labeling of internuclear neurons in *in vivo* and *in vitro* experiments gave information about the location of medial and lateral rectus motoneurons [80]. Furthermore, the genome is fully known and allows proteomics studies [81]. Compared to mice (90 million years) and chicken (310 million years), *Xenopus* are more distant to humans in evolutionary aspects (360 million years), but derive from the same root of vertebrate ancestors. In comparison to mammalian neuronal circuits, *Xenopus laevis* has a far simpler assembly, however, with a homologous organization as mammalian circuits at a basic level. Therefore, some studies use *Xenopus laevis* and other frogs to evaluate principal brainstem pathways and trigger phenomena, which appear in human diseases and infections, such as chytridiomycosis [82, 83], tubercu-

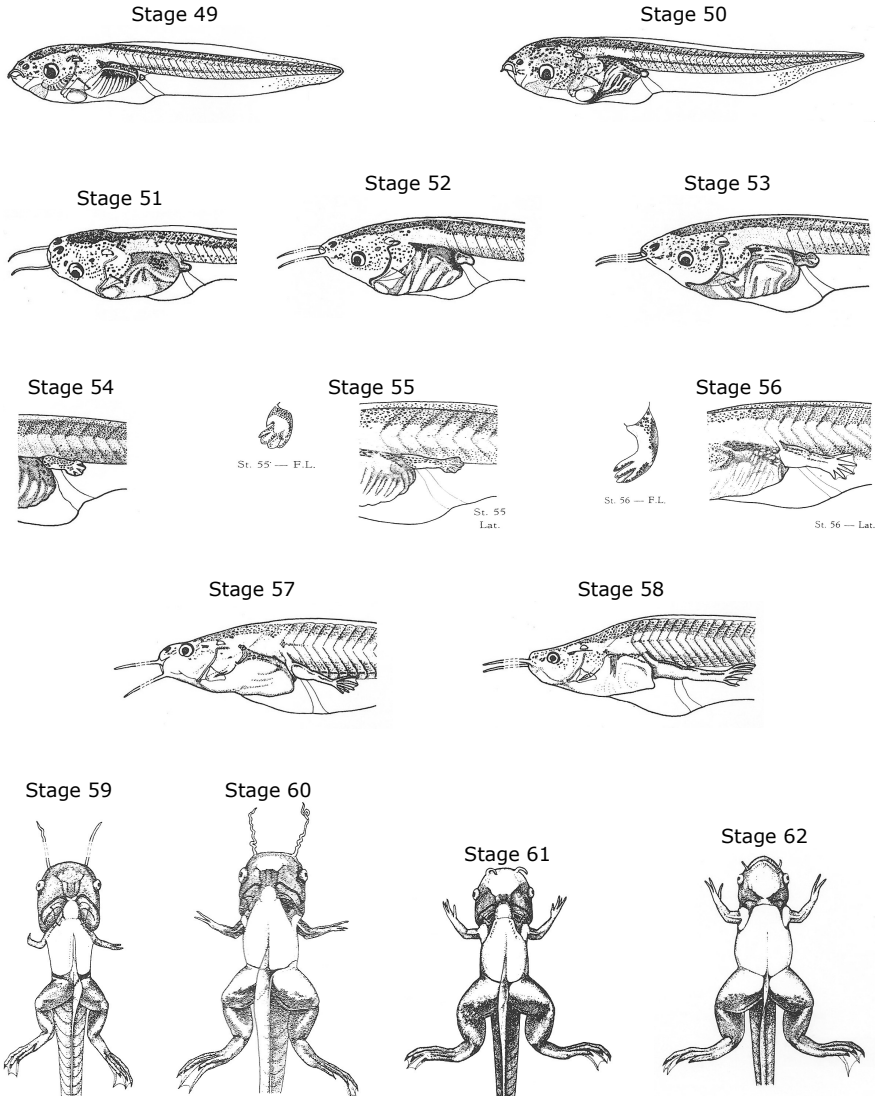

Figure 2.2.: Staging table of *Xenopus laevis* – Staging starting from larvae (stage 49) to young froglets (stage 62). Stage 0 to stage 48 is the development from a fertilized egg into a larva and stage 63 to stage 66 development to an adult frog (not shown). Each stage differs from the former stage in growing hindlimbs, forelimbs, growth and regression of the tail, and shape of head and body. With this staging table *Xenopus laevis* growth status can be clearly determined. Figure adapted from Ref. [76]. Reprinted from Normal Table of Xenopus Laevis (Daudin): A Systematical and Chronological Survey of the Development from the Fertilized Egg Till the End of Metamorphosis, Vol 2, P. D. Nieuwkoop, J. Faber, 252 pages, Copyright Garland Pub., (1994), with permission from Elsevier.

losis [84], diabetes [85], endocrine disease [86], Alzheimer's disease [87], Meniere's disease [88], or saccades [89].

Xenopus laevis tadpoles are good experimental specimen for other reasons as well. They can tolerate low oxygenated water, already at early stages. Although adult *Xenopus* have perfectly developed lungs, the larvae use gills. Consequently, during metamorphosis, the animal has to change its respiratory mechanism. Amphibians and reptiles show a discontinuous respiration pattern [90], in comparison to mammals, birds, and terrestrial vertebrates, which have a continuous pulmonary respiration. Some amphibian species have a smaller or missing left lung, or even have three lungs [91, 92]. Metabolic rates in amphibians derive from pulmonary respiration and cutaneous gas exchange, the latter being in some species the major oxygen source [93]. Cutaneous gas exchange is exclusively present in aquatic species. It is well known that amphibians have a lower metabolism [94, 95], so that passive diffusion is adequate. The diffusion capacity of oxygen though has its limits. Through tissue, an oxygen diffusion is possible up to $\sim 40\,\mu m$ [25]. While for skin diffusion, gases need to conquer 18 µm to 60 µm distances, diffusion distance via lung epithelia is 100 times smaller [96]. Further, skin breathing is an obstacle as the availability of oxygen is dependent on the water in the surrounding. That makes lung breathing more efficient than skin breathing.

The well-vascularized skin allows amphibians a passive gas diffusion via the skin, which accounts for 20 % to 85 % of their oxygen needs [62, 97, 98]. This passive diffusion via the skin enables amphibians to oxygenate their blood during diving. However, if higher metabolic rates are required, such as in bullfrogs, cutaneous gas supply is insufficient and the bulk of oxygen derives from pulmonary gas exchange [99]. In *Xenopus laevis*, the general oxygen supply is mainly covered by a huge lung oxygen reservoir, that allows long diving periods of up to 40 min without breathing for a 95 g - 153 g animal [100]. However, *Xenopus laevis* has an additional oxygen supply from blood and tissue stores [101]. While the oxygen supply through skin breathing is limited, lung oxygen uptake rises linearly when the total gas exchange increases [98]. In older stages of *Xenopus laevis* larvae, lung breathing is used to fulfill all oxygen requirements [102]. Emilio and Shelton measured the O_2-consumption of an adult *Xenopus laevis*, which is 4.2 ml/100g/h provided by the lung, and 0.6 ml/100g/h provided by the skin [103]. When *Xenopus laevis* are stressed, O_2-consumption increases to 8.6 ml/100g/h (lung), and 2.5 ml/100g/h (skin) [97]. Adult *Xenopus laevis* body weight ranges from 30 g - 86 g (males) and 93 g - 140 g (females) [104]. The blood volume makes up 13.4 % of the body weight [105], with a blood oxygen capacity of 8.5 vol% [106]. The calculation of oxygen stored in the blood amounts from 0.34 ml/h up to 1.60 ml/h. Similar values (0.9 ml) were found by Boutilier *et al.* [100]. Compared to the lung oxygen capacity, which is 8 ml [100], oxygen storage in the blood is quite

small. The O_2-concentration found in tissue storage is less than 0.1 ml oxygen [97] and comparatively small to the amount of oxygen in the blood. Therefore, the lung is the most efficient source providing oxygen. All oxygen storages will last for a maximum of 28 min for a 100 g *Xenopus* [100]. The results are consistent with Hemmingsen's equation [107], where O_2-consumption in relation to body mass is predicted via

$$V_{O_2} = 0.82 \times M^{0.75}, \tag{2.1}$$

with the O_2-consumption (V_{O_2}) in µl/h and body mass (M) in mg.

For an adult *Xenopus laevis* with a weight of 100 g, Hemmingsen's equation calculates an O_2-consumption of 4.61 ml/h, which is close to what was found by Emilio and Shelton (4.2 ml/100g), [103]. Assuming that the equation is valid also for *Xenopus laevis* larvae, a body weight of 0.3 g (stage 53, see Fig. 2.2), yields an O_2-consumption of 0.0591 ml/h.

Winwood-Smith and White measured metabolic rates with a flow-through respirometry system, where O_2 and CO_2 were monitored [108]. They showed that *Rhinella marina*, another African frog, under normal conditions (10 °C and 25 °C) require pulmonary respiration, since cutaneous oxygen uptake is not sufficient to cover cellular oxygen respiration. This was also shown by Boutilier in 1986 for *Xenopus laevis* [101]. Further, the amount of pulmonary respiration is proportional to the temperature and almost absent at low temperatures. Long periods where no oxygen uptake occurs through the lung are called apnoea and are predominantly present at lower temperatures, i.e. < 10 °C [108]. Terrestrial amphibians, such as *Rhinella marina*, use skin breathing to provide oxygen during apnoea up to 3 hours under reduced temperature conditions. However, during apnoea under normal temperature, skin gas diffusion is not sufficient to satisfy oxygen needs [108].

During critical phases, where oxygen is temporarily limited, the body's own oxygen stores are depleted, and an accumulation of lactate occurs, which is the result of an anaerobic metabolism [100]. Fig. 2.3 shows the dynamics of arterial blood values such as oxygen and lactate before, during, and after a dive. When enforcing a dive in *Xenopus laevis*, the oxygen pressure measured in the artery decreases as oxygen is consumed continuously, see Fig. 2.3 a). The haematocrit concentration is almost doubled during an enforced dive. This shows that during oxygen shortage, blood oxygen supply is increased and the metabolism switches to anaerobic conditions to provide energy from additional sources. Further, in Fig. 2.3 b) arterial blood CO_2 pressure and lactate increases during a dive. Both rises lead to a drop of pH in the plasma. Further, bicarbonate concentration in the plasma declines, indicating lactate production. These data allow insight into a general O_2-consumption of the whole animal during active or passive phases. However, how much oxygen is needed for brain activity, or in other words, how much oxygen the brain

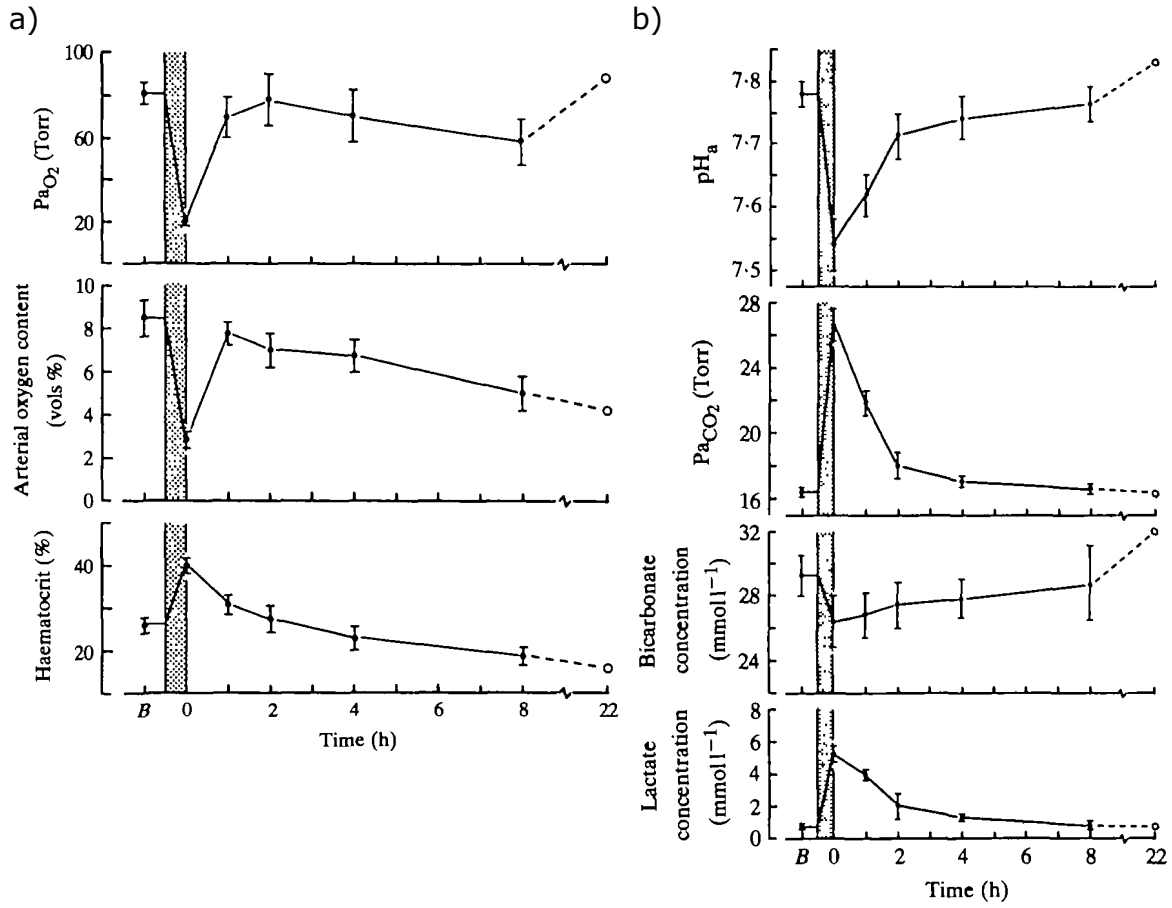

Figure 2.3.: Arterial blood values during enforced diving (30 min, shaded area) of an adult *Xenopus laevis* – a) Oxygen pressure and arterial oxygen content (vol%) decreases during the dive, while haematocitin (%) increases. The recovery phase (at 8 h) after the dive shows lower concentrations than before. b) Measurements of arterial blood values show a decreased pH during enforced diving and increased pH levels that return to normal values after the dive. CO_2-pressure during the dive increases from 16 Torr to almost 28 Torr at the end of the dive. Bicarbonate concentrations decrease slightly, whereas lactate concentrations increase during the dive. Pictures taken from Ref. [100], adapted with permission from J. Exp. Biol.

consumes at rest or activity, has not been specified so far. As shown above, amphibians have a unique oxygen supply, however, other species developed different forms to cover their oxygen needs.

2.4. Symbiosis in Nature and Clinical Approaches

Symbiosis with algae or cyanobacteria are naturally found in the animal kingdom, where the host provides habitat and shelter, and in reverse receives nutrients from the symbiont.

In terms of evolution, some species join forces to live with additional or better conditions. In addition, some animals took the step to symbiosis with photosynthetic cyanobacteria or algae. One of the factors of choice of an animal host is a good body-to-volume-ratio. Larger surfaces provide the photosynthetic symbiont with a better capture of light. The host receives photosynthetic products such as maltose, glucose, succinate, fumarate, and oxygen which are fed into its own metabolic pathways. Further, metabolic waste products from the host can be used by the photosynthetic symbiont to recycle products, which are again valuable for the host. One of the main waste products is nitrogen, and it was shown that in some symbionts nitrogen recycling occurs [109].

However, photosynthesis comes along with some downsides for the host, such as the production of reactive oxygen species, which, if high and concentrated, could destroy membranes and proteins. Further downsides are changed environmental conditions such as elevated temperature [110] or bleaching due to light illumination [111]. Those negative effects can lead to a breakdown of the bond between host and symbiont, ultimately leading to the death of the host [111]. Most animals performing a symbiosis in nature are from one of two families: Porifera (sponges) and Cnidaria (hydroids, corals, sea anemones, and jellyfishes). The dominant algae symbionts in these hosts are freshwater chlorophytes (genus Chlorella). An example for a bilateral symbiosis is the sea slug, as shown in Fig. 2.4 b). Its large surface makes it an excellent host, and its lack of a circulatory system makes the algae a good symbiont. Morphologically complex animals also form symbiosis, e.g. molluscs such as tridacna gigas, see Fig. 2.4 a), which hosts photosynthetic algae of the genus Symbiodinium. Some hosts have even morphological conflicts when going into symbiosis and need to re-organize their shape or body plan. Most Cnidaria have to compromise in relation to their tentacles, for the sake of nutrition they need both photosynthesis and feeding. For example, Bunodeopsis antilliensis, shown in Fig. 2.4 c), have a few long and mobile tentacles to catch food, and many short tentacles where symbiotic algae reside. These morphological adaptations indicate an advantage for the host going into symbiosis with photosynthetic algae or cyanobacteria. Besides morphological changes, also biochemical changes are necessary for a successful symbiosis. Apart from a few exceptions, algae in symbiosis are located intracellularly at the membrane of the host. Delivering substrates to the specific location where the algae are located require changes such as new transporters or higher enzyme activity [112].

The supply of oxygen by the symbiont is often only a byproduct of their own metabolic pathway. Algae and cyanobacteria use photosynthesis to trigger water photolysis for the production of oxygen by using the energy of light, as illustrated in Fig. 2.5. To start photosynthesis, energy is needed. This required energy is delivered by four light quanta, activating both photosystem I (PS I) and photosystem II (PS II) in parallel, triggering the

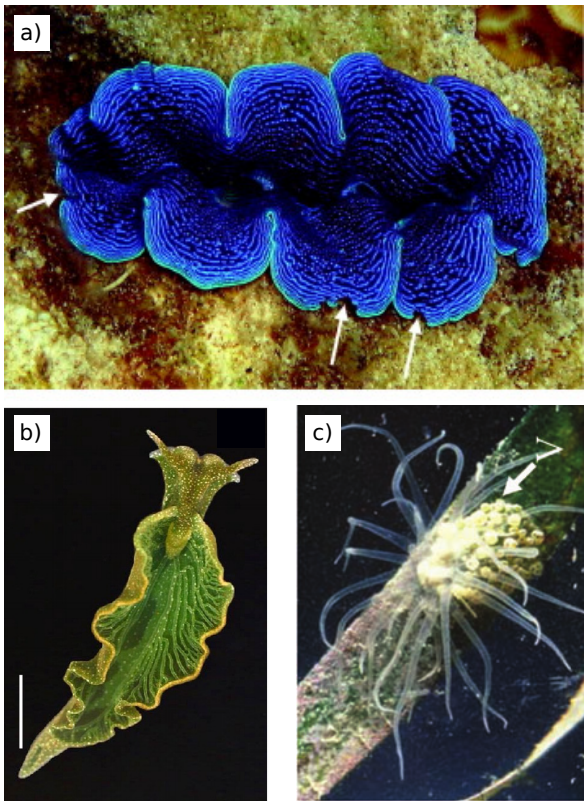

Figure 2.4.: Examples of symbiosis in nature – a) Giant clam, b) sea slug, c) and sea anemone are representative hosts for algae. White arrows in a) mark fish bites on the mantle edge, in c) vesicles bearing symbiotic algal cells. Calibration bar in b) represents $500\,\mu\mathrm{m}$. Pictures taken from a) Ref. [113], reprinted from Biological Conservation, Volume 181, Neo, M. L., Eckman, W., Vicentuan, K. Teo, S. L.-M., Todd, P. A., The ecological significance of giant clams in coral reef ecosystems, Pages 111-123, Copyright (2015), with permission from Elsevier. b) Ref. [114]; ©2008 National Academy of Sciences, c) Ref. [115], by permission of Oxford University Press.

transport of electrons and the production of ATP. The so-called photolysis happens when light excites chlorophyll molecules in the PS II pathway. The deprived electrons from the surrounding water oxidize H_2O to O_2, releasing H^+ and electrons. The electrons will be further transported via a chain reaction in an exergonic pathway by an electron transport chain to the PS I system, to return to a non-excited state. The electron transport is coupled to an H^+ transport into the thylakoid space. The rest of the energy from the exergonic path is used to produce ATP. Via further light exposure of PS I, electrons will be transported to $NADP^+$ reductase, to produce NADPH. The accumulation of H^+ in the thylakoid space activates ATP synthase, which will produce ATP by transporting H^+ into the stroma.

In the present study, two different microorganism strains were used: *Chlamydomonas reinhardtii* (*C.reinhardtii*) and *Synechocystis* sp. (*Synechocystis*). *C.reinhardtii*, see

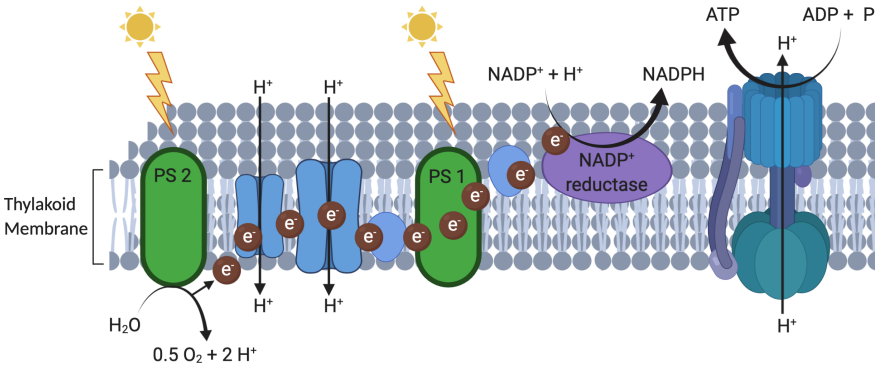

Figure 2.5.: Illustration of photosynthesis – Light with a wavelength of 680 nm hits chlorophyll, and activates the photosystem II (PS II), hydrolyzing water into oxygen and hydrogen, thereby releasing two protons and two electrons. These electrons will be transported by the electron transport chain, which is coupled to proton channels, releasing more protons into the cell. The end of the electron transport chain is the photosystem I (PS I), which is activated by light with a wavelength of 700 nm, guiding the electron to the $NADP^+$ reductase, which produces NADPH. The result of the enriched proton concentration in the cell leads to the activation of the ATP synthase, which pumps protons out of the cell and produces ATP. Picture adapted from Ref. [116]; Concepts of Biology: 1st Canadian Edition by Charles Molnar and Jane Gair is used under a CC BY 4.0 Licence and created with ©BioRender - biorender.com.

Fig. 2.6 a), is a unicellular green alga (eukaryote), up to 10 µm in size, and predominantly used for genetic studies, as its genome is fully sequenced [47, 117]. *C.reinhardtii* is found in fresh water all around the world, especially when the water is nutritious. It grows rapidly (vegetative and sexual reproduction) [118] and uses two cilia for locomotion and light detection. Rhodopsin-like photoreceptors, located on the cilia, allow the algae to control locomotion towards modest light or away from high light intensities, optimizing photosynthesis and cell nutrition [119]. Chemotaxis towards ammonium (during night) and phototaxis towards light (during day) are regulated by a circadian clock [120]. *C.reinhardtii* can grow under normoxia, as well as under anoxic conditions [121]. Algae derive their energy under normoxia from the TCA cycle and OXPHOS [122] and from glycolysis under anoxic conditions [121]. In nature, *C.reinhardtii* is continuously in contact with other organisms, where chemical signaling and nutrient exchange occurs [121].

Synechocystis, see Fig. 2.6 b), is a cyanobacteria (prokaryote), also called blue-green algae and 2 µm in size. Before oxygen was present on earth, a progenitor of cyanobacteria was already resident [123]. Photosynthesis led to oxygen release and accumulation until a change in atmosphere occurred, boosting evolution. Since bacteria lack typical membranes, the metabolic cycles, which produces ATP and oxygen, are different from those

of plants and other eukaryotic cells. It is assumed that cyanobacteria are the progenitors of chloroplasts that are present in algae [124].

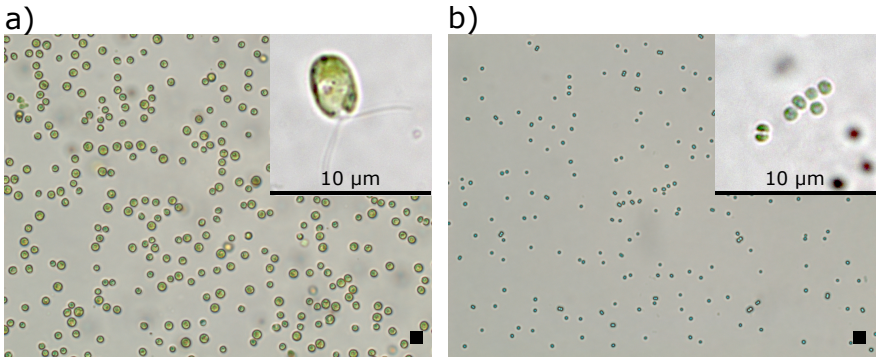

Figure 2.6.: Bright field image of isolated algae and cyanobacteria – a) *C.reinhardtii* and b) *Synechocystis*. AxioObserver 7, Zeiss, zoom 40x. Scale square represents 10 µm. Image courtesy of Myra Chávez. Zoom in the upper right corner show a higher magnification of *C.reinhardtii* in a) and *Synechocystis* in b). Taken with Nikon Eclipse 80i, zoom 60x.

C.reinhardtii and *Synechocystis* are easy to handle, cheap, fast growing, and declared as safe by the US Food and Drug Administration (FDA) [117]. Further, *C.reinhardtii* can be co-cultured with nearly any kind of cell in 2D and 3D tissues, even with those of mammalian species [52]. It was shown that the algae do not activate the immune response of the host. Oxygen could be released via light activation, and for skin defects an algae-collagen-transplant remained functional for 5 days [52]. During the wound healing processes, oxygen supply is necessary not only for ATP production in cells, but also for oxygen dependent enzymes such as NADPH-linked oxygenase [125]. Genetically modified microalgae were used to deliver not only oxygen but also pro-regenerative molecules that are beneficial for wound healing [125]. The implantation of fibroblasts with mutant *C.reinhardtii* was successfully tested in *in vitro* models and in immunocompetent mice [126].

It has been shown that the symbiotic oxygen is beneficial in nature and has a great potential for clinical approaches. In the current study the application of algae and cyanobacteria in the brain vasculature of *Xenopus laevis* larvae were studied to determine the impact of photosynthetically produced oxygen during hypoxia.

3. Experimental Methods

This chapter presents the experimental procedures used during the present work. Sec. 3.1 describes the semi-intact *in vitro* preparation of *Xenopus laevis* tadpoles. The preparation of the microorganisms is shown in Sec. 3.2, discussing the cultivation of *C.reinhardtii* and *Synechocystis*. Further, the concentration calculations for isolated and injected microorganisms, and the monitoring of the oxygen production of isolated algae and cyanobacteria is described. The experimental setup and measurement electrodes are shown in Sec. 3.4, and Sec. 3.5 finally discusses the data analysis.

3.1. *Xenopus laevis*

Amphibian *in vitro* preparations offer a more robust and less hypoxic alternative to hypothermic mammalian preparations since they have a lower rate of O_2-consumption at the same temperature [127]. The exceptional tolerance to anoxia has drawn increasing attention from a physiological and biomedical viewpoints because of the possibility to define compensatory mechanisms that may be applicable also to mammals.

In the present study, the previously established semi-intact *in vitro* preparation of *Xenopus laevis* larvae [29] were used. This preparation preserves all sensory organs, motor effectors, as well as the central nervous system [29]. However, this model lacks blood perfusion, and respiratory gases are exchanged exclusively by diffusion at the surface. For fundamental questions where an intact blood circulatory system is not of importance, such as sensory influences, signal processing, or motor output, the preparation has all necessary properties. Therefore, the semi-intact *in vitro* preparation of *Xenopus laevis* larvae is an excellent model for studying the relationship between neuronal metabolism and how it is coupled to different physiological and pathological conditions.

3.1.1. Semi-Intact *In Vitro* Preparation

Experiments were performed on *Xenopus laevis* larvae between stage 51 to 54 [76], see Fig. 2.2, of either sex. The larvae were bred in house (Biocenter, Department Biology II, Ludwig-Maximilians-University Munich, 82152 Martinsried). Larvae were maintained at

12/12 h light/dark cycles in tanks with non-chlorinated water at 17 °C and fed daily with Spirulina bacteria. Preparations and experiments were performed with consideration of the 'principles of animal care', publication No. 86-23, revised 1985 of National Institute of Health. Permission for the experiments was granted by the Regierung von Oberbayern (ROB-55.2.2532.Vet 03-17-24 and ROB-55.2-2532.Vet 02-19-128). Prior to surgery, larvae were anaesthetized in 0.05 % 3-aminobenzoic acid ethyl ester methanesulfonate (MS-222; Pharmaq Ltd. UK), perfused with a cold (18 °C) mock Cerebral Spinal Fluid (CSF), so called Ringer solution (75 mmol/l NaCl, 25 mmol/l $NaHCO_3$, 2 mmol/l $CaCl_2$, 2 mmol/l KCl, 0.5 mmol/l $MgCl_2$, 11 mmol/l glucose, and 10 mmol/l HEPES buffer, pH 7.4), and subsequently decapitated at the level of the upper spinal cord. Further, the brain was exposed, and the forebrain removed. The preparation of *Xenopus laevis* larvae is shown in Fig. 3.1 a). To ensure full recovery from anesthetics after preparation, the larvae were kept in Ringer (16 °C) for at least two hours before the experiment. For measuring discharge rates (multi-unit), the trochlear extraocular motor nerve innervating the superior oblique (SO) muscle was disconnected from the target muscle at the innervation site, see Fig. 3.1 b). This allows to record action potentials from this nerve via nerve suction into a thin glass capillary. The electrodes were pulled on a P-87 Brown/Flaming electrode puller from borosilicate glass (Science Products, Hofheim, Germany), and individually broken to fit the diameter of the SO nerve. This recording was used as proxy for central nervous activity. The region of interest for the oxygen measurements was the IV^{th} ventricle, between the caudal end of the cerebellum and the rostral end of the choroid plexus. The IV^{th} ventricle is easy to access for measurements without disrupting brain tissue and without interfering with normal circuit function, see Fig. 3.1 c). Further, the recording of extraocular motoneurons, with nuclei and most presynaptic origins located in the tissue around the IV^{th} ventricle, allowed studying the correlation between neuronal activity and O_2-consumption to a very close approximation. The bottom of the IV^{th} ventricle and the position of the electrodes were determined visually using a Zeiss Luminar microscope with 0.8 magnification. Spontaneous nerve activity (discharge rates measured as spikes/s) determined by electrophysiological recordings of extraocular motoneurons, was analyzed during different conditions such as variation of oxygen levels in the Ringer solution and drug administration. The consumption of oxygen in the IV^{th} ventricle and adjacent tissue was used as proxy for energy expenditure and recorded with an oxygen microelectrode, OX-10 [128]. O_2-concentrations and concurrent extracellular spike activity were digitized at 120 Hz and 20 KHz, respectively (CED 1401, Cambridge Electronic Design, UK) and stored on a computer for offline analysis.

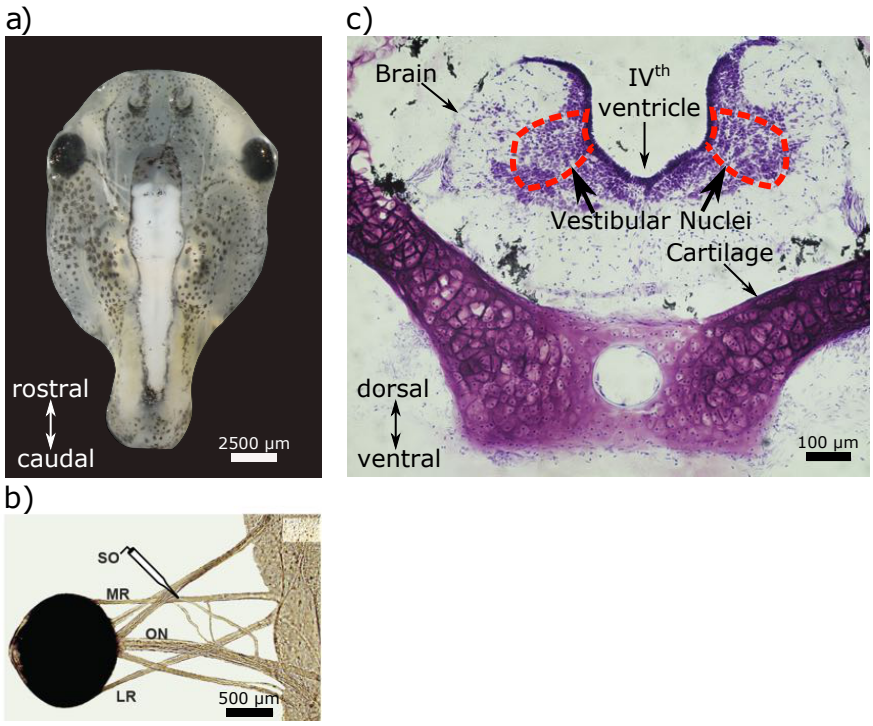

Figure 3.1.: Semi-intact *in vitro* preparation of *Xenopus laevis* larvae – a) Larval preparation, b) accessible SO nerve from the left eye, and c) coronal section through the hindbrain, Nissl staining. Figure b) taken from Ref. [45]; ©2014 Wiley Periodicals, Inc. Develop Neurobiol 75: 1051–1067, 2015. Permission granted by Wiley Periodicals, Inc.

3.1.2. Developmental Staging

When working with *Xenopus laevis* larvae, it has to be considered that each animal is an individual and develops with a different time frame. It is thus necessary to determine body size, weight, and its dependence on development. Developmental stages were determined according to the staging table provided by Nieuwkoop and Faber [76]. Therefore, each larva was weighed and measured prior to the experiment. Fig. 3.2 summarizes size and weight of *Xenopus laevis* larvae at different stages of development. To better understand the broad variability of larval development, data from studies using animals at different stages were also included in Fig. 3.2. Since Emilio and Shelton determined a total blood volume in *Xenopus laevis* as 13.4 ml/100g [97], the calculated blood volume of the larvae ranges from 26.8 µl (stage 51) to 67 µl (stage 54), assuming the calculation from Emilio and Shelton is valid for larvae as well.

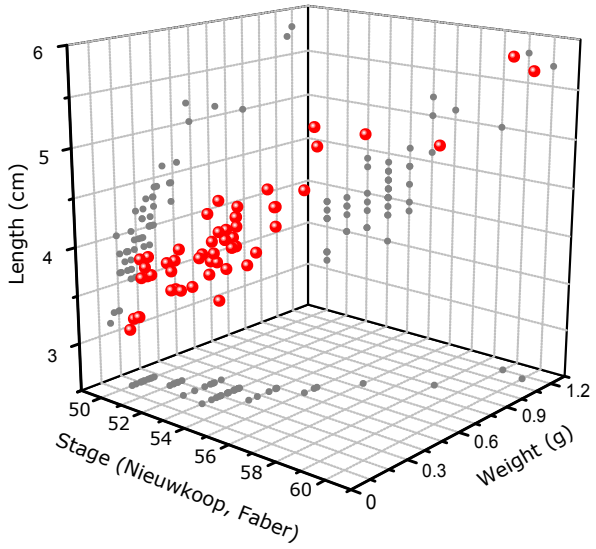

Figure 3.2.: Developmental stages of *Xenopus laevis* larvae – Three dimensional plot of larval stage (Nieuwkoop and Faber [76]), length (cm), and weight (g), to demonstrate the correlation between these parameters during larval development.

3.2. Algae and Cyanobacteria Preparation

Algae and cyanobacteria were grown in collaboration with the Nickelsen lab by Dr. M. Chávez and Prof. Dr. J. Nickelsen, Biocenter - Department Biology I, Ludwig-Maximilians-University Munich, 82152 Martinsried.

3.2.1. Cultivation of *Chlamydomonas reinhardtii*

The cell-wall deficient, arginine phototropic, cw15-30-derived UVM11 *C.reinhardtii* strain [129] was routinely grown photomixotrophically at room temperature (RT) on tris-acetate-phosphate (TAP)-agar plates under continuous light stimulation (30 µE/m/s). Before each experiment, a preculture was started by inoculating a 100 ml TAPS (TAP-medium supplemented with 1 % (w/v) sorbitol) liquid culture with plate-growing algae and allowed to grow to the middle log-phase at standard culture conditions RT, 150 rpm, (30 µE/m/s). Then, the algae-suspension was transferred into 1 L shake flasks and incubated for 4-5 days to reach a cell-concentration of 10×10^7 cells/ml. To prepare the working cell-suspensions, cell-number was first determined under the microscope using a Neubauer-chamber, then the required culture-volume was centrifuged (5 min, 1200 rpm, RT), and cells were resuspended in Ringer solution at the required concentration. As control, nac2-26 *C.reinhardtii* mutant strain was used and treated in the same way. The mutant lacked the nuclear Nac2 gene, which is required for the stable accumulation of the psbD mRNA,

which encodes the D2 reaction center polypeptide of the photosystem II. Thus the mutant was not able to complete photosynthesis.

3.2.2. Cultivation of *Synechocystis* sp. PCC 6803

The wild type *Synechocystis* strain was kept on BG11-medium agar-plates, at 30 µE/m/s to 50 µE/m/s and 25 °C to 30 °C. Plates were refreshed every 3 weeks. A liquid preculture was started, prior to each experiment, by inoculating agar-growing cyanobacteria in 50 ml BG11-medium and incubating it for 3 days at standard culture conditions (30 °C, 150 rpm, 30 µE/m/s to 50 µE/m/s). Then, cell density was determined by OD_{750} to calculate the volume necessary to start an expanded 0.75 L culture at $OD_{750} = 0.01$ ($\sim 2 \times 10^5$ cells/ml). Culture vessels were kept in a bioreactor with constant aeration (30 °C, 30 µE/m/s to 50 µE/m/s) for 3 days to 4 days or until they reached an $OD_{750} \geq 2$. Cyanobacteria were brought to the required cell-densities by centrifugation (5 min, 3000 g, RT), and were subsequently resuspended in Ringer solution. As control, the *Synechocystis* DeltaD1-TD41 mutant strain was used and treated like the wild type *Synechocystis* strain. The *Synechocystis* 6803 DeltaD1-TD41 mutant lacks the three copies of the psbA gene encoding the photosystem II subunit D1. These organisms were thus also incapable of conducting photosynthesis.

3.2.3. Calculation of Algae and Cyanobacteria Concentrations

In the following, the concentrations for isolated and injected algae and cyanobacteria are calculated.

Concentration and total cell number in 5 ml solution for isolated algae and cyanobacteria:

$$\begin{aligned} \text{Exp. 1:} \quad & 0.5 \times 10^9 \,\text{cells/ml} \cdot 5\,\text{ml} = 2.5 \times 10^9 \,\text{cells} \\ \text{Exp. 2:} \quad & 0.1 \times 10^9 \,\text{cells/ml} \cdot 5\,\text{ml} = 0.5 \times 10^9 \,\text{cells} \end{aligned}$$

Concentration of the injections to achieve the same amount of cells as in the isolated solution:

$$\begin{aligned} \text{Exp. 1:} \quad & 2.5 \times 10^9 \,\text{cells} : \quad 10\,\mu\text{l} = 0.25 \times 10^9 \,\text{cells/µl} \quad = 250 \times 10^9 \,\text{cells/ml} \\ \text{Exp. 2:} \quad & 0.5 \times 10^9 \,\text{cells} : \quad 10\,\mu\text{l} = 0.05 \times 10^9 \,\text{cells/µl} \quad = 50 \times 10^9 \,\text{cells/ml} \end{aligned}$$

To compare the injections to the isolated microorganisms, at least 50×10^9 cells/ml would be required. However, trying to augment the microorganisms in this high concentration was not possible, at least for *C.reinhardtii*. The highest concentration of *C.reinhardtii* was 10×10^9 cells/ml. Therefore, to work with the same concentration for *C.reinhardtii* and *Synechocystis*, 10×10^9 cells/ml for the injections for both microorganisms were used. The injected total volume was 10 µl, corresponding to 0.1×10^9 cells in total for both, the *C.reinhardtii* and *Synechocystis*. Because of the variance of larval blood volumes (cf. 3.1.2) due to increasing body length of older animals, in the measurements with injected microorganisms, similar larval stages were used (stage 51 and 52).

3.2.4. Oxygen Monitoring Setup of Isolated Algae and Cyanobacteria

To activate the photosystem of the algae or cyanobacteria, the light source was placed at a distance of 5 cm from the sample. Light illumination was set to 5400 lux, approximately the optimum luminance for photosynthesis [130]. Data were collected as shown in Fig. 3.3. In order to determine the intensity of the light source and the amount of light reaching the sample, a spectrometer SpectraScan® Spectroradiometer PR-655 from PhotoResearch was used. The light source was a Zeiss CL 6000 LED, with >150 W, 600 lm, and two flexible fiber optics. The spectrometer was fixed on a tripod and different distances and intensities were measured. Absorption spectra of chlorophyll and the emission spectra of the light source are described in App. A.4.

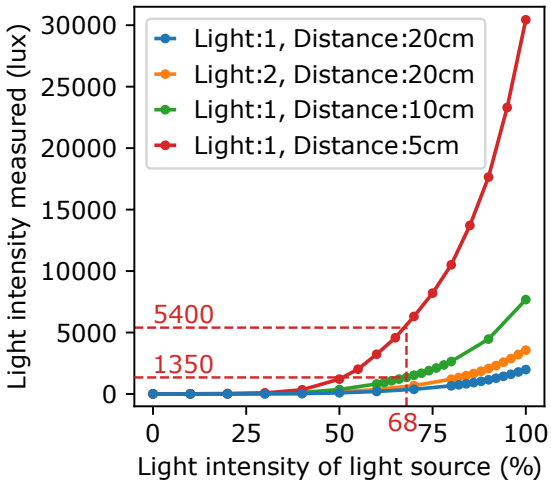

Figure 3.3.: Light Intensities – Measurement of light intensity of the light source with different luminance. Luminance was monitored at 20 cm distance, for one light source (blue), and two light sources (orange), as well as for one light source at 10 cm distance (green). The curve was calculated for the 5 cm distance (red) (for details see main text).

The desired light intensity is calculated as following:

$$\begin{aligned}
\textbf{Intended light intensity:}\quad & I = 100\,\mu\text{E} \\
& 1\,\text{E} = 1\,\text{mol photons} = 6.022 \times 10^3 \\
\text{Photosynthetically Active Photon Flux Density:}\quad & \text{PPFD} = (\mu\text{mol})/(\text{m}^2 \times \text{s}) \\
\text{Photosynthetically active radiation:}\quad & \text{PAR} = (\mu\text{E})/(\text{m}^2 \times \text{s}) \\
\text{Lux conversion factor (sun light):}\quad & C_{\text{lux}} = 54 \\
& I = \text{PPFD} \times C_{\text{lux}} \\
\Rightarrow\quad & I = 100\,\mu\text{mol} \times 54 = 5400\,\text{lux}
\end{aligned}$$

The relation between distance and luminance is given by

$$I_1 \times D_1^2 = I_2 \times D_2^2, \tag{3.1}$$

with I_i and D_i being the intensities and distances, respectively. With distances $D_1 = 5\,\text{cm}$ and $D_2 = 10\,\text{cm}$, and intensity $I_1 = 5400\,\text{lux}$, it thus follows

$$\begin{aligned}
5400\,\text{lux} \times 5^2\,\text{cm}^2 &= I_2 \times 10^2\,\text{cm}^2 \\
\Rightarrow \quad I_2 &= 1350\,\text{lux}.
\end{aligned}$$

The intensity of the light source needs to be set to a luminance of 1350 lux at a distance of 10 cm to obtain an equivalent of 5400 lux at a distance of 5 cm. Again from curve Light: 1, Distance: 10 cm (green dots in Fig. 3.3) it follows that

$$1350\,\text{lux} \mathrel{\widehat{=}} 68\,\%.$$

For obtaining the intended light intensity of 100 µE at a distance of 5 cm, the intensity of the light source was set to 68 %. The maximum that could be reached with one light source at 5 cm distance was 30 500 lux and was also used in the experiments.

Moreover, to keep the temperature constant during these measurements, the sample was placed in a Styrofoam box filled with ice water, heated to 17 °C. Details of the experimental setup are shown in Fig. 3.4. To evaluate the oxygen production capacity of isolated *C.reinhardtii* and *Synechocystis*, respectively, 0.5×10^9 cells/ml and 0.1×10^9 cells/ml were suspended in Ringer and the O_2-concentration was measured with micro-electrodes.

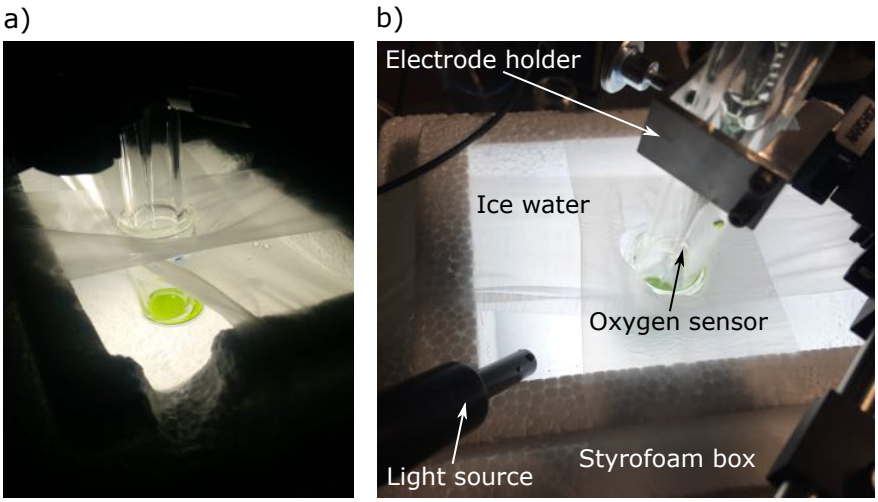

Figure 3.4.: Isolated algae and cyanobacteria – a) and b) show measurement of oxygen production in isolated algae or cyanobacteria with different light intensities.

3.3. Injection of Algae or Cyanobacteria into *Xenopus laevis* Larvae

Animals were anesthetized [0.05 % 3-aminobenzoic acid ethyl ester methanesulfonate (MS-222; Pharmaq Ltd. UK)] and mechanically secured ventral side up with u-shaped pins in a Sylgard-lined dish of 5 cm diameter and maintained in chilled MS-222 Ringer solution throughout the injection procedure. Prior to the cardial injections, the skin above the heart was gently removed. Glass capillaries (Science Products, $(0.86 \times 1.5 \times 80)$ mm with filament) for the cardial injection of the algae or cyanobacteria suspension were pulled on an electrode puller (Shutter Instrument, P-97) and cut under the microscope to adjust the tip size to a very thin needle with a tip diameter of 20 µm - 30 µm and a tip angle of 30°. A volume of 10×10^9 cells/ml algae or cyanobacteria, see Sec. 3.2.3, were filled into the glass capillary, inserted into a holder with a pressure application connector and mounted onto a 3-axes micromanipulator (Bachofer, Reutlingen, Germany). The capillary filled with *C.reinhardtii*, *Synechocystis*, or the respective photomutants was placed above the heart of the *Xenopus* tadpole and its position was adjusted with the micromanipulator to insert the tip into the ventricular chamber of the heart. The algae or cyanobacteria suspension was pressure-injected (npi Electronic Instruments for the Life Sciences PDES-02T) by single pulses of 0.2 s, produced by a pulse master Multi-Channel Stimulator (World Precision Instruments, SYS-A300). A modest pressure of 1 bar was used for all experiments. The pulses were given manually, adjusted to the animals' heartbeat, over a time range of 30 min to allow the microorganisms to spread homogeneously throughout the entire vascular system of the anesthetized larvae. This can be seen as green staining of blood

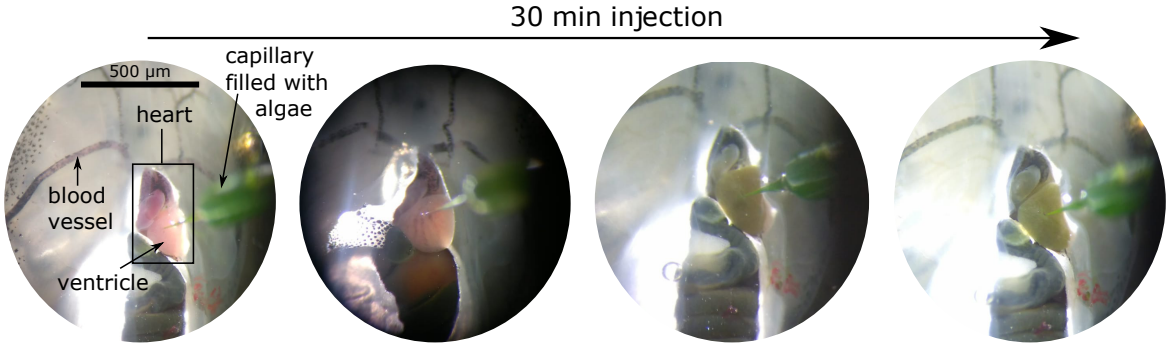

Figure 3.5.: Algae or cyanobacteria injection (the picture shows the injection of *C.reinhardtii*) – Ventral view of the heart of an anesthetized larva. The thin glass capillary filled with algae or cyanobacteria is inserted into the heart. Injection over 30 min with a total volume of 10 µl (10×10^9 cells/ml) with *Synechocystis* or *C.reinhardtii*, respectively.

vessels in Fig. 3.5. After slowly retracting the injection electrode, the deeply anesthetized tadpoles remained at 16 °C in the Sylgard-lined chamber for 30 min and were prepared for the subsequent isolation procedure. This time allowed the microorganisms to spread through the vascular system. Fig. 3.6 shows the distribution of the algae or cyanobacteria in the entire blood circulatory system of *Xenopus laevis* larvae. Thereafter, the semi-intact *in vitro* preparation was prepared, as described in Sec. 3.1.1. The blood vessels in the isolated brains were visualized using Isolectin, which stains the vascular system through a binding to the oligosaccharide component of the endothelial wall, coupled to a green fluorescence tag A488. Additionally, prior to injection, a 2 µl solution of Isolectin GS-IB4 from *Griffonia simplicifolia* Alexa Fluor™ 488 Conjugate was mixed with 8 µl algae or cyanobacteria. A total amount of 10 µl algae or cyanobacteria-Isolectin-mix was injected into the vascular system of the larvae. Following immediate decapitation after the injection, the tissue was fixed in 4 % paraformaldehyde for 8 hours. Thereafter, the tissue was cleared in glycerin for 8 hours and prepared for confocal microscopy. Whole brains were imaged on a Zeiss LSM 900-Airyscan-2 microscope by using the software ZEN (blue edition) 3.0 in sequences (z-stack) of 445 optical sections with a thickness of 1.33 µm that were reconstructed [as will be discussed in detail in Ch. 4.3 Fig. 4.25 a)]. The reconstruction to calculate the blood and microorganism volume was performed with the software Vision 4D, Arivis, see App. A.5. Images of blood vessels filled with algae or cyanobacteria were taken with a Zeiss LSM 900-Airyscan-2 microscope with 71.76 µm optical thickness, and 0.39 µm imaged sample thickness, see Ch. 4.3, Fig. 4.26 a) and with a RS-G4 Mavig Vivascope, 60x zoom-1.35 [Fig. 4.26 b)]. Detailed images of single blood vessels, filled with algae or cyanobacteria, were imaged on a Zeiss LSM 900-Airyscan-2 microscope with 58.8 µm optical thickness, and 0.21 µm imaged sample thickness [Ch. 4.3 Fig. 4.27 a) - c)] and a Mavig VivaScope RS-G4, 60X Olympus (UPLSAPO60XO, NA 1.3)

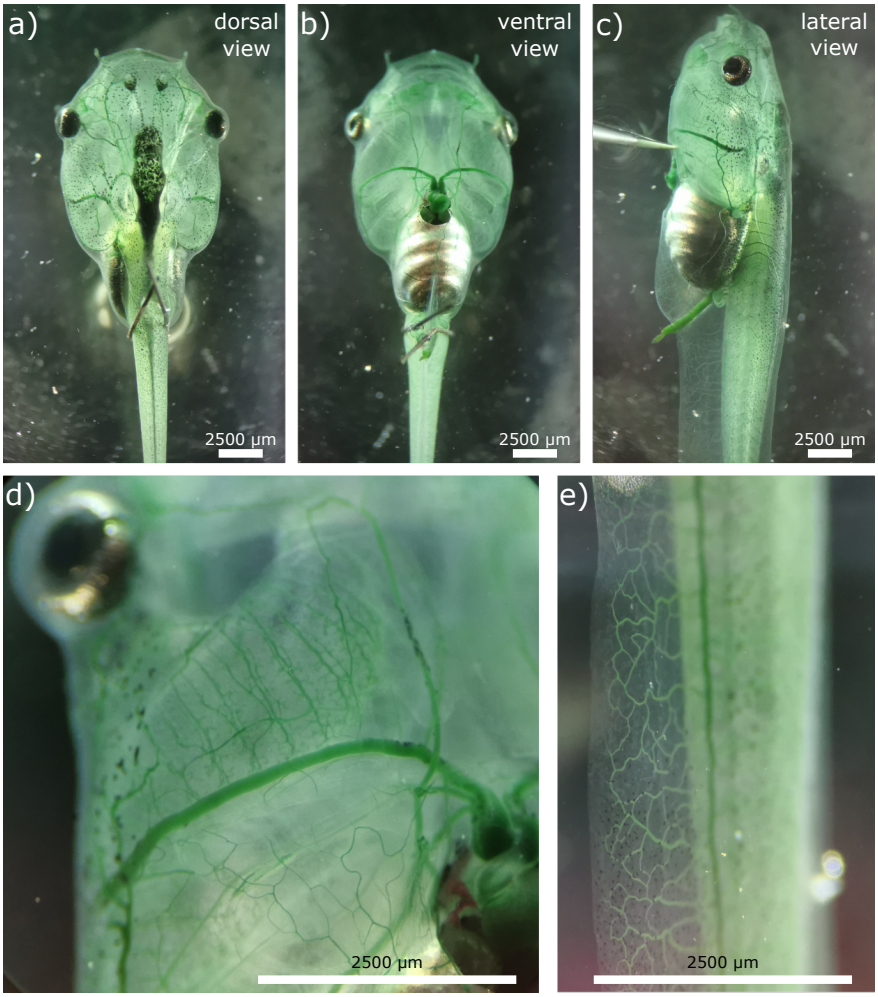

Figure 3.6.: Larva after algae or cyanobacteria injections (the picture shows injected *Synechocystis*) – Images were taken 30 min after injection of the microorganisms into the heart of the anesthetized larva. Images show a) dorsal, b) ventral, and c) lateral views. The cyanobacteria are fully distributed within the vascular system, reaching the smallest blood vessels in d) the body and e) the tail.

oil objective, with 1.5 µm optical thickness, and 95 µm imaged sample thickness [Ch. 4.3 Fig. 4.27 d) - f)]. For the blood vessels, the light absorption of Isolectin is 488 mm and emission is ∼ 500 nm. The algae and cyanobacteria with autofluorescence of the chlorophyll absorb at 430 nm and 440 nm (chlorophyll a and b), and emit at 660 nm and 640 nm (chlorophyll a and b), respectively, see App. A.4. The excitation wavelength for imaging with Zeiss LSM 900-Airyscan-2 was for chlorophyll 655 nm and for Isolectin 493 nm. For imaging with the Mavig Vivascope, the excitation wavelength was set to 640 nm for chlorophyll and to 488 nm for Isolectin.

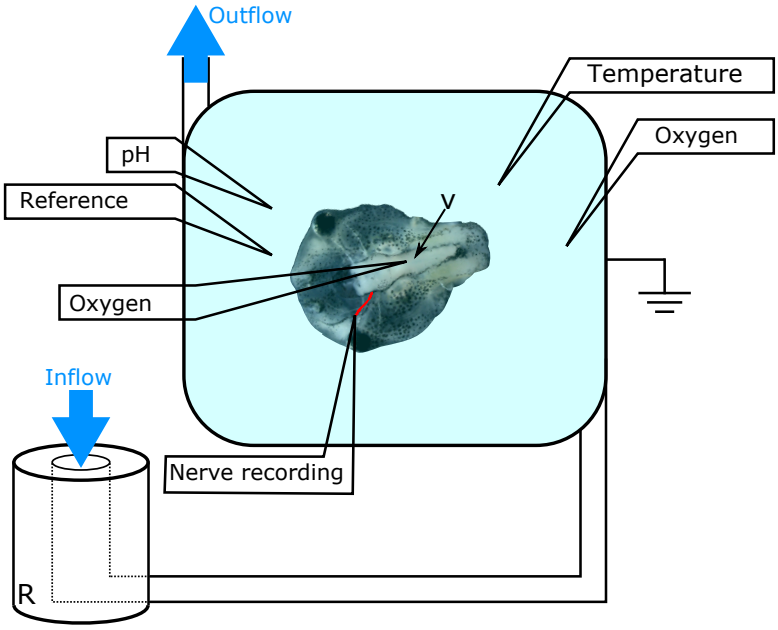

Figure 3.7.: Schematic of the experimental setup to measure the O_2-concentration in the preparation – Measurement chamber with a reservoir (R), positions of the electrodes for monitoring temperature, pH, and O_2-concentration in the Ringer and in the IVth ventricle (marked with v) of the larval preparation. Nerve recordings were obtained from the trochlear nerve (red).

3.4. Experimental Setup

Completely submerged amphibian preparations were mechanically secured to the Sylgard floor of a central chamber with a total volume of 2 ml. A schematic of the setup is shown in Fig. 3.7. The O_2-concentration could be fast and reversibly changed by alternating the Ringer solution through bubbling with carbogen (5 vol% CO_2, 95 vol% O_2) or nitrogen (100 vol% N_2) in a small reservoir, marked with R, immediately upstream of the recording chamber. The inflow rate of the Ringer solution was 3.5 ml/min and was set constant with a pump (ISMATEC, REGLO Analog MS-4/12), causing the Ringer to flow through an ice box to keep the temperature in the recording chamber constant. In all experiments the conditions were kept constant, i.e. temperature 17.5 °C ± 0.5 °C, 7.4 pH, and 3.5 ml/min pump flow. The Ringer solution was monitored with three microelectrodes, i.e. for oxygen, pH, and temperature [128]. The oxygen value inside the IVth ventricle and its surroundings were measured with two Clark-type microelectrodes. The electrodes had a tip diameter of 10 µm, and possessed an internal Ag/AgCl reference anode, which increased resolution and allowed 90 % response time in less than 1 s. Calibration of the electrodes, an example of one such calibration is shown in Fig. 3.8, was performed before each experiment with the following solutions (detailed calculations of the O_2-concentration can be found in App. A.3):

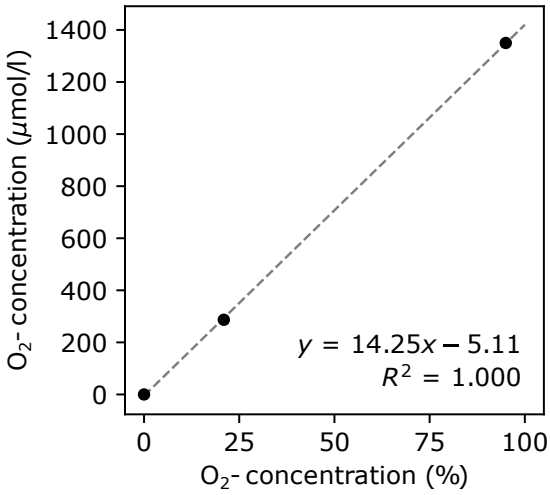

Figure 3.8.: Calibration curve for the oxygen sensors – Calibration curve was made with Ascorbic acid (0), air-saturated Ringer (286 µmol/l), and carbogenized Ringer (1350 µmol/l). The linear oxygen calibration line allows to calculate the concentration for any measured value.

- For 0 O_2: 0.1 mol/l Ascorbic acid in 0.1 mol/l NaOH at 18 °C
- For 286.85 µmol/l O_2: 18 °C Ringer solution, air-saturated
- For 1350 µmol/l O_2: 18 °C Ringer solution, carbogenized.

For the experiments, the electrodes were positioned in the bath chamber as well as in the open and accessible IV$^{\text{th}}$ ventricle without touching the brain tissue. Extracellular pH was measured with a pH microelectrode with a tip diameter of 10 µm and a separate reference electrode, a thick open-ended Ag-AgCl electrode with a gel-stabilized electrolyte. Calibration was performed at the beginning of each experiment with solutions of known pH 4, 7, and 9 from Roth, see App. A.1.

For temperature monitoring, a microelectrode (TP-200) was used. This microelectrode consisted of a tapered glass capillary with a mineral insulated thermo-coupler inside. The sensor was calibrated with Ringer solution at various temperatures prior to the experiment.

The current output of all electrodes was converted by a UNISENSE A/S analog converter [128] and fed into a CED Micro3 1401 data acquisition unit, to record all inputs with the Spike2 software [131]. The output from the nerve recording electrode was fed into a polarographic amplifier, and further into an acquisition unit. This gave immediate output of discharge rate, pH, temperature, and O_2-concentrations in the bath and the IV$^{\text{th}}$ ventricle. All electrodes were attached to micromanipulators for precise positioning in the experimental setup. The oxygen electrodes were attached to motorized microma-

nipulators (Sensapex, Finland), enabling to manipulate the electrode in the x-, y-, and z-direction, for precise positioning of the electrodes within the IVth ventricle and the bath.

3.5. Data Analysis

Discharge rates of the superior oblique (trochlear) motor nerve were obtained from multi-unit spike activity using Spike2 (Cambridge Electronic Design, UK) scripts. Spike rates were counted by all events reaching a threshold (1.5× the amplitude of the noise level). Multi-unit discharge rates were plotted with a bin width of 1 s to exclude spontaneously appearing spike bursts. More detailed analysis of spike bursts and the resulting oxygen drop were processed and analyzed using Python. The integral of bursts and O_2-consumption (resulting from a burst) was determined as area under the curve, limited by the onset condition, as given baseline. The O_2-consumption was determined by subtracting the ventricular oxygen value from the respective bath concentration. Spike discharge activity and concurrent O_2-concentration dynamics were processed and analyzed statistically using Microcal Origin 6.0 (OriginLab Corp., USA). Statistical differences were calculated with the Wilcoxon signed-rank test (paired parameters) and the Mann-Whitney U-test (unpaired parameters; Prism, Graphpad Software, Inc, USA).

4. Experimental Results

This chapter presents the experimental results for monitoring O_2-concentration in semi-intact *in vitro* preparations of *Xenopus laevis* larvae (Sec. 4.1), their neuronal contribution to O_2-consumption in the brain (Sec. 4.2), and the application of algae or cyanobacteria to enhance oxygen supply (Sec. 4.3). Part of the data from Sec. 4.1 and Sec. 4.2 are published in Özugur *et al.* Ref. [132].

Sec. 4.1 reports the O_2-concentration around the *in vitro* preparation. In Sec. 4.1.1, the O_2-concentration around the preparation, the z-stack plane through the IV$^{\text{th}}$ ventricle, as well as inactivated (dead) brain samples as a control were measured. Oxidative phosphorylation (OXPHOS) was inhibited with 500 µmol/l potassium cyanide (KCN), which blocks mitochondrial cytochrome-c-oxidase. Further, in Sec. 4.1.2, external O_2-concentration in the Ringer solution was increased and the concentration of oxygen in the ventricle in correlation to the O_2-concentration in the bath was analyzed. Additionally, O_2-concentrations in the brain tissue and in the vestibular nuclei were measured and the diffusion duration of oxygen into the brain tissue and the ventricle, covered by or without the choroid plexus, was calculated. In Sec. 4.1.3, the brain's oxygen needs were evaluated by increasing external O_2-concentrations in the Ringer solution to various levels and by monitoring the respective ventricular O_2-concentrations.

In order to test how oxygen is consumed by specific metabolic cycles, Sec. 4.2 discusses how drugs were used to block specific pathways. Neuronal processing was inhibited in Sec. 4.2.1 by 0.5 % and 0.05 % 3-aminobenzoic acid ethyl ester methane sulfonate (MS-222), which block sodium (Na) channels and interfere with signal processing. Furthermore, the recovery from MS-222 and the correlation of discharge rates and O_2-consumption were studied. Besides inhibition of nerve activity, in Sec. 4.2.2 the increased firing rate by bursts and their effect on O_2-consumption in the IV$^{\text{th}}$ ventricle were investigated under normal conditions, as well as during increased external oxygen levels.

Sec. 4.3 describes the use of photosynthesis to provide oxygen for *Xenopus laevis* preparations, with the algae *C.reinhardtii* and the cyanobacteria *Synechocystis*, respectively. First, maximal O_2-production and the EC_{50} values of isolated algae and cyanobacteria (0.5×10^9 cells/ml, 0.1×10^9 cells/ml) at different light intensities (5400 lux and 30 500 lux) were analyzed in Sec. 4.3.1. Then, in Sec. 4.3.2, algae and cyanobacteria were injected into

the vascular system of the *Xenopus laevis* larvae prior to the isolation of the preparation. The distribution in the brain was visualized with confocal imaging. Further, in Sec. 4.3.3, O_2-production upon light illumination in the ventricle of injected preparations was measured and compared to injections of photomutant algae or cyanobacteria, which lack the Photosystem II (PS II), and therefore the ability to produce oxygen. The advantage of intrinsic oxygen supply from algae and cyanobacteria inside brain blood vessels was verified by monitoring neuronal activity under hypoxia.

4.1. O_2-Concentration in the Semi-Intact *In Vitro* Preparation

O_2-levels in the brain are a critical parameter for cell metabolism and therefore also influence neuronal function. To analyze the interrelation of oxygen availability and neuronal activity or the O_2-need of the brain, first a general O_2-concentration analysis helps to get a better understanding of the oxygen dynamics in the amphibian brain. In Sec. 4.1.1 O_2-concentration measurements of the semi-intact *in vitro* preparation gives information about the distribution of the oxygen in the vicinity of the tissue and the brain under air-saturated Ringer conditions. This is in Sec. 4.1.2 further investigated with metabolic inactive brains. Further, increasing external O_2-levels and simultaneously measuring the O_2-concentration at the floor of the IV$^{\text{th}}$ ventricle showed different oxygen dynamics. The brain O_2-consumption under various external Ringer levels is calculated in Sec. 4.1.3 and provides basic knowledge for further experimental approaches.

4.1.1. Oxygen Depletion in the IV$^{\text{th}}$ Ventricle

An oxygen depth profile (z-stack) across the IV$^{\text{th}}$ ventricle and around the preparation was constructed, as shown in Fig. 4.1. The oxygen map was obtained by recording 31 animals. Measured concentrations (white circles) and interpolation between the measured points revealed the distribution of the O_2-concentration. The data show the highest oxygen value in the bath Ringer solution [(292 ± 4) µmol/l, mean $\pm$ standard error of the mean (SEM)], with a decrease in the vicinity of the tissue and a complete depletion at the ventricular floor (0). This suggests that oxygen is consumed by the brain and the adjacent tissue, and uses all oxygen available in the surrounding Ringer solution. Fig. 4.2 shows one example of a stepwise measurement along the depth track in the midline of the brain, which was used to obtain the oxygen map in Fig. 4.1. The continuous oxygen readout during repositioning the ventricular electrode from the bottom of the IV$^{\text{th}}$ ventricle, stepwise in 0.2 mm in the y-direction up to 1.4 mm above the preparation is shown in Fig. 4.2 a). The bath

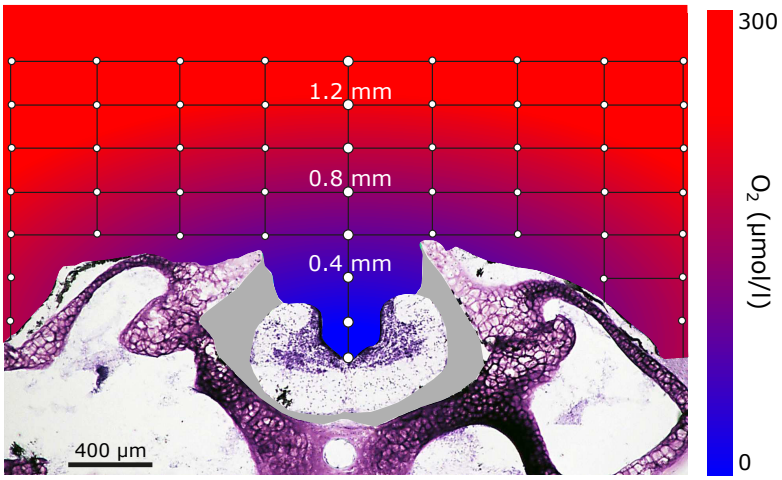

Figure 4.1.: O_2-concentration map around the semi-intact *in vitro* preparation of *Xenopus laevis* – Two-dimensional oxygen map showing oxygen levels around and within the IV$^{\text{th}}$ ventricle, measured in $0.2\,\text{mm}$ steps (white circles). Coronal section through the head of the preparation showing the location of measurement points. White dots depict the measurement points of the oxygen electrode. The color-coded O_2-concentration gradient is depicted on the right, starting from 0 (blue) to $300\,\mu\text{mol/l}$ (red). The regions between the points of measurement ($n = 31$) were interpolated. Figure modified from Ref. [132].

electrode remained at a fixed position and monitored the O_2-concentration in the Ringer solution, which was kept constant. There is a gradual reduction in O_2-concentration as the ventricular electrode moves towards the ventricle floor. A linear relation between the ventricle depth and the O_2-concentration between $0.2\,\text{mm}$ and $0.8\,\text{mm}$ distance to the ventricle floor was observed, see Fig. 4.2 b). As a control, non-functional brain samples (EtOH) were monitored and are depicted in grey, see Fig. 4.2 b). Control measurements such as EtOH treated brains are discussed in the next paragraph, cf. Sec. 4.1.2. The results suggest that the most prominent change in O_2-concentration as a function of distance is between $0.2\,\text{mm}$ and $0.8\,\text{mm}$. This indicates that in the brain around the ventricle, cells consume all available oxygen. The high O_2-consumption in the IV$^{\text{th}}$ ventricle is why the prospective focus was on the depth track in the ventricle. To verify if the measured oxygen depletion is due to brain activity and not due to a morphological diffusion barrier, the measurements were repeated on dead brain samples via two approaches shown in Fig. 4.2 b) and Fig. 4.3. In the first approach the brain was deactivated before the experiment by EtOH treatment of the preparation ($n = 7$), and in the second approach the brain was deactivated in-situ through bath application of $500\,\mu\text{mol/l}$ KCN ($n = 8$). In EtOH deactivated brains, the O_2-concentration in the ventricle was constant and independent of the distance to the ventricle floor, see Fig. 4.2 b). In the following, O_2-concentrations were measured with one electrode at the lowest position in the IV$^{\text{th}}$ ventricle (position

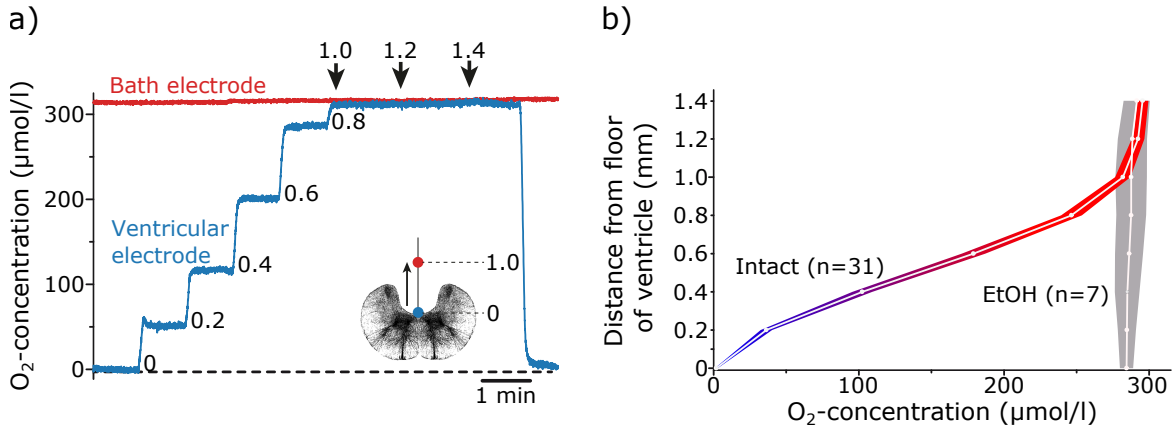

Figure 4.2.: O_2-concentration as a function of the distance to the ventricular floor – The O_2-consumption in the z-stack of one animal is depicted in a) where the oxygen level was measured in $0.2\,\mathrm{mm}$ steps. The inset at the bottom right corner illustrates the position of the electrodes in the ventricle (0 (blue) and $1.0\,\mathrm{mm}$ (red) above the ventricular floor). b) Average of the O_2-concentration of 31 animals in the depth track into the IV$^{\mathrm{th}}$ ventricle. The oxygen level and the distance to the ventricular floor depict an s-shaped dependency. The mean of $31\,\mathrm{animals}$ is illustrated as white circles and the error by the width of the color coded line. The same color code as in Fig. 4.1 is used. As control, dead brain samples (EtOH-fixed) were monitored the same way and are depicted in grey (n = 7), with mean data (white circles and line) and corresponding error (width of the grey shading). Figures modified from Ref. [132].

0), and the second electrode in the bath (position 1 0) to monitor the surrounding Ringer O_2-concentration. In EtOH treated brains, the O_2-concentrations at the ventricular floor remained at the same concentration as the electrode in the surrounding Ringer solution. This indicates metabolic inactivity, leading to an oxygen leftover in the IV$^{\mathrm{th}}$ ventricle. The same effect was observed when KCN, an inhibitor of OXPHOS (one of the oxygen dependent cycles and major ATP source), was applied. In both sets of experiments, when applying a higher external O_2-concentration ($> 500\,\mu\mathrm{mol/l}$), see Fig. 4.3 a) and b), it takes $\sim 15\,\mathrm{min}$ $[(14.8 \pm 0.3)\,\mathrm{min};\ n = 6]$ for an equalization of ventricular- and bath O_2-concentration in the Ringer. The effect of a delayed but matching augmentation is also observed during the return of the O_2-concentration to air-saturated Ringer levels ($\sim 290\,\mu\mathrm{mol/l}$, see Fig. 4.3 a). Moreover, EtOH and KCN deactivated preparations show the same values for the ventricular and bath Ringer oxygen, see Fig. 4.3 c). This is also true for higher external O_2-concentrations as shown in Fig. 4.3 d). As expected from dead brain samples, these results show that the preparation no longer uses the available oxygen, hence indicating that metabolic activity is absent.

It was shown that the oxygen depletion in the vicinity of the tissue, especially in the IV$^{\mathrm{th}}$ ventricle, is due to the O_2-consumption by the brain. Under air-saturated Ringer

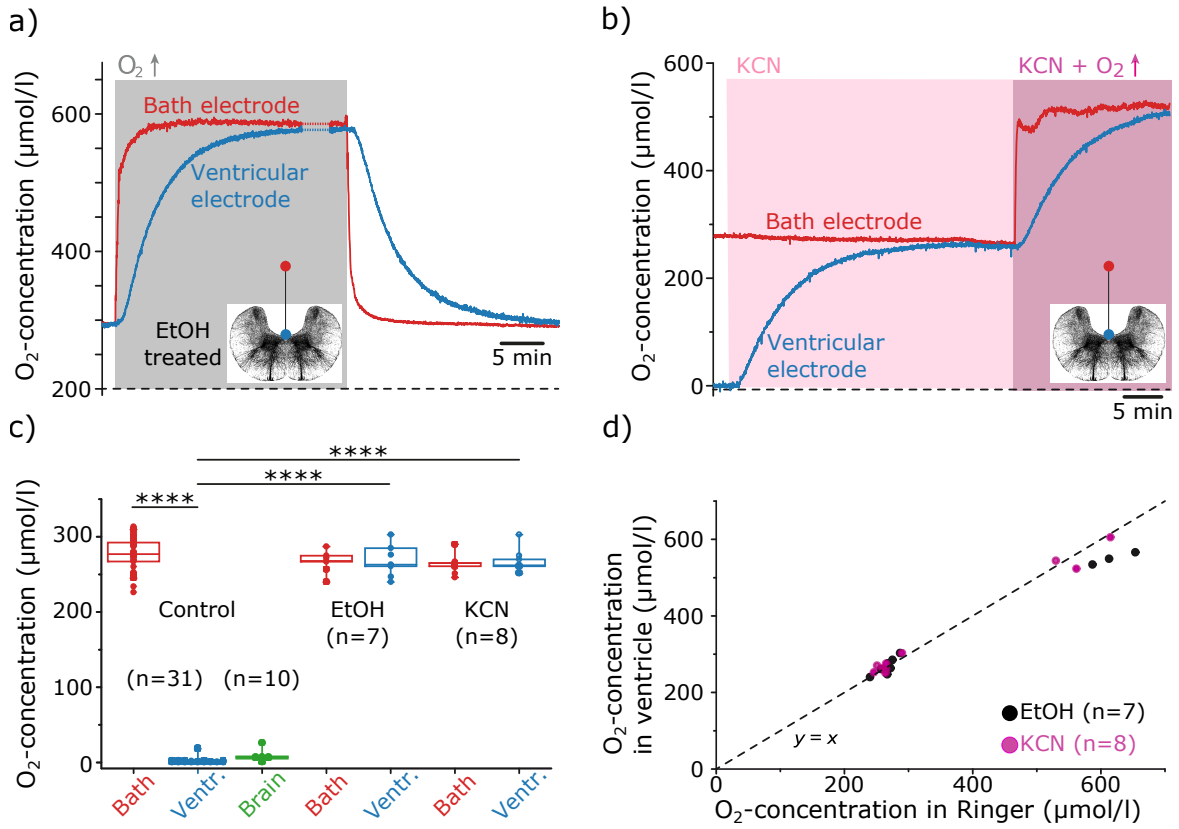

Figure 4.3.: Oxygen measurements in metabolically inactive brain samples – Oxygen was measured at the ventricular floor in metabolically inactive brain samples (EtOH fixed and KCN in-situ deactivated). a) Temporary increase in bath oxygen from $\sim 290\,\mu\mathrm{mol/l}$ up to $\sim 600\,\mu\mathrm{mol/l}$ (grey shaded) of an EtOH deactivated brain. It shows that the oxygen level in the IV$^{\mathrm{th}}$ ventricle rises with a small delay and further shows the same effect after returning to normal air-saturated Ringer levels. b) Inhibition of OXPHOS with KCN ($500\,\mu\mathrm{mol/l}$, pink shaded) caused a rise of the oxygen value in the ventricle, as bath oxygen levels remained constant. Additionally supplied oxygen increases in the presence of KCN (dark pink shaded) augments the O_2-concentration in the IV$^{\mathrm{th}}$ ventricle further until it reached bath levels. c) O_2-concentrations in the bath (red) and the ventricular floor (blue) in untreated active preparations (control), and in EtOH and KCN inactivated preparations. Ventricular differences are shown in control and inactive samples (EtOH and KCN, **** $p \leq 0.0001$; Mann-Whitney U-test). d) O_2-concentration in the ventricle as a function of the bath O_2-concentration shows a linear relationship ($y = x$) for both, metabolic inactive (EtOH) and OXPHOS impaired (KCN) samples. Figures modified from Ref. [132].

levels (∼290 µmol/l O_2), all available oxygen is decreased in the vicinity of the tissue of the preparation, and starts to drop drastically at around 0.8 mm distance to the ventricular floor, and was fully depleted in the depth of the IV^{th} ventricle, see Fig. 4.1. Oxygen depletion along the depth track of the IV^{th} ventricle in intact preparations is not linear, but s-shaped as a function of the distance to the ventricle floor, with the lowest O_2-concentration at the ventricle floor, and the highest in the distant Ringer solution, > 1 mm from the ventricular floor, see Fig. 4.2 a) and b). Based on the results obtained in metabolically inactive brain samples, see Fig. 4.2 b) and Fig. 4.3, the oxygen consumption as shown in Fig. 4.1 derives from metabolic activity in the brain.

4.1.2. Increased External Ringer O_2-Concentration

The results shown in Fig. 4.1 indicated that oxygen is fully depleted within the IV^{th} ventricle. This raised the question whether more oxygen could be used by the brain if more oxygen is available within the IV^{th} ventricle. Accordingly, higher external O_2-concentrations were applied to the bath Ringer solution, i.e. ∼ 550 µmol/l, ∼ 750 µmol/l, and ∼ 950 µmol/l, and the concentration was measured with one oxygen electrode in the bath and another at the bottom of the IV^{th} ventricle. The ventricular electrode was moved in between the y-positions 0 and 1.2 mm as a distance to the ventricular floor (z-stack), as shown in Fig. 4.4. When the external oxygen was increased, the ventricular electrode remained at the lowest position in the ventricle (position 0) until the O_2-concentration in the ventricle was increased and reached a steady state (∼ 100 µmol/l, ∼ 150 µmol/l, and ∼ 300 µmol/l, respectively). A brief control of the O_2-concentrations in the bath was performed by retracting the electrode in the ventricular zone, in steps of 0.2 mm, to 1.2 mm above the ventricular floor.

Fig. 4.5 shows the oxygen dynamics along the depth track of the IV^{th} ventricle when increasing external Ringer oxygen levels. The data shows a rightward shift of the oxygen dependence curve (s-shape) in regard to ventricular depth (z-stack) to higher oxygen levels, as seen in Fig. 4.5 a). The characteristic s-shape, presented previously in Fig. 4.2 b), does not change if more oxygen is available in the surrounding Ringer solution. Different external O_2-concentrations were applied, i.e. 290 µmol/l, 550 µmol/l, 750 µmol/l, and 950 µmol/l, and O_2-levels along a depth track of the ventricle monitored in 0.2 mm steps. The shape of the oxygen diffusion, when plotting the O_2-concentration against electrode position in the ventricular zone, appears to be independent from external oxygen levels. Further, the O_2-concentration at the bottom of the ventricle is linearly related to the concentration in the Ringer solution when greater than 700 µmol/l O_2, see Fig. 4.5 b). This result suggests that above this level the brain is not consuming more oxygen if more

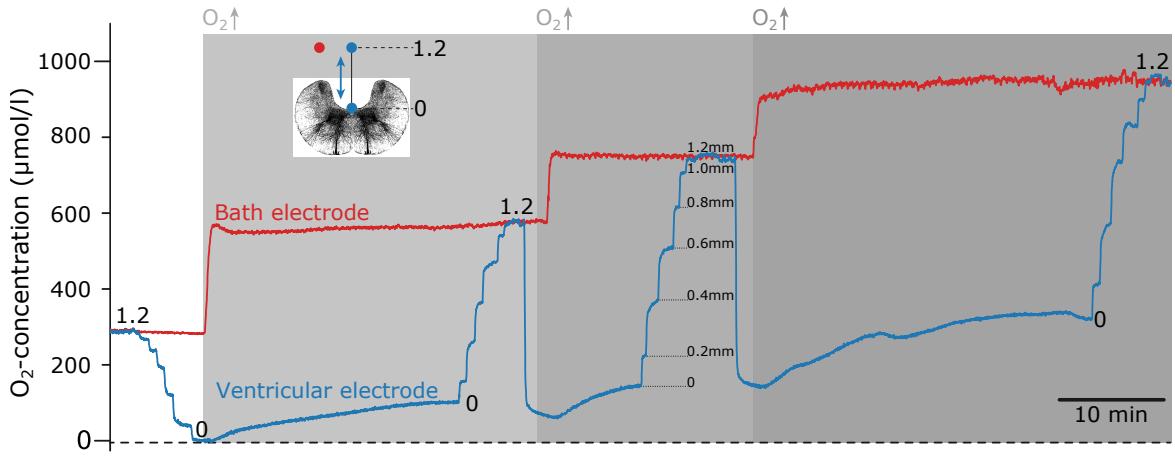

Figure 4.4.: Example recording of stepwise increased O_2-concentration in the Ringer solution – Oxygen levels measured with one electrode in the bath chamber (red trace) and another electrode in the IV$^{\text{th}}$ ventricle (blue trace). The ventricular electrode was moved in $0.2\,\text{mm}$ steps (z-stack) from the bottom of the ventricular floor (0 position) to $1.2\,\text{mm}$ above. Continuous measurement of oxygen levels at the ventricular floor during external oxygen application in three steps (see red trace), i.e. $\sim 550\,\mu\text{mol/l}$, $\sim 750\,\mu\text{mol/l}$, and $\sim 950\,\mu\text{mol/l}$ (grey shaded), increased the ventricular O_2-level to $\sim 100\,\mu\text{mol/l}$, $\sim 150\,\mu\text{mol/l}$, and $\sim 300\,\mu\text{mol/l}$. Figure modified from Ref. [132].

is available, but has an upper limit in O_2-consumption. Below this limit, oxygen provided by diffusion from external oxygen is not sufficient to reach brain oxygen saturation levels. If the Ringer oxygen level was higher than $\sim 700\,\mu\text{mol/l}$ O_2, the leftover oxygen obviously remains unused for brain metabolism and remains in the ventricular zone. This explains the linear increase of ventricular oxygen, above $\sim 700\,\mu\text{mol/l}$ O_2 in the Ringer solution. Due to this finding, in the following experiments external oxygen levels were increased above $700\,\mu\text{mol/l}$ to provide a condition in the ventricle where surplus oxygen was available. The increased external oxygen level avoided an oxygen undersaturation in the brain. Additionally, it was confirmed that oxygen levels in the brain tissue (green dots) have the same concentration as measured in the IV$^{\text{th}}$ ventricle (black dots) as can be seen in Fig. 4.5 b). This is also true for higher external oxygen levels. The idea of introducing the electrode into the brain was to provide an oxygen readout in close apposition to the area of O_2-consuming motor and premotor nuclei, which directly project to the eye muscle nerves where neuronal activity was recorded, subsequently see Sec. 3.1.1.

Fig. 4.6 shows the O_2-diffusion in the brain tissue and the ventricle, without and with a blood plexus, when increasing external O_2-concentration. Higher oxygen levels in the Ringer solution have no significant influence on the O_2-diffusion duration in the brain

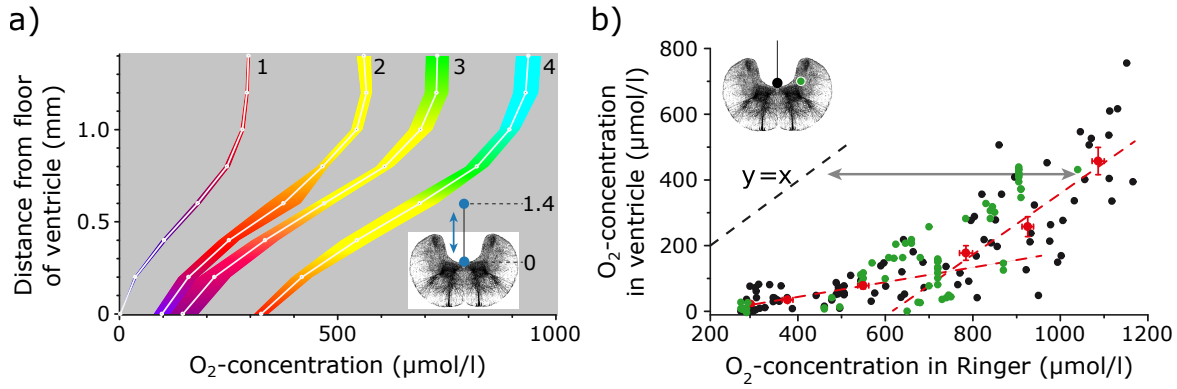

Figure 4.5.: Increased external oxygen levels in the Ringer solution – O_2-concentration in the IV^{th} ventricle in correlation to a) electrode position at different distances to the ventricular floor and b) O_2-concentration in the Ringer solution. a) Depth profile of oxygen from the ventricular floor to $1.4\,\mathrm{mm}$ above the ventricle (z-stack). Increasing external oxygen levels from $290\,\mu\mathrm{mol/l}$, n = 31 (1), to $550\,\mu\mathrm{mol/l}$, n = 6 (2), $750\,\mu\mathrm{mol/l}$, n = 6 (3), and $900\,\mu\mathrm{mol/l}$, n = 6 (4), leading to a shift in O_2-concentrations in the ventricular zone. Color coded O_2-concentration depicts in purple: 0 - $200\,\mu\mathrm{mol/l}$, red: $200\,\mu\mathrm{mol/l}$ - $400\,\mu\mathrm{mol/l}$, yellow: $400\,\mu\mathrm{mol/l}$ - $700\,\mu\mathrm{mol/l}$, cyan: $> 700\,\mu\mathrm{mol/l}$. The mean is depicted as white circles of each group and the error of each measurement point is indicated by the width of the color coded area, respectively. b) Ventricular O_2-concentration dependency on external oxygen levels in the Ringer. Applying $\sim 700\,\mu\mathrm{mol/l}$ O_2 or more, the O_2-concentration in the ventricle increase linearly as a function of oxygen in the Ringer. Oxygen in the ventricle was measured at the ventricular floor (black) and in the brain tissue in the region of the vestibular nuclei (green), as shown in the inset in the top left corner. Red dots represent the mean $\pm$ SEM of the ventricular O_2-level at distinct bath O_2-concentrations and red dashed lines represent the linear regression through lower ($y = a + 0.25x$; $R^2 = 0.98$) and higher ($y = a + 0.93x$; $R^2 = 0.96$) mean ventricular concentrations, respectively. Ventricular measurements (black dots) $n = 97$ measurements from 24 preparations. Brain tissue (green dots) $n = 69$ measurements from 11 preparations. Figures modified from Ref. [132].

tissue and the ventricle, independent of the presence or absence of the choroid plexus above the IV^{th} ventricle.

It was shown that increasing external oxygen levels in the bath caused a delayed increase of the O_2-concentration at the ventricular floor, cf. Fig. 4.4. There seems to be a point where oxygen saturation in the ventricular zone is reached during increased levels of external bath oxygen, cf. Fig. 4.5 b). This saturation point is the same when measuring the oxygen in the vestibular nucleus or the ventricle. There is no significant difference of O_2-diffusion duration in the three locations (vestibular nucleus, ventricle without plexus, and ventricle with plexus), indicating that the choroid plexus presents no physical barrier for oxygen, cf. Fig. 4.6. The methodological approach was to monitor oxygen levels in the ventricle and not in the brain tissue, and thus prevent tissue or cell damage which

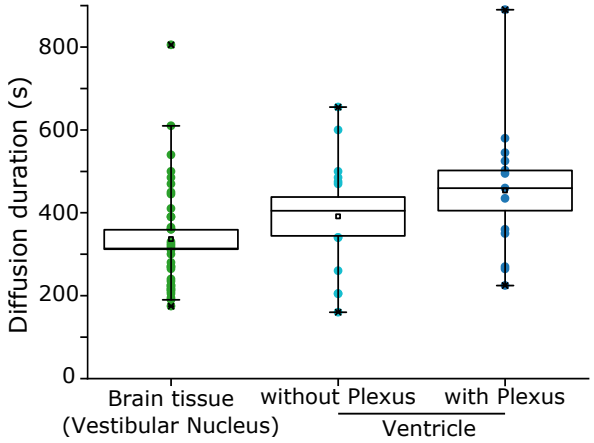

Figure 4.6.: Oxygen diffusion duration into the ventricle – Diffusion duration in seconds during application of higher oxygen levels into the bath Ringer solution, measured in the vestibular nucleus (green, (336.50 ± 136.12) s), the ventricular floor without choroid plexus (cyan, (391.25 ± 163.01) s), and the ventricular floor with choroid plexus above (blue, (454.08 ± 174.51) s).

occurs when inserting the electrode into the brain. Since there is no difference in O_2-concentration in the ventricle or the vestibular nuclei, the oxygen levels monitored at the ventricular floor corresponds to the levels in the anatomically adjacent vestibular nuclei.

4.1.3. Brain O_2-Consumption

As seen in Fig. 4.5 b), the brain's demand for oxygen has not reached its limit at normal air-saturated Ringer levels ($\sim 290\,\mu$mol/l), but only when the Ringer levels were above $\sim 700\,\mu$mol/l. In the following, the exact O_2-concentration of the brain's oxygen demand is calculated to estimate its oxygen needs. Accordingly, the difference of oxygen levels in the bath ($> 700\,\mu$mol/l) and the IV$^{\text{th}}$ ventricle was measured for 90 animals as shown in Fig. 4.7. The arithmetic mean for O_2-consumption is $626\,\mu$mol/l O_2 [Fig. 4.7 a)], and is independent of external Ringer solution [Fig. 4.7 b)].

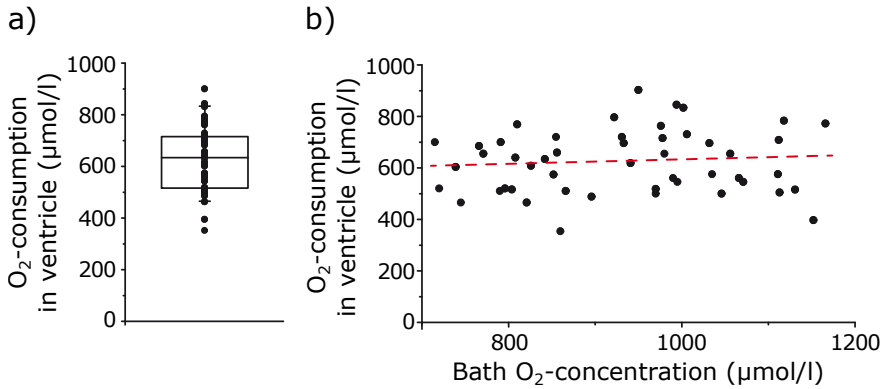

Figure 4.7.: Brain oxygen consumption – a) Mean value of brain O_2-consumption is $(626 \pm 120.7)\,\mu\mathrm{mol/l}$. b) The brain O_2-consumption is not correlated with the external O_2-concentration in the Ringer solution, O_2-concentration min: $715\,\mu\mathrm{mol/l}$, O_2-concentration max: $1166\,\mu\mathrm{mol/l}$. Linear regression (dashed line): $m = 0.0821$, $R^2 = 0.0073$, $p = 0.4241$, $n = 90$ measurements from 13 preparations. Thus, the slope of the regression line is not significantly different from zero. Figures modified from Ref. [132].

4.2. Correlation between O_2-Consumption and Neuronal Activity

Sec. 4.1 established that the brain is responsible for the oxygen depletion in the ventricular zone. Here, the focus is on the neuronal contribution to the consumption of oxygen. A reasonable assumption is that the major oxygen consumers are neurons, and thus OXPHOS, as major energy providing source, is the major oxygen consuming pathway. Since the neuronal discharge is dependent on oxygen availability, neuronal discharge and O_2-concentration was simultaneously monitored to determine a correlation between neuronal activity and O_2-consumption. Therefore, the discharge of the trochlear motor nerve, one of the extraocular motor nerves that innervates the superior oblique eye muscles, was monitored simultaneously with the O_2-concentration in the IV$^{\text{th}}$ ventricle. As shown before, metabolically inactive brains led to an increase in O_2-concentration in the ventricle. In Sec. 4.2.1 this will be further investigated with regard to neuronal inhibition. In Sec. 4.2.2 the O_2-consumption during spontaneous appearing bursts, which resulted in a drop of the O_2-concentration in the ventricle, is analyzed.

4.2.1. Inhibition of Neuronal Activity

Functional nerve activity of the trochlear motor nerve was recorded as a proxy for neuronal activity in the brain. Fig. 4.8 shows an example recording following blocking of nerve firing activity by application of 3-aminobenzoic acid ethyl ester methanesulfonate (MS-222) and how the O_2-concentration and the resulting O_2-consumption in the ventricle is influenced by this inhibition. Inhibition of sodium (Na) channels by 0.5 % MS-222, an inhibitor of the fast sodium conductance, and frequently used in amphibians and fish, prevented nerve firing after 1 min, as can be seen in Fig. 4.8 a). During application of 0.05 % MS-222 for 20 min, O_2-consumption in the IV$^{\text{th}}$ ventricle decreased, followed by a fast recovery to normal O_2-concentrations shortly after washing out of the inhibitor, see Fig. 4.8 b). The maximum treatment time for MS-222 application was 40 min for 0.05 % MS-222 and 10 min for 0.5 % MS-222. The O_2-concentration at the ventricular floor was significantly higher in the presence of 0.05 % MS-222 and even higher in the presence of 0.5 % MS-222, compared to control values in the ventricle, as shown in Fig. 4.9 a). The dependency of the O_2-concentration on the ventricular position (z-stack) showed a steep shift to higher O_2-concentrations with 0.05 % MS-222 and even bigger effects with 0.5 % MS-222, Fig. 4.9 b). This demonstrates that the block of sodium channels has an effect on nerve firing activity as well as on O_2-consumption in the IV$^{\text{th}}$ ventricle.

Fig. 4.8 shows that blocking neuronal activity with a sodium channel blocker (0.5 %

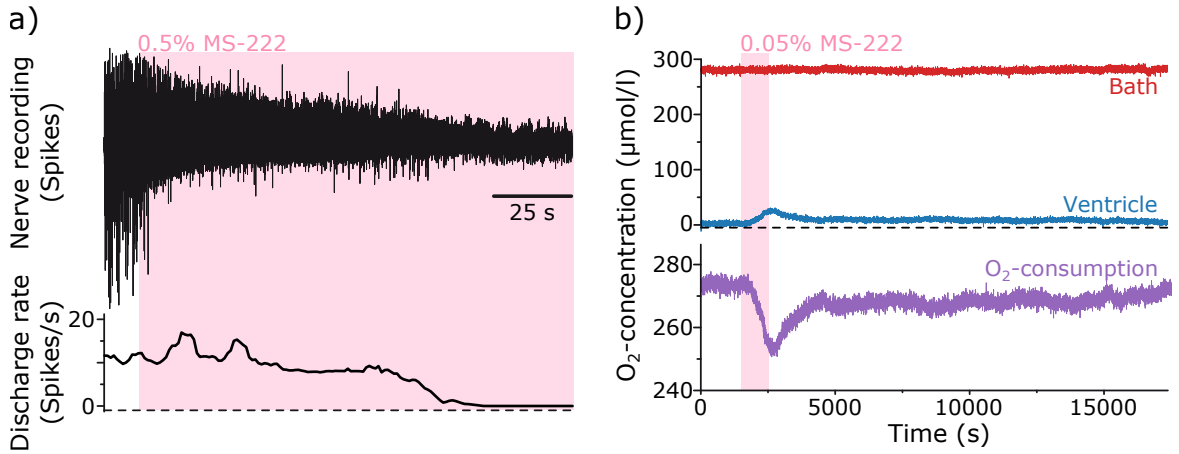

Figure 4.8.: Neuronal inhibition – The effect of $0.5\,\%$ and $0.05\,\%$ MS-222 on discharge rate (Spikes/s) and O_2-concentration in the ventricle. a) Example recording of $0.5\,\%$ MS-222 application (pink shaded), caused an immediate decrease of the discharge rate (Spikes/s), culminating in a complete loss soon afterwards. Recorded spikes are shown as black trace (Nerve recording) along with the corresponding discharge rate. b) Effect of $0.05\,\%$ MS-222 application for $20\,\mathrm{min}$ (pink shaded area) on the O_2-concentration (blue) and resulting O_2-consumption (purple) in the ventricle, while the bath O_2-level (red) remained constant.

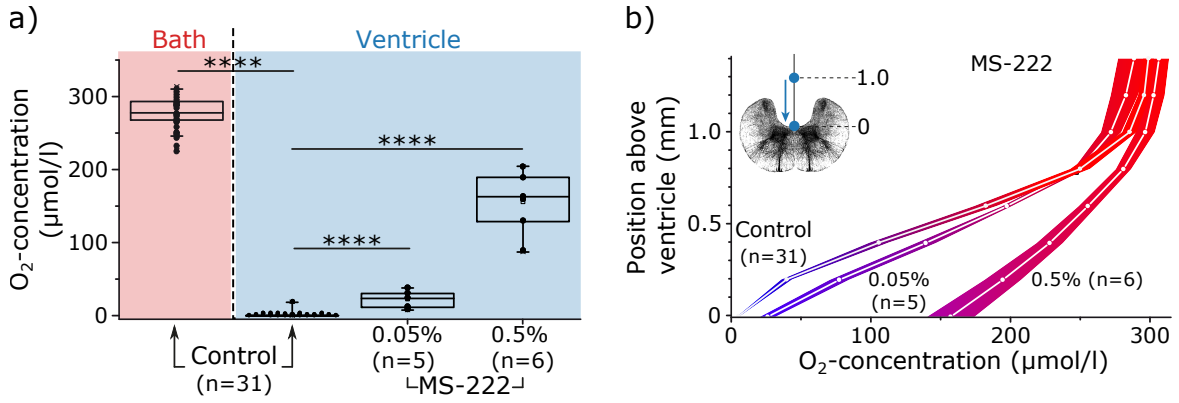

Figure 4.9.: Effect of MS-222 on the O_2-concentration in the ventricle – a) Bath O_2-levels (red shaded) and corresponding O_2-concentration in the ventricle (blue shaded) in controls, following $0.05\,\%$ MS-222 application for $40\,\mathrm{min}$, and $0.5\,\%$ MS-222 for $10\,\mathrm{min}$. Ventricular oxygen had significantly higher levels after $0.5\,\%$, and $0.05\,\%$ MS-222 application, compared to the control condition. **** $p \leq 0.0001$; Mann-Whitney U-test. b) O_2-concentration in the IV$^{\mathrm{th}}$ ventricle, as depth track in correlation to electrode position in the ventricle in controls, after $0.5\,\%$ and $0.05\,\%$ MS-222 application. White dots depict the measurement points ($0.2\,\mathrm{mm}$ steps) as mean values and the error is shown by the width of the color coded area in each condition as shown before in Fig. 4.5. Figures modified from Ref. [132].

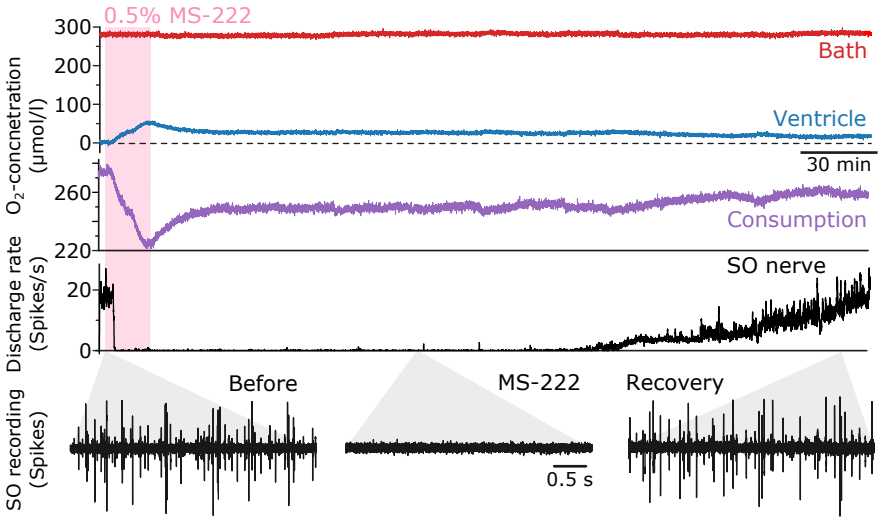

Figure 4.10.: Neuronal blockade and recovery from MS-222 – Recording showing the effect of 0.5 % MS-222 application for 10 min (pink shaded area) on the O_2-concentration in the IV^{th} ventricle (blue trace), and resulting O_2-consumption (purple trace), while the bath O_2-concentration (red trace) was kept constant. Spike activity of the trochlear motor nerve is shown as discharge rate (Spikes/s) (black trace), with higher magnifications to highlight the nerve activity before MS-222 treatment ('Before'), during the inhibition ('MS-222'), and during wash-out ('Recovery' - bottom, grey shaded areas). Figure modified from Ref. [132].

and 0.05 % MS-222, respectively) caused an increase in the O_2-concentration in the IV^{th} ventricle. This indicates that neuronal activity is responsible at least for part of the O_2-consumption in the brain and therefore responsible for the oxygen depletion in the ventricular zone seen in Fig. 4.1. A more extended effect of MS-222 is shown in Fig. 4.10, illustrating an example recording where the O_2-concentration in the IV^{th} ventricle and the discharge rates of the extraocular motor nerve after MS-222 (0.5 %, 10 min) application were recorded. Application of 0.5 % MS-222 (pink shaded) caused a drop of the nerve activity and an increase in O_2-concentration in the IV^{th} ventricle. The O_2-consumption was calculated from the bath and ventricular O_2-concentrations. After inhibitor wash out, there was a relatively fast recovery of O_2-consumption, though the neurons remained inactive. In the late recovery phase, defined by the final washout of MS-222, a linear correlation between O_2-consumption and discharge rate was observed, as illustrated in Fig. 4.11 a) and b). This linear correlation during the later phase of the recovery is reproducible as can be seen Fig. 4.11 c). The neuronal discharge recovery coincided with a decrease of the O_2-concentration in the ventricular zone, indicating an increased O_2-consumption likely due to the re-established spike activity.

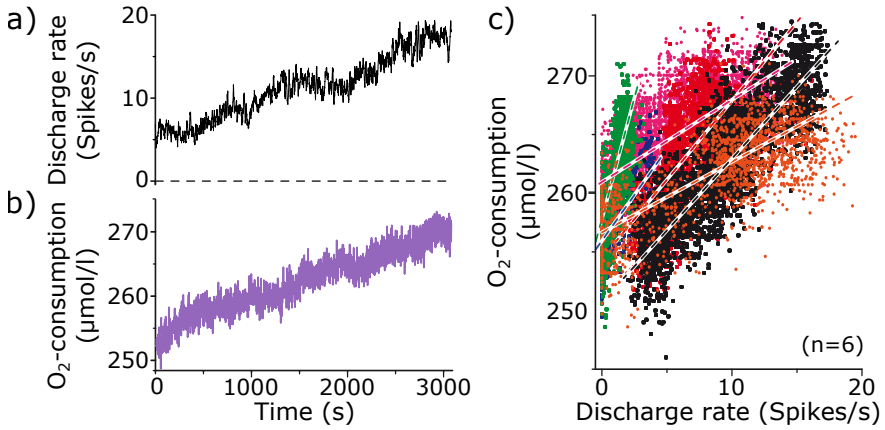

Figure 4.11.: Late recovery phase during $0.5\,\%$ MS-222 wash-out – a) Discharge rate (Spikes/s) and b) O_2-consumption increases during the recovery period. c) Ratios of discharge rate and O_2-consumption in different preparations ($n = 6$) are linearly correlated. Figures modified from Ref. [132].

4.2.2. Spontaneous Increase of Neuronal Activity

The previous experiments established that the loss of neuronal activity as well as the recovery thereof could be unequivocally correlated with O_2-consumption in the ventricle. Fig. 4.12 shows the increased oxygen need during spontaneously increased neuronal activity, so called spike bursts. During a burst, the neuronal discharge increases considerably while the O_2-concentration in IV$^{\text{th}}$ ventricle transiently decreases, see Fig. 4.12 a) - c), followed by a fast recovery of the O_2-concentration (~ 6 min) until it reaches normal pre-spike burst oxygen values again, see Fig. 4.12 c). The average ($n = 4$) of bursts [Fig. 4.12 d)] and O_2-consumptions [Fig. 4.12 e)] illustrate the reproducibility, and an O_2-consumption increase in the ventricular zone at higher nerve discharge rates. Further, analyzing the onset of a burst and the onset of the O_2-consumption, seen in Fig. 4.12 d) and e) (red arrow), shows that the onset of the O_2-consumption occurred when the maximum discharge rate was already reached. The O_2-consumption is at its maximum ~ 1 min after the onset, and slowly decreases thereafter. The delay of the O_2-consumption onset at the peak discharge could be explained by a diffusion effect, since the oxygen supply requires time to diffuse from the Ringer into the IV$^{\text{th}}$ ventricle. During a spike burst the oxygen in the IV$^{\text{th}}$ ventricle was fully depleted, cf. Fig. 4.12 c) suggesting that the air-saturation of the Ringer is not sufficient to cover the oxygen needs in the brain during a burst. As described above, the brain saturation level is ~ 626 µmol/l O_2, cf. Fig. 4.7. Therefore, external bath levels were increased and the O_2-consumption and the correlation with the neuronal activity was examined.

Fig. 4.13 shows the nerve activity during increased external oxygen levels of ~ 600 µmol/l

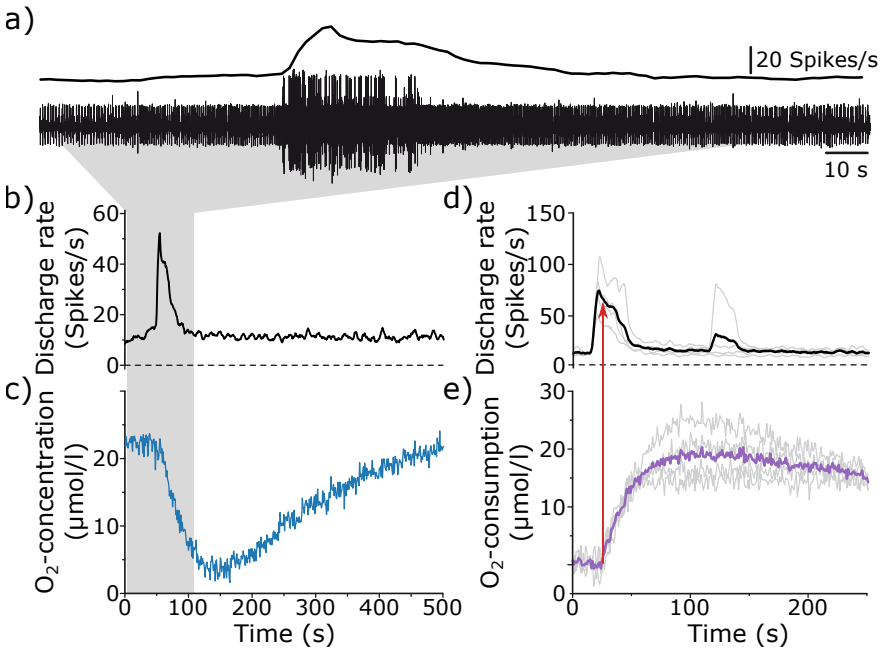

Figure 4.12.: O_2-consumption during increased spike activity, so called spike bursts – Nerve activity and O_2-concentration during spontaneously increased discharge rates. Magnified view of the recording [grey area in a)] shows increased discharge rates in b), which are accompanied by a simultaneous decrease of the O_2-concentration in the IV$^{\text{th}}$ ventricle in c). The recovery to pre-spike burst oxygen levels in the ventricle after a burst was $\sim 6\,\text{min}$. The average of 4 measurements (grey) and their mean (black/ purple) are plotted in d) discharge rate and e) O_2-consumption. Red arrow shows that the O_2-consumption increases when the peak discharge is already reached. Figures modified from Ref. [132].

O_2. At this point, the oxygen in the IV$^{\text{th}}$ ventricle was not fully depleted during a burst because higher levels of oxygen were available. This implies that the brain is not consuming all available oxygen during a spike burst, but rather that there is a limit in O_2-consumption. Further, during a shorter burst (Fig. 4.13, black trace, 3$^{\text{rd}}$ peak) the oxygen drop was smaller compared to that during a longer burst (black trace, 2$^{\text{nd}}$ peak), demonstrating a correlation between the duration of increased nerve firing and O_2-consumption. Fig. 4.14 shows the integral of the O_2-consumption curve for each burst at elevated oxygen levels. This integral describes the total O_2-consumption over the entire burst duration; and this integral will be called total O_2-consumption. The average discharge rate, see Fig. 4.14 a), O_2-consumption b), and O_2-concentration in the IV$^{\text{th}}$ ventricle c), were analyzed for 10 bursts. The total O_2-consumption at air-saturated Ringer oxygen level ($\sim 290\,\mu\text{mol/l}$) and during an increased bath O_2-concentration ($\sim 600\,\mu\text{mol/l}$) was calculated in d). Accordingly, higher bath oxygen levels were accompanied by higher total O_2-consumption, indicating that the O_2-consumption is larger if more oxygen is available.

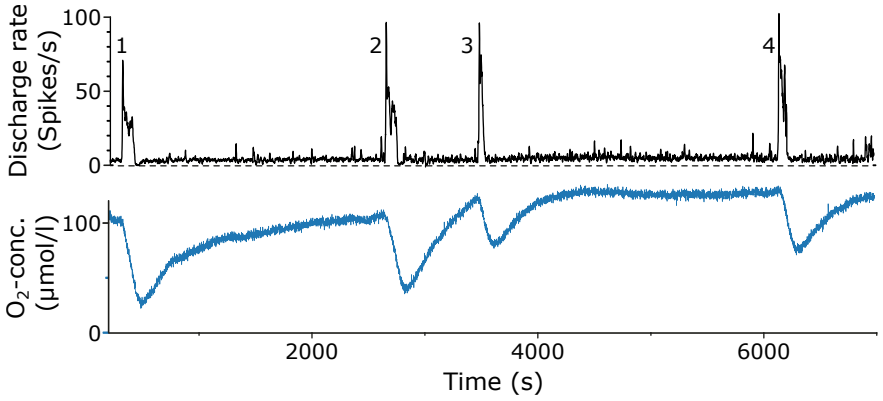

Figure 4.13.: Measurement of increased nerve activity during elevated Ringer O_2-concentration – Measurement of increased discharge rate (burst, black trace) and O_2-concentration at the ventricular floor (blue), during an increased external oxygen level ($\sim 600\,\mu mol/l$ O_2). Each burst provoked a drop of the O_2-concentration in the ventricle. A longer burst provoked a more pronounced drop in the O_2-concentration (see 2^{nd} burst in comparison to 3^{rd} burst). Figure modified from Ref. [132].

However, this could also arise from longer burst duration, as shown in Fig. 4.13. To evaluate this more closely, spontaneously occurring spike bursts were monitored under different Ringer O_2-concentrations, shown in Fig. 4.15. Different ventricular O_2-concentrations were analyzed; minimum: 0 O_2, maximum: 590 µmol/l O_2. The total O_2-consumption during a spike burst were grouped according to the total O_2-consumption magnitude during different bursts, i.e. a) $3000\,s \times \mu mol/l$, b) $5000\,s \times \mu mol/l$, c) $8000\,s \times \mu mol/l$, and d) $9000\,s \times \mu mol/l$. Each oxygen drop was normalized to indicate whether oxygen diffusion dynamics are dependent on different external oxygen levels. The figure clearly shows that independent of the O_2-consumption group [(3000, 5000, 8000, or 9000) $s \times \mu mol/l$] the oxygen recovery is similar during different Ringer oxygen levels. This suggests that the external oxygen level does not influence the diffusion dynamics in the IV^{th} ventricle.

Further, Fig. 4.16 shows the latency of the O_2-consumption onset after a burst appeared, for various ventricular oxygen levels. There is no variance in latency for the ventricular oxygen $(10 - 650)\,\mu mol/l$ O_2, which corresponds to $(290 - 1100)\,\mu mol/l$ O_2 in the Ringer solution. The distribution of the latency in relation to the ventricular O_2-concentration shows a linear trend, with similar values at lower and higher ventricular O_2-concentrations. The slope of the linear fit of the latency is not significantly different from zero ($p = 0.76$). This indicates that there is no relationship between the oxygen diffusion into the IV^{th} ventricle and the external O_2-concentration in the ventricle. In Fig. 4.16 b) the oxygen recovery time after an oxygen drop, caused by a burst, is shown. The recovery time is plotted against ventricular O_2-concentrations and was measured from the lowest point of the oxygen drop until oxygen values reached pre-burst values. The recovery time

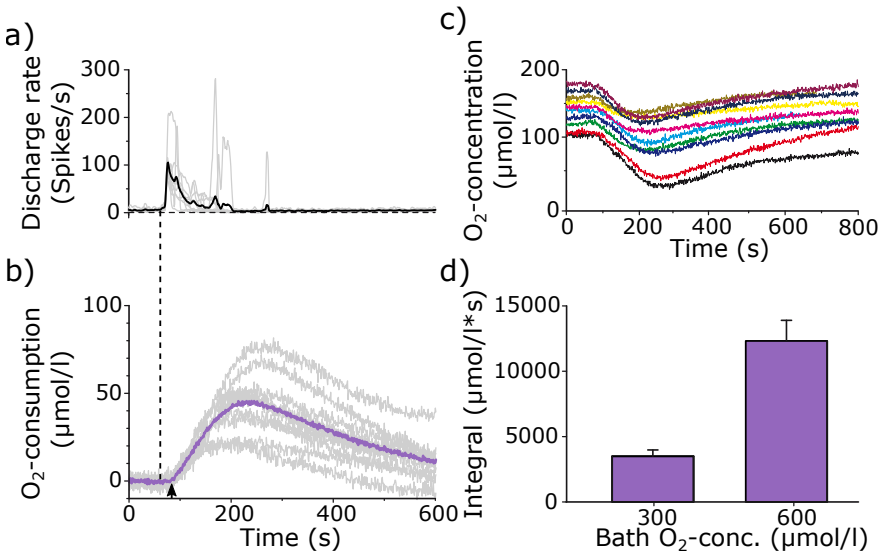

Figure 4.14.: Impact of spike bursts during increased external oxygen values – Average (n = 10) of discharge rates a), and O_2-consumption b), show higher amplitudes at $\sim 600\,\mu mol/l$ external oxygen levels, compared to air-saturated oxygen conditions ($\sim 290\,\mu mol/l$) d). c) Different oxygen drops during different discharge rates. Vertical dashed line and arrow in a) and b) represents the latency of the O_2-consumption onset and indicates the oxygen diffusion. Figures a) and b) modified from Ref. [132].

was normalized to the oxygen change during the drop. The lowest point of the oxygen drop was also the point when the burst has already ceased and no further oxygen was consumed, also shown before in Fig. 4.12 and Fig. 4.14. The recovery time, independent of the amount of O_2-consumption, was faster at higher ventricular O_2-levels. It was shown in Fig. 4.5 b) and Fig. 4.7 that the IV^{th} ventricle was saturated with oxygen $> 626\,\mu mol/l$, the prospective focus was on the oxygen recovery time for ventricular O_2-concentration with bath levels $> 626\,\mu mol/l$. $40\,\mu mol/l$ O_2 - $600\,\mu mol/l$ O_2 in the ventricle corresponded to $700\,\mu mol/l$ O_2 - $1100\,\mu mol/l$ O_2 in the Ringer solution. Brain oxygen levels were obviously saturated when the oxygen level in the Ringer was $> 626\,\mu mol/l$ and the time of oxygen recovery was likely related to oxygen diffusion. A slightly slower recovery dependent on ventricular O_2-concentration was observed, indicating that with higher oxygen levels the ventricular oxygen is refilled faster.

Next, the influence of increasing external oxygen levels on discharge rate will be discussed. Fig. 4.17 shows that the nerve activity is affected by the O_2-concentrations in the Ringer. This suggests that increased external oxygen levels in the Ringer increase the ventricular oxygen availability, which is under air-saturated conditions (O_2-conc. $\sim 290\,\mu mol/l$ in the external Ringer solution and $\sim$ 0 O_2 in the ventricle) not sufficient to cover the complete oxygen need of the adjacent tissue, as shown in Fig. 4.5 b) and

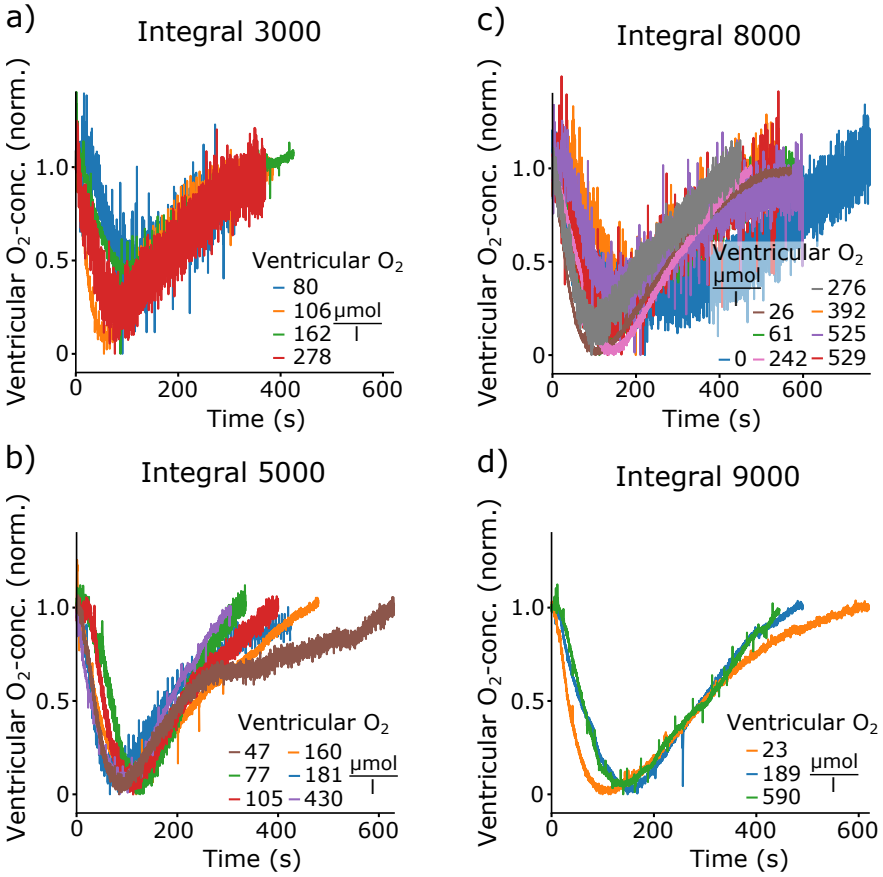

Figure 4.15.: Oxygen drops under different external oxygen levels – Normalized total O_2-consumption during a burst for total O_2 a) $3000\,\mathrm{s} \times \mu\mathrm{mol/l}$, b) $5000\,\mathrm{s} \times \mu\mathrm{mol/l}$, c) $8000\,\mathrm{s} \times \mu\mathrm{mol/l}$, and d) $9000\,\mathrm{s} \times \mu\mathrm{mol/l}$ for different ventricular O_2-concentrations.

Fig. 4.7. Since the external oxygen level does further affect discharge rates, cf. Fig. 4.17, it is important to understand how the discharge rates of a broad range of external oxygen levels correlates with the O_2-consumption in the IV$^{\mathrm{th}}$ ventricle. Fig. 4.18 shows two examples of the total O_2-consumption analysis, in a) and c), as well as the corresponding discharge rate, in b) and d). The two examples were taken with similar external Ringer levels: $910\,\mu\mathrm{mol/l}$ O_2. The total O_2-consumption in Fig. 4.18 c) is approximately 64 % the amount of the total O_2-consumption in Fig. 4.18 a) and Fig. 4.18 c) is 69 % of the discharge rate of Fig. 4.18 a), suggesting a correlation between the O_2-consumption and the discharge rate. A potential correlation between the magnitude of the spontaneous spike burst, associated O_2-consumption, and ventricular O_2-level was evaluated, following calculation of the total O_2-consumption [purple shaded areas in Fig. 4.18 a) and c)], and the overall discharge rate [grey shaded areas in Fig. 4.18 b and d)]. The discharge rate represents the total discharge over the entire burst duration; from now on this will be called total discharge rate. Fig. 4.19 shows the total discharge rate as a function of

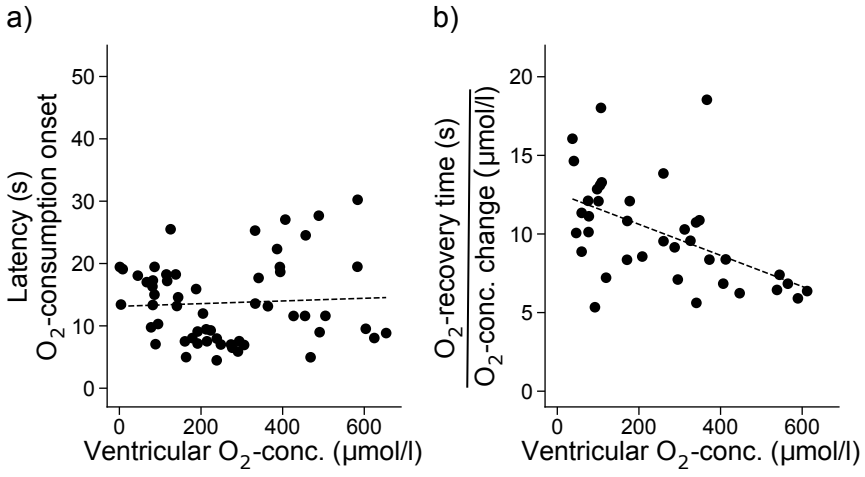

Figure 4.16.: Influence of external O_2-concentration on O_2-consumption onset and O_2-recovery – a) Correlation of the latency of the oxygen drop in the IV$^{\text{th}}$ ventricle at higher O_2-concentrations in the ventricle, $n = 59$ measurements from 7 preparations. Linear fit (dashed line): $m = 0.0015$, $R^2 = 0.0017$, $p = 0.76$. The mean of the latency was (13.7 ± 6.4) s. b) Time after a burst (lowest point of the oxygen drop) until the O_2-concentration in the ventricle reached the normal oxygen level, normalized to the oxygen change due to the drop, in correlation to the ventricular O_2-concentration (µmol/l). Linear fit (dashed line): $m = -0.01$, $R^2 = 0.2711$, $p = 0.0008$. $n = 59$ measurements from 7 preparations. Figures modified from Ref. [132].

the ventricular O_2-concentration (black), indicating that the extent of spontaneous spike bursts was independent of the ambient O_2-level, since the slope of the linear regression was not significantly different from zero ($p = 0.377$). In contrast, the integral of the O_2-transient increased with higher ventricular O_2-levels (purple) as indicated by the non-zero slope of the linear regression ($p = 0.022$), thus confirming the generation of larger O_2-transients when augmenting the bath O_2-level [compare O_2-transients in Fig. 4.12 d) and e), Fig. 4.14 a) and b)].

Fig. 4.20 shows a slightly higher magnitude of O_2-consumption when discharge rates were increased, clearly indicating an interrelation of the oxygen drop and the discharge rate during a burst. The fact that brain O_2-levels are not saturated below ~ 626 µmol/l O_2, cf. Fig. 4.7, and no O_2-consumption was visible below ~ 700 µmol/l, cf. Fig. 4.5 b), the external Ringer levels ranged from 500 µmol/l - 800 µmol/l O_2 (yellow) and 800 µmol/l - 1200 µmol/l O_2 (green) in Fig. 4.20. Fig. 4.20 a) shows a linear correlation between the increased discharge and the increased O_2-consumption in the ventricle. However, the integrals of the O_2-consumption was broadly scattered. To exclude the interference of discharge activity to O_2-consumption, in Fig. 4.20 b) the O_2-consumption from Fig. 4.20 a) was normalized to the corresponding discharge rate integral and is shown as function

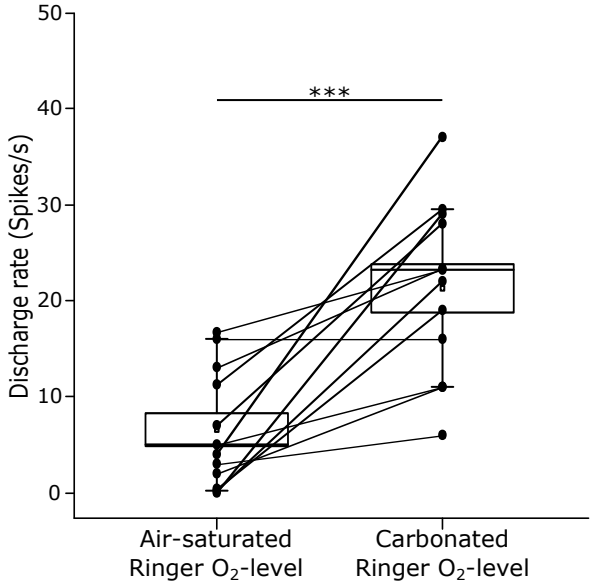

Figure 4.17.: Dependency of resting discharge rates on external oxygen levels – Discharge rates (Spikes/s) show a variance during changes of the external oxygen level between air-saturated [$(6.6 \pm 6.2)\,\mu\text{mol/l}$, 12 animals] and carbonated Ringer [$(21.3 \pm 9.1)\,\mu\text{mol/l}$, 12 animals]. Oxygen levels in the Ringer were adjusted to air-saturated levels of $(276.8 \pm 9.4)\,\mu\text{mol/l}$, corresponding to a ventricular O_2-concentration of $(0 \pm 15.5)\,\mu\text{mol/l}$. Carbonated Ringer O_2-concentration was increased to $(814.7 \pm 171.1)\,\mu\text{mol/l}$, corresponding to a ventricular O_2-concentration of $(183.1 \pm 156.5)\,\mu\text{mol/l}$. *** $p \leq 0.001$; Wilcoxon matched-pairs signed ranked test.

of the ventricular O_2-concentration. It can be seen that the O_2-consumption is generally increased at higher discharge rates [Fig. 4.20 a)], but also when normalized to the discharge rates the O_2-consumption is also increased at higher oxygen levels [Fig. 4.20 b)].

As just established, the total O_2-consumption is dependent on the total discharge rate. Therefore, it is important to understand how the O_2-consumption is correlated to the burst duration. This is shown in Fig. 4.21, where a longer burst duration is accompanied by a higher O_2-consumption. The O_2-consumption per burst/second is $0.4\,\mu\text{mol/l/s}$ [Fig. 4.21 b)], which is independent of the external Ringer O_2-concentrations [Fig. 4.21 c)]. The total O_2-consumption ranges from $\sim 10\,\mu\text{mol/l}$ (min) to $\sim 50\,\mu\text{mol/l}$ (max), depending on the burst duration, for measurements above $570\,\mu\text{mol/l}$ external Ringer solution, cf. Fig. 4.21 a).

A major problem in many experimental preparations is that the oxygen supply is limited through diffusion processes. In our semi-intact *in vitro* preparation the tissue lacks an active blood circulation, and therefore natural oxygen supply through the vasculature. Variations of the external oxygen supply with the Ringer flow is possible in our setup, but comes along with some drawbacks as the oxygen delivery is not quick and precise, since

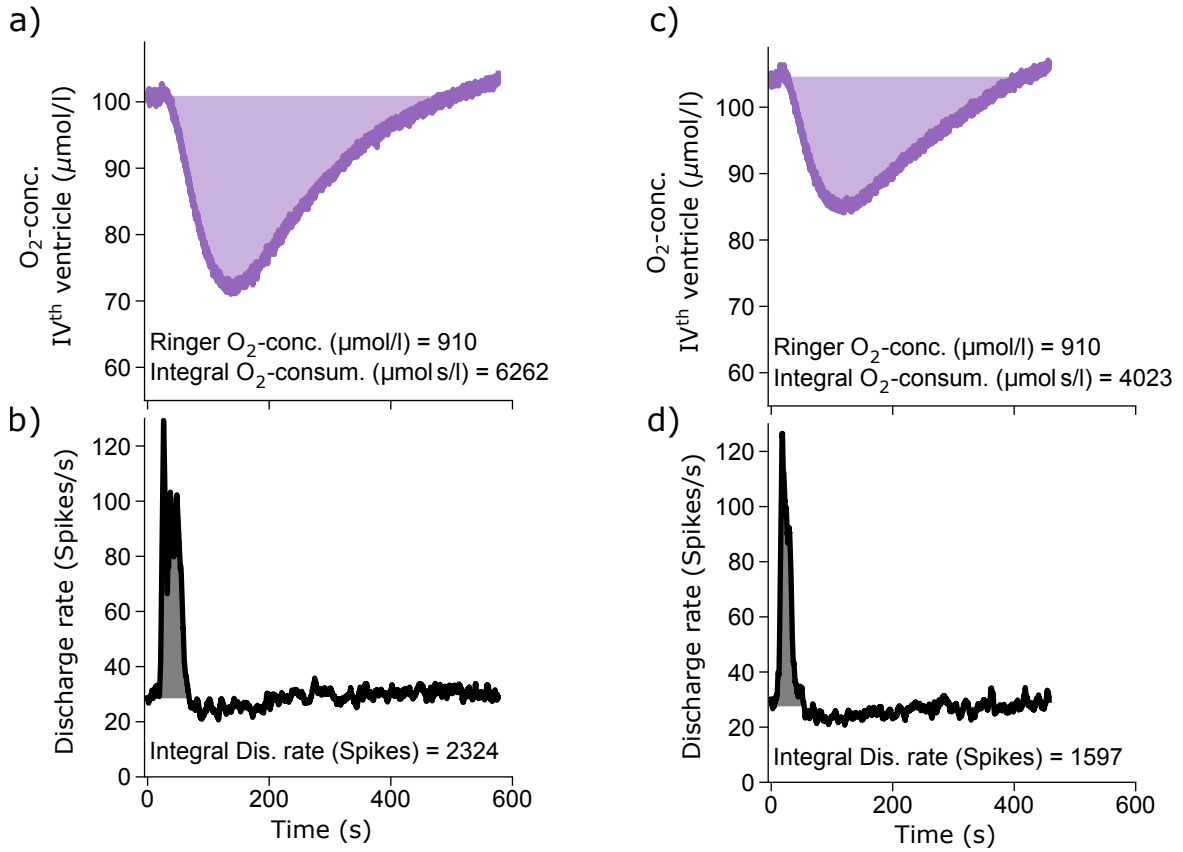

Figure 4.18.: Total O_2-consumption and discharge rate – Two examples of total O_2-consumption calculations for O_2-consumption in a) and c), and corresponding discharge rates in b) and d) during a spontaneous burst. External oxygen was in both examples $910\,\mu mol/l$ O_2. Figures modified from Ref. [132].

most oxygen diffuses from Ringer solution into the air. To guarantee fast and precise oxygen delivery to the brain, a new approach was established where oxygen producing organisms were inserted into the vascular system of the larvae prior to the preparation of the isolated tissue.

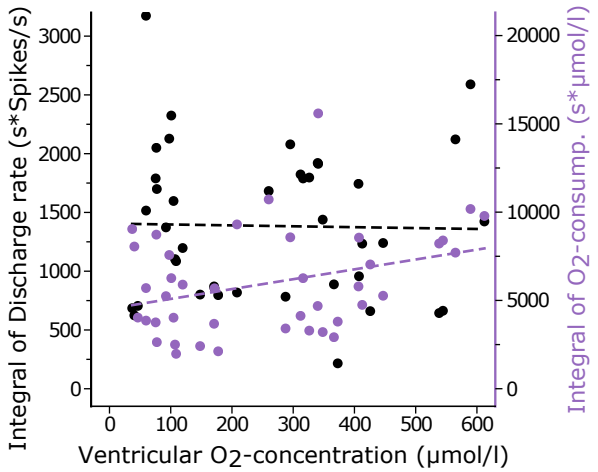

Figure 4.19.: Influence of ventricular oxygen levels on discharge rate and O_2-consumption – Integrals of spike rates (black) and of O_2-consumption (purple) as a function of oxygen levels in the ventricle. $n = 59$ measurements from 9 preparations. Linear fit (dashed line, black): $m = 0.45$, $R^2 = 0.0137$, $p = 0.377$. Linear fit (dashed line, purple): $m = 6.80$, $R^2 = 0.088$, $p = 0.022$. Figure modified from Ref. [132].

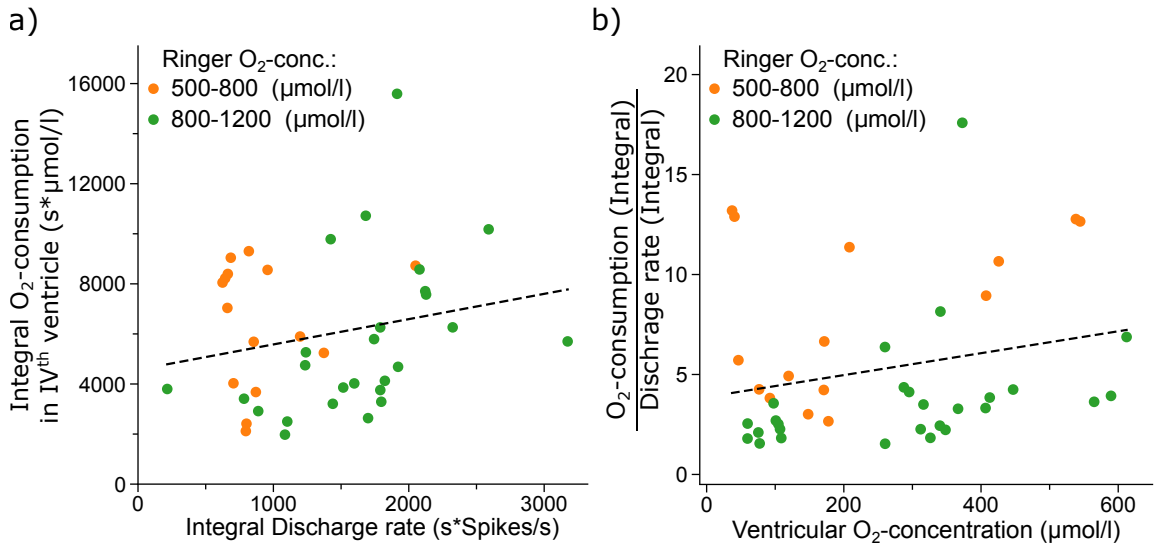

Figure 4.20.: Influence of external oxygen levels on discharge rate and O_2-consumption – a) Total O_2-consumption and total discharge rate vs different bursts, during several external bath oxygen levels, $n = 52$ measurements from 10 preparations. Linear fit (dashed line): $m = 1.01$, $R^2 = 0.048$, $p = 0.167$. b) Integral of O_2-consumption normalized to the corresponding integral of discharge rate, shown as correlation to the ventricular O_2-concentration. Linear fit (dashed line): $m = 0.01$, $R^2 = 0.044$, $p = 0.090$. Figure b) modified from Ref. [132].

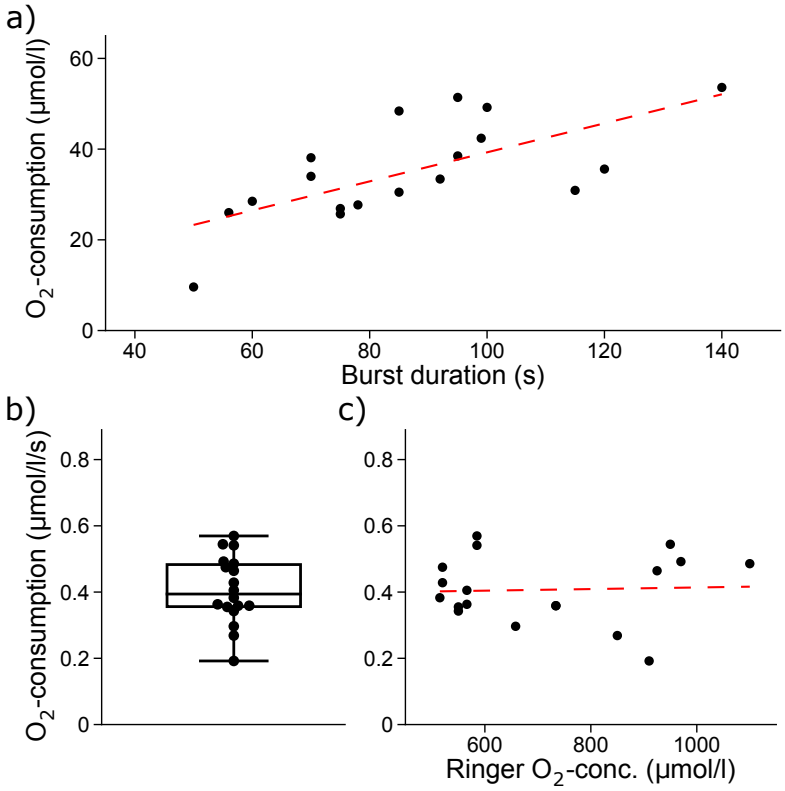

Figure 4.21.: O_2-consumption during bursting – Oxygen drops from Fig. 4.15 were analyzed with respect to peak amplitude (before normalization), to obtain a) the maximum O_2-consumption in relation to burst duration. Linear fit (dashed line): $m = 0.32$, $R^2 = 0.45$, $p = 0.0023$. b) O_2-consumption normalized to burst duration yields a mean of $(0.4 \pm 0.1)\,\mu\mathrm{mol/l/s}$, which is independent from the external Ringer O_2-concentration shown in c). Linear fit (dashed line): $m = 0.00002$, $R^2 = 0.002$, $p = 0.86$.

4.3. Algae and Cyanobacteria as Oxygen Source in the *Xenopus laevis* Brain

In the following, the injection and distribution of algae and cyanobacteria as oxygen source into the brain of *Xenopus laevis* will be described. Sec. 4.3.1 characterizes the concentration and light dependency of O_2-production of the isolated algae *C.reinhardtii* and isolated cyanobacteria *Synechocystis*. These single-celled organisms were introduced into the vascular system of *Xenopus laevis* larvae and their distribution in the brain vasculature of the larvae will be then visualized in Sec. 4.3.2. In Sec. 4.3.3, the algal O_2-production sufficiency to rescue neuronal discharge under hypoxia is described. Algae and cyanobacteria were grown in collaboration with the Nickelsen lab by Dr. M. Chávez and Prof. Dr. J. Nickelsen.

4.3.1. O_2-Production in Isolated Algae and Cyanobacteria

To determine the optimal parameters for the oxygen production in the brain of *Xenopus laevis*, it was crucial to evaluate the O_2-production of *C.reinhardtii* and *Synechocystis* as a function of cell concentration and luminance. This is shown in Fig. 4.22. Cell concentrations of 0.1×10^9 cells/ml and 0.5×10^9 cells/ml, and luminance levels of 5400 lux [Fig. 4.22 a)] and 30 500 lux [Fig. 4.22 b)] (these luminance levels were determined to be the optimal parameters, see Sec. 3.2.4). The maximal O_2-production (µmol/l) refers to the highest concentration for both, algae or cyanobacteria, under light illumination. As controls, photomutant strains of algae and cyanobacteria, respectively, were used with a concentration of 0.1×10^9 cells/ml and a luminance of 5400 lux, cf. Sec. 3.2.1 and Sec. 3.2.2. Photomutant algae and cyanobacteria were not capable of producing oxygen, since these strains were missing a gene to encode PS II. Further, algae and cyanobacteria need oxygen from their environment for their own metabolic needs, which can be seen in Tab. 4.1, where the O_2-concentration of the mutants were found to be negative. The highest O_2-concentration produced by algae or cyanobacteria upon illumination was usually acquired within 1.5 hours, after which a plateau was reached. Cell concentrations of 0.5×10^9 cells/ml reached significantly higher oxygen levels in *Synechocystis* at 30 500 lux, in comparison to lower cell concentrations. For *C.reinhardtii*, no significant difference in O_2-production was observed for lower and higher cell numbers for both luminance intensities. However, a higher light intensity of 30 500 lux, cf. Fig. 4.22 b), caused an increased O_2-production in *C.reinhardtii* for both concentrations, and in *Synechocystis* only for the higher concentration. High luminance is known to have a phototoxic effects, however, this was not observed up to 30 500 lux. Besides not being phototoxic, also higher O_2-production

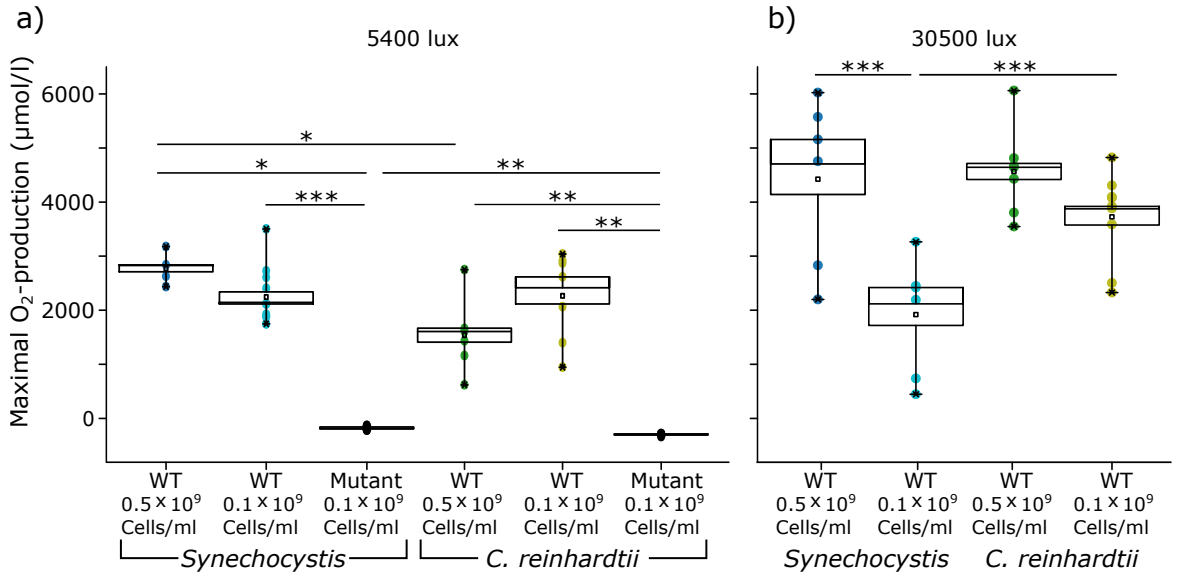

Figure 4.22.: Maximal O_2-production (µmol/l) of *Synechocystis* and *C.reinhardtii* – Different cell concentrations (0.5×10^9 cells/ml and 0.1×10^9 cells/ml) and luminance a) 5400 lux and b) 30 500 lux were tested. As a control, photomutant strains with 0.1×10^9 cells/ml of both *Synechocystis* and *C.reinhardtii* were monitored with 5400 lux. * $p \leq 0.05$, ** $p \leq 0.01$, *** $p \leq 0.001$, Mann-Whitney U-test. Mean values, and statistical analysis are listed in Tab. 4.1.

rates were reached compared to 5400 lux. Both algae and cyanobacteria appear to have an extensive O_2-production capacity. While at 5400 lux *Synechocystis* with a cell concentration of 0.5×10^9 cells/ml provides the highest output, for 30 500 lux *Synechocystis* and *C.reinhardtii* with a cell concentration of 0.5×10^9 cells/ml are both providing the highest oxygen output. Statistical mean values for the maximal O_2-production rates at all conditions are listed in Tab. 4.1.

Since the oxygen maximum of the microorganisms is not reached within the same time frame, the data from Fig. 4.22 were further analyzed to evaluate which species produces not only the most oxygen, but also on which time-scale. The EC_{50}, which is the time until the half maximum value is reached, was calculated and plotted in Fig. 4.23. It clearly shows that *C.reinhardtii* has lower EC_{50} values for the O_2-production at 5400 lux, as seen in Fig. 4.23 a), indicating that *C.reinhardtii* reaches the maximum of O_2-concentration faster than *Synechocystis* and is therefore more efficient in its O_2-production. As can be seen in Fig. 4.23 b), increasing light intensity to 30 500 lux, the EC_{50} values decreased for both species, even more drastically for *Synechocystis* [Fig. 4.23 a)]. Statistical mean values for the EC_{50} of maximal O_2-production of all conditions are listed in Tab. 4.2.

The measurements with isolated microorganisms show that *C.reinhardtii* is significantly faster then *Synechocystis* in O_2-production for both cell concentrations (0.1×10^9 cells/ml and 0.5×10^9 cells/ml), as shown in Fig. 4.23. However, *C.reinhardtii* also has a signifi-

Table 4.1.: Algae and Cyanobacteria O_2-production maximum. Cell concentrations of 0.1×10^9 cells/ml and 0.5×10^9 cells/ml were monitored for wild type (WT) and photomutants. The O_2-concentration and the respective SEM is given with the number of animals (n) for both light intensities 5400 lux and 30 500 lux.

		Light intensity (lux)					
		5400			30500		
	Cell conc. (cells/ml)	O_2-conc. (µmol/l)	SEM(±)	n	O_2-conc. (µmol/l)	SEM(±)	n
Synechocystis WT	0.5×10^9	2770	317	4	4469	1565	6
	0.1×10^9	2244	534	11	1939	1105	5
Mutant	0.1×10^9	−171	42	5	-	-	-
C.reinhardtii WT	0.5×10^9	1542	703	6	4613	819	8
	0.1×10^9	2266	819	7	3764	825	9
Mutant	0.1×10^9	−334	21	5	-	-	-

Table 4.2.: Algae and Cyanobacteria EC_{50} (time until the half maximum O_2-production is reached). Cell concentrations of 0.1×10^9 cells/ml and 0.5×10^9 cells/ml were monitored for wild type (WT). The EC_{50} and the respective SEM is given with the number of animals (n) for both light intensities 5400 lux and 30 500 lux.

		Light intensity (lux)					
		5400			30500		
	Cell conc. (cells/ml)	EC_{50} (s)	SEM(±)	n	EC_{50} (s)	SEM(±)	n
Synechocystis WT	0.5×10^9	3374	794	4	1468	320	6
	0.1×10^9	2834	382	5	1679	186	5
C.reinhardtii WT	0.5×10^9	1407	382	6	1291	351	8
	0.1×10^9	1930	558	7	939	161	9

cantly lower maximal O_2-output for 0.5×10^9 cells/ml at 5400 lux, cf. Fig. 4.22 a). Both, algae and cyanobacteria, were used for injections into the vasculature of *Xenopus laevis* larvae. Due to a possible phototoxic effect, which could occur in lower concentrated algae or cyanobacteria solutions, as it is the case during injection and distribution throughout the vascular system, light illuminance was set to 5400 lux.

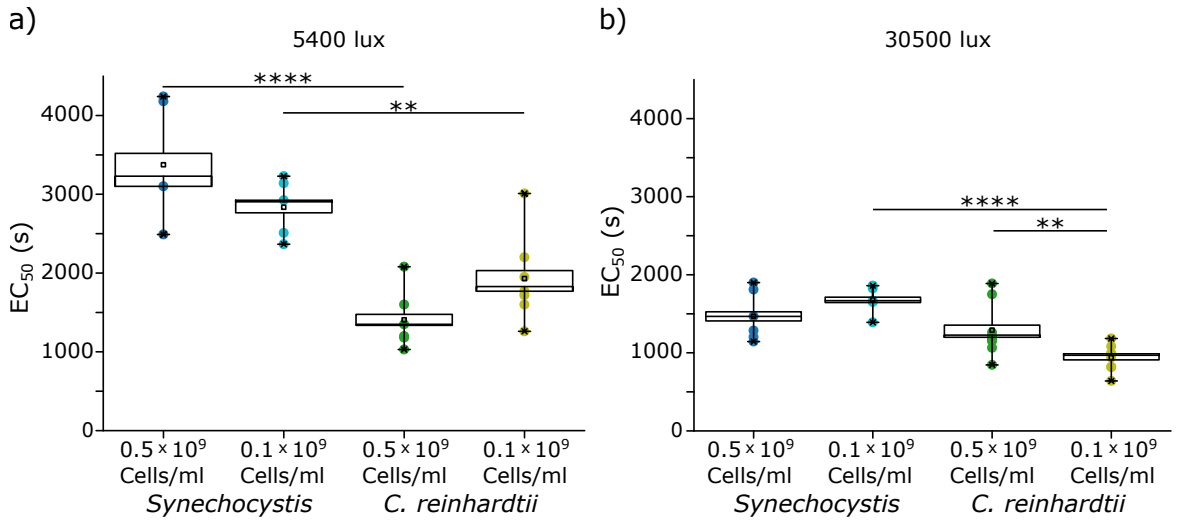

Figure 4.23.: Time until half maximum of O_2-production is reached – EC_{50} values for *Synechocystis* and *C.reinhardtii* at 5400 lux and 30 500 lux at different cell concentrations (0.1×10^9 cells/ml and 0.5×10^9 cells/ml). ** $p \leq 0.01$, **** $p \leq 0.0001$, Mann-Whitney U-test. EC_{50} values, and statistical analysis are listed in Tab. 4.2.

4.3.2. Visualization of Microorganisms in the Brain of *Xenopus laevis*

After injection of algae and cyanobacteria into the vasculature of the larvae, as described in Sec. 3.3, the distribution of the microorganisms throughout the entire brain vasculature was visualized. Fig. 4.24 shows the brain from dorsal, with Mesencephalon (MP) and Cerebellum (CB). The choroid plexus, above the Rhombencephalon (RB), is filled with algae or cyanobacteria, as seen by the green color. The IV$^{\text{th}}$ ventricle is located below the choroid plexus and is marked by the black box (v). The microorganisms also fill the blood vessels inside the brain, and are visible through the tissue. To distinguish between microorganisms and brain vasculature, the blood vessel walls, which contain oligosaccharides, were stained with Isolectin, coupled to Alexa Fluor 488. Isolectin was injected together with algae or cyanobacteria solution (details can be found in Sec. 3.3. The chlorophyll in the microorganisms can be excited with light at a wavelength of 640 nm/655 nm (depicted in green), and the Isolectin with 488 nm/493 nm (depicted in red). Fig. 4.25 shows the fixed brain from dorsal. A z-stack through the entire tissue is shown in Fig. 4.25 a). A single plane is shown in Fig. 4.25 b). The single plane with the excited chlorophyll autofluorescence is shown in Fig. 4.25 c), and the excitation of the blood vessels is shown in Fig. 4.25 d). The image revealed a fine network of blood vessels in the hindbrain adjacent to the IV$^{\text{th}}$ ventricle, in comparison to noticeably much thicker blood vessels in the forebrain.

The strong chlorophyll-autofluorescence makes it difficult to see a co-localization between algae or cyanobacteria and isolectin-stained blood vessels. Therefore, the tissue

was imaged at a higher magnification, which is shown in Fig. 4.26. The image shows the region of the vestibular nuclei, adjacent to the IVth ventricle, cf. the white box in Fig. 4.25 b). The microorganisms (chlorophyll excitation, depicted in green) are evenly distributed throughout the blood vessels (Isolectin A 488, depicted in red). The distribution is only shown in one plane, as the image represents a single focal plane. There was no clumping or blockage, showing that algae or cyanobacteria fit into the brain vasculature and were evenly distributed after the injection. This is observed despite the different sizes of the two microorganisms: *Synechocystis* with a diameter of 2 µm [Fig. 4.26 a)] and *C.reinhardtii* with a diameter 10 µm [Fig. 4.26 b)]. In addition, the shape of the microorganisms appeared to not be altered, suggesting that algae and cyanobacteria remained intact and alive within the blood vessels.

Furthermore, in Fig. 4.27 magnified single blood vessels are shown. Fig. 4.27 a) shows blood vessels with injected *Synechocystis*. The lines (green and red) represent electronically constructed coronal sections through the two vessels shown in Fig. 4.27 b) and c). These coronal sections through the blood vessels more clearly illustrate the localization of the microorganisms inside the blood vessels. Blood vessels with *C.reinhardtii* are shown in Fig. 4.27 d) - f). In comparison with *Synechocystis*, the algae *C.reinhardtii* are of similar size as the vasculature diameter and lined up one after the other inside the blood vessels. For the smaller *Synechocystis*, two to three single cells fit into the blood vessel (diameter) and could possibly distribute throughout smaller vessels, deeper in the tissue.

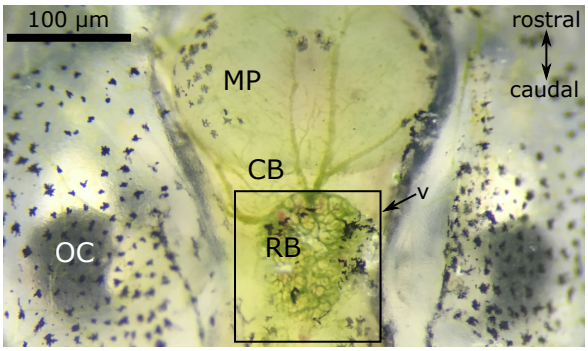

Figure 4.24.: Distribution of microorganisms in the blood vessels of the brain (the picture shows injected *C.reinhardtii*) – Image of an intact brain in the preparation. Mesencephalon (MP), Cerebellum (CB), Rhombencephalon (RB), and Otic capsule (OC) can be seen. The choroid plexus is located on top of the IVth ventricle and is filled with *C.reinhardtii* (green). Region of the IVth ventricle (black box, marked with v). Image taken with Leica MZ12.

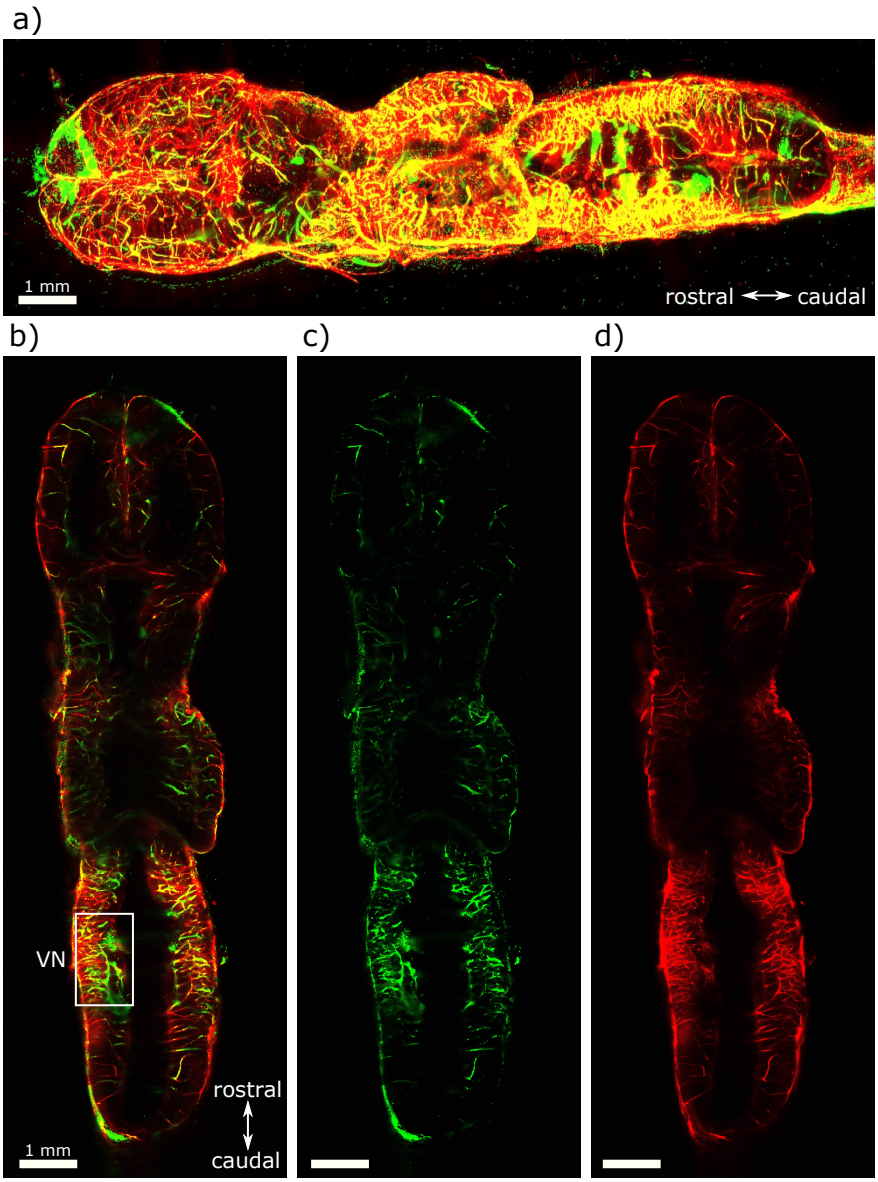

Figure 4.25.: Distribution of microorganisms (the picture shows injected *Synechocystis*) throughout the entire brain – Confocal image of a fixed brain showing a z-stack in a) and a single focal plane in b). The region of the vestibular nuclei is marked by the white box VN. c) Algae/ cyanobacteria autofluorescence (depicted green). d) Blood vessels were stained with Isolectin Alexa Fluor $488\,\mathrm{nm}$ conjugate (depicted in red). Taken by Zeiss LSM 900-Airyscan-2, 10x.

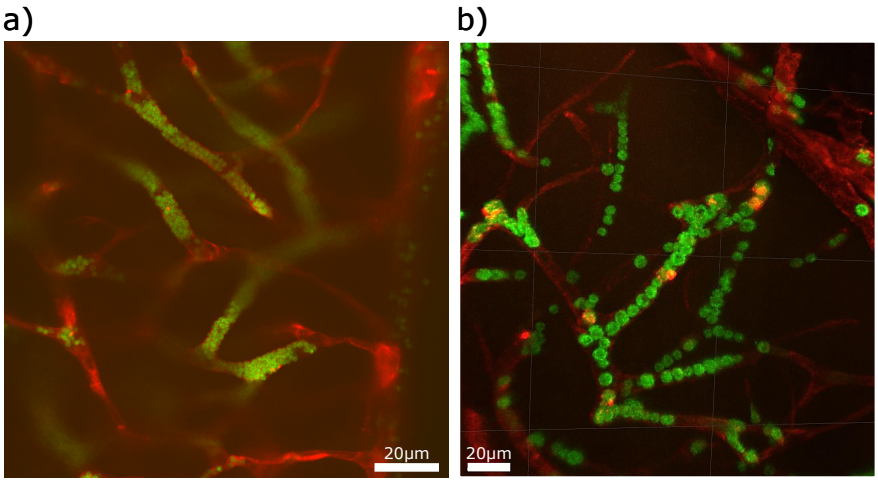

Figure 4.26.: Confocal images of fixed brain tissue at the level of the vestibular nuclei – a) *Synechocystis*, imaged with Zeiss LSM 900-Airyscan-2, 20x. Chlorophyll excitation (depicted in green) and Isolectin (depicted in red). b) *C.reinhardtii*, imaged with a VivaScope RS-G4 microscope (Mavig GmbH) and a 60x Objective, zoom 1.35 (Olympus). Chlorophyll excitation (depicted in green) and Isolectin (depicted in red). Picture a) taken by Zeiss. Picture b) taken by Mavig GmbH.

4.3.3. Photosynthetic O_2-Production in the Brain of *Xenopus laevis*

For experiments in the intact larval brain, suspensions of *C.reinhardtii* or *Synechocystis* were injected into the heart of anesthetized larvae and were allowed to spread through the vascular system, reaching brain through the respective blood vessels. For the injection, cell concentrations with 10×10^9 cells/ml were used, cf. Sec. 3.3. After dissection of the *in vitro* preparation, oxygen monitoring in the IV$^{\text{th}}$ ventricle occurred as described in the previous chapter. With illuminance, photosynthetic oxygen is directly produced from the algae or cyanobacteria in the vicinity of the high energy—and therefore also high oxygen demanding—neuronal cells. The illumination let the O_2-concentration in the ventricle increase, as depicted in the example recording in Fig. 4.28. The duration from the start of the illumination (yellow box) and the point where the oxygen level started to increase is called latency. The time until the O_2-production reached its maximum is called rise time and the duration from illumination stop until the ventricular O_2-level decreased to control values is called decay time. Small drops in the oxygen rise (blue trace) are due to spontaneously appearing bursts, which can be seen as more frequent and higher amplitude nerve discharges, cf. black trace in Fig. 4.28. To quantify the quality of O_2-production of the microorganisms in an intact nervous system, the time of latency, rise time, and decay time was analyzed, as shown in Fig. 4.29. The latency of oxygen increases by both microorganisms was independent from external Ringer O_2-concentration and

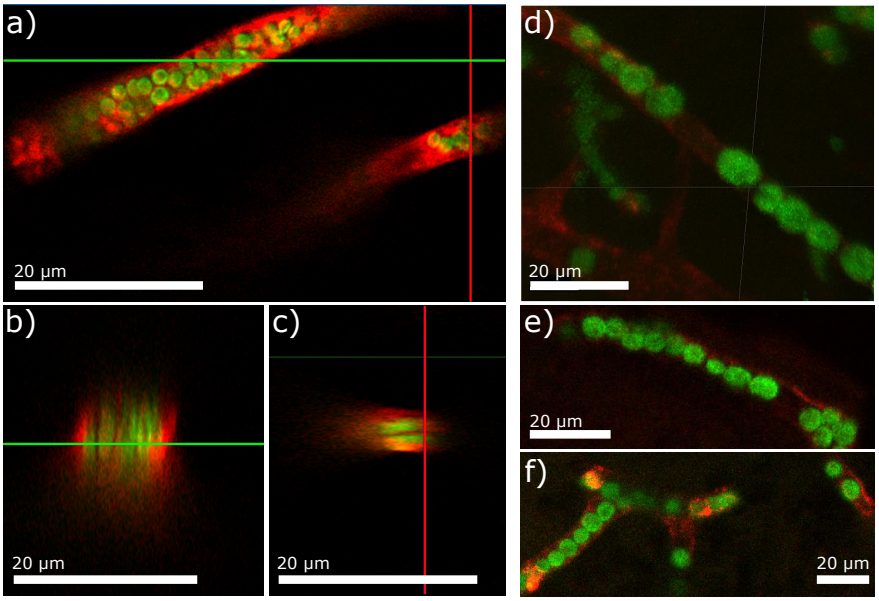

Figure 4.27.: Single blood vessels and coronal section – Confocal images depicting blood vessels stained with Isolectin-A488 (staining for blood vessel walls, depicted in red) and microorganisms (chlorophyll autofluorescence, depicted in green). a) Two blood vessels with injected *Synechocystis* were imaged and electronically cut along b) the horizontal green line, and c) the vertical red line. d) - f) Blood vessels with *C.reinhardtii*. Pictures a) - c) taken by Zeiss, with LSM 900-Airyscan-2, 40x. Pictures d) - f) imaged with a RS-G4 Mavig Vivascope, 60x by Mavig GmbH.

occured within about 2 min. The latency was also significantly shorter with *Synechocystis*, as can be seen in Fig. 4.29 a). Also the rise time in Fig. 4.29 b) showed a slightly faster augmentation when *Synechocystis* was preset and occured within about 10 min. The decay time was about 5 min for both cyanobacteria and algae, as shown in Fig. 4.29 c).

No significant difference was observed for air-saturated or carbonated Ringer solutions for a particular species with respect to latency, rise time, and decay time, respectively. However, the rise time and decay time are both dependent on the amount of O_2-production. To analyze the O_2-production of both microorganisms, the ventricular O_2-concentration of the preparation was monitored during light illumination. In Fig. 4.30 a) the O_2-concentration (µmol/l) at the ventricular floor in darkness, during illumination at 5400 lux, and in the surrounding Ringer solution were plotted. The oxygen measurements in the ventricle (dark + light) were performed with *C.reinhardtii* and *Synechocystis*, respectively. From the experiments described above, the ventricular oxygen is known to be close to zero in air-saturated Ringer ($\sim$290 µmol/l) conditions, cf. Sec. 4.1. External bath levels were increased (hyperoxia: $\sim$800 µmol/l), thus elevating the ventricular oxygen level. In order to estimate the amount of oxygen, potentially produced by the algae, it

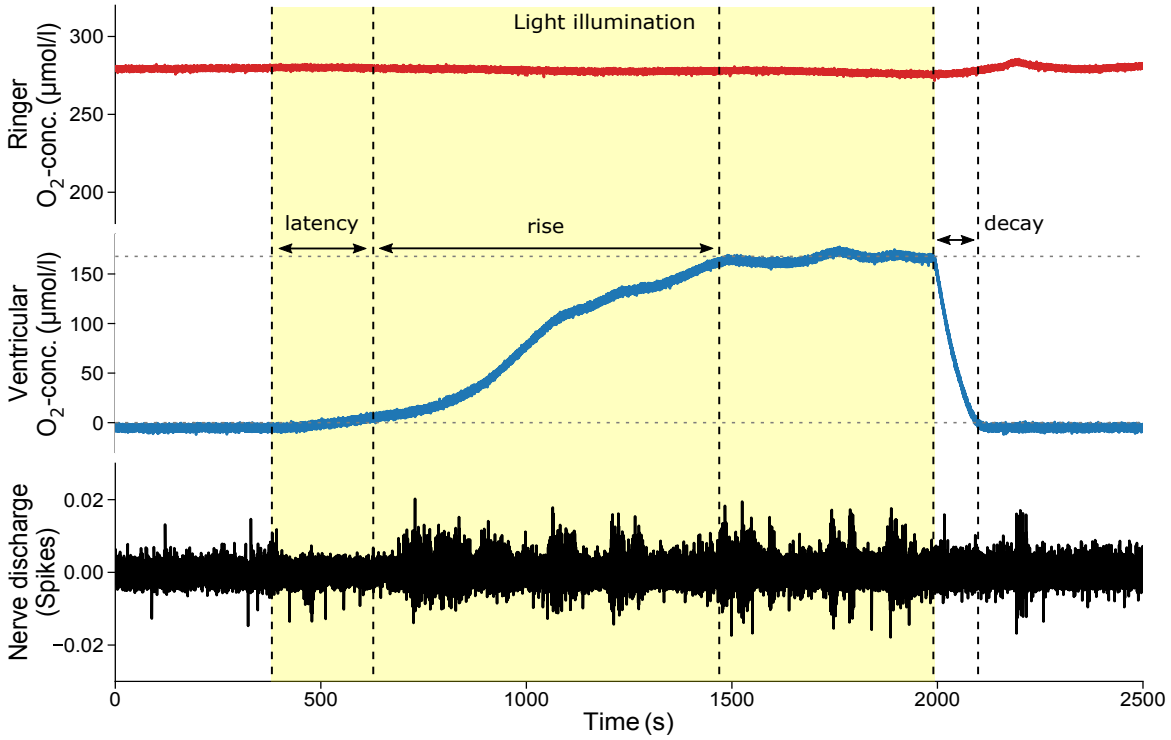

Figure 4.28.: Light induced O_2-production in a larval preparation – Example recording of Ringer (red), ventricular O_2 (µmol/l, blue), and nerve firing rates (black), at air-saturated bath O_2-concentrations (µmol/l) in a semi-intact *in vitro* preparation of *Xenopus laevis* larvae, in which microorganisms (here *C. reinhardtii*) were injected and spread throughout the vascular system. With light illumination (5400 lux, yellow box) the O_2-level in the ventricle increased, and decreased after illumination stopped, while the external Ringer O_2-concentration remained constant.

was necessary to saturate the O_2-consumption of the brain. This then allowed to measure photosynthetically produced oxygen as increase of the ventricular O_2-concentration during illumination, without the masking by the O_2-consumption of the brain. The difference between the oxygen measured in the ventricle in darkness and during illumination was on average ~ 170 µmol/l and related to algal O_2-production. To quantify the O_2-production of *C.reinhardtii* and *Synechocystis*, O_2-production of both species was separated and plotted as a function of external Ringer levels in Fig. 4.30 b). However, no difference was encountered and both species produced around 200 µmol/l. Further, photomutant strains of both algae *C.reinhardtii* and cyanobacteria *Synechocystis*, which lack a functional photosystem II and thus cannot produce oxygen, were used, cf. Fig. 4.31. Oxygen production between the two species was not significantly different to each other but was, as expected, considerably higher with regard to their respective photomutants. Fig. 4.31 shows that the photomutant of *Synechocystis* produces only small amounts of oxygen during light

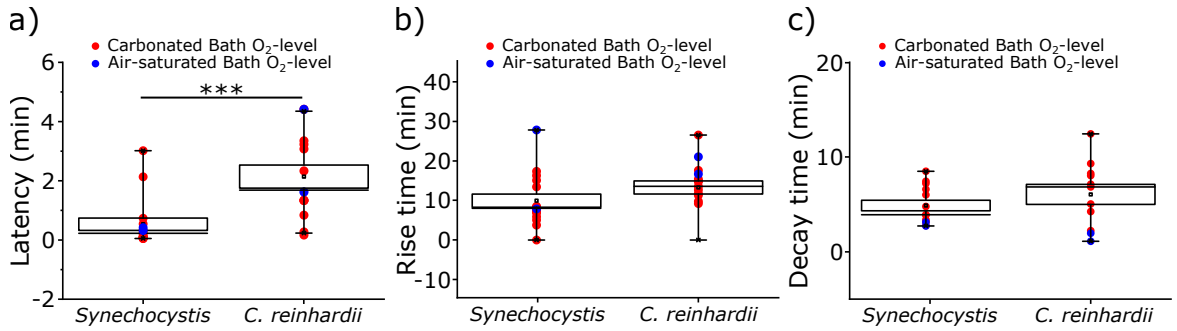

Figure 4.29.: Latency, rise time, and decay time of O_2-production of algae and cyanobacteria in *Xenopus laevis* preparations with different external O_2-concentrations – a) Latency (min) was measured in the IV$^{\mathrm{th}}$ ventricle beginning from light illuminance until the O_2-concentration in the ventricle began to rise [$(0.5 \pm 0.8)\,\mathrm{min}$ with n$=16$ for *Synechocystis* and $(2.1 \pm 1.4)\,\mathrm{min}$ with n$=13$ for *C.reinhardtii*]. b) Rise time (min) indicates the time from onset of O_2-production until the maximum level is reached [$(10.0 \pm 6.7)\,\mathrm{min}$ with n$=16$ for *Synechocystis* and $(13.3 \pm 6.4)\,\mathrm{min}$ with n$=13$ for *C.reinhardtii*]. c) Decay time (min) was determined from the illumination switch off until the O_2-concentration reached again the O_2-concentration at pre-light illumination [$(4.9 \pm 2.0)\,\mathrm{min}$ with n$=13$ for *Synechocystis* and $(6.1 \pm 3.5)\,\mathrm{min}$ with n$=11$ for *C.reinhardtii*]. Red and blue dots represents the O_2-concentration in the Ringer, with blue indicating air-concentration [$(264.6 \pm 29.4)\,\mu\mathrm{mol/l}$] and red indicating elevated Ringer concentrations [$(791.1 \pm 146.2)\,\mu\mathrm{mol/l}$]. *** $p \leq 0.001$, Mann-Whitney U-test.

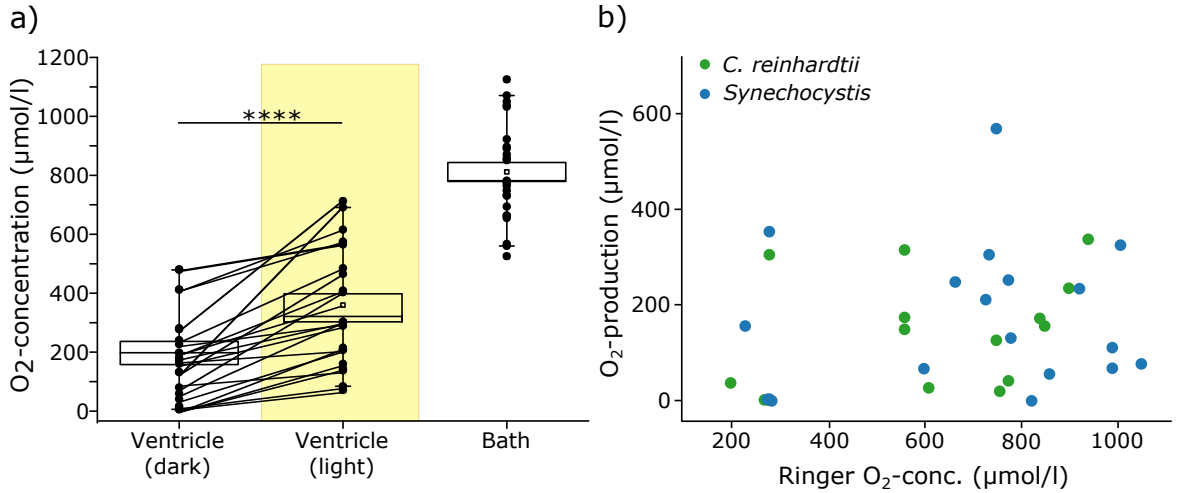

Figure 4.30.: O_2-production of algae and cyanobacteria in *Xenopus laevis* preparations – a) O_2-concentrations $(\mu\mathrm{mol/l})$ were measured in the IV$^{\mathrm{th}}$ ventricle in darkness [$(158.3 \pm 149.8)\,\mu\mathrm{mol/l}$, n$=25$] and under illumination (yellow box) with $5400\,\mathrm{lux}$ [$(332.0 \pm 193.7)\,\mu\mathrm{mol/l}$, n$=22$], at elevated oxygen levels in the external Ringer solution [$(819.8 \pm 165.4)\,\mu\mathrm{mol/l}$, n$=25$]. **** $p \leq 0.0001$; Wilcoxon matched-pairs signed rank test. b) Ventricular O_2-production capacity of *Synechocystis* (blue, $n = 19$) and *C. reinhardtii* (green, $n = 15$) as function of external Ringer O_2-concentration, ranging from $200\,\mu\mathrm{mol/l}$ to $1050\,\mu\mathrm{mol/l}$.

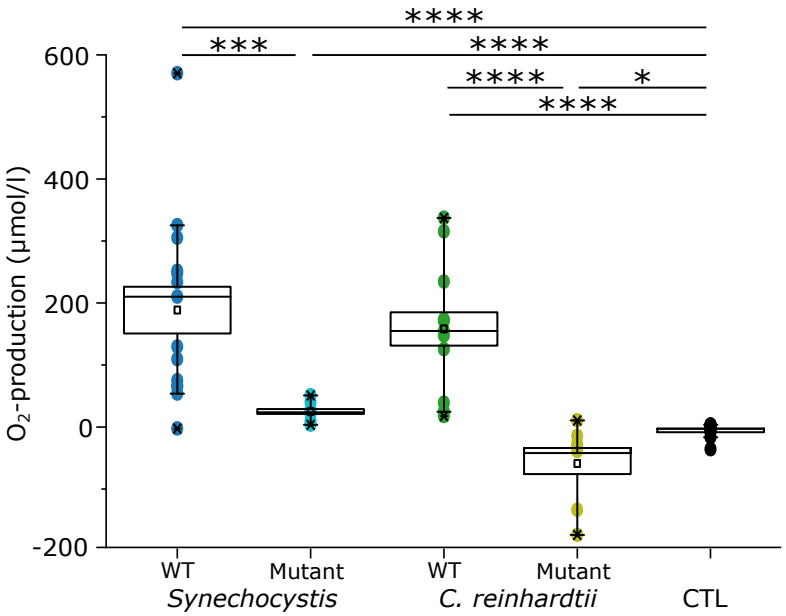

Figure 4.31.: Ventricular O_2-production of algae and cyanobacteria in the *Xenopus laevis* preparation upon illumination – *Synechocystis* wild type (WT) (blue, $(189.5 \pm 149.5)\,\mu mol/l$, $n = 14$), *C.reinhardtii* WT (green, $(159.4 \pm 106.8)\,\mu mol/l$, $n = 11$), their respective photomutants: *Synechocystis* (cyan, $(32.3 \pm 7.1)\,\mu mol/l$, $n = 8$) and *C.reinhardtii* (yellow, $(-55.9 \pm 67.3)\,\mu mol/l$, $n = 7$), and the control (CTL), larvae preparation without microorganisms injected (black, $(-3.1 \pm 10.9)\,\mu mol/l$). * $p \leq 0.1$, *** $p \leq 0.001$, **** $p \leq 0.0001$; Mann-Whitney U-test.

illumination. Observed were even negative values for O_2-production in *C.reinhardtii*, indicating that the net O_2-consumption is the consequence of respiration by the algae, as their mitochondria need to consume oxygen for energy production. This is not seen in *Synechocystis*, likely because these microorganism do not possess mitochondria. Upon illumination of the larval preparation, algae and cyanobacteria in the blood vessels of the brain produced 189.5 µmol/l (mean) and 159.4 µmol/l (mean) O_2 for *Synechocystis* and *C.reinhardtii*, respectively. Controls (CTL) were monitored without injected microorganisms and showed no O_2-production upon light illumination.

Next, the O_2-production of both algae and cyanobacteria in the *Xenopus* preparation under hypoxia ($\sim 40\,\mu mol/l$ O_2) was studied. Whether the photosynthetically produced oxygen from algae or cyanobacteria, distributed in the brain vasculature, were sufficient to maintain or even rescue the neuronal activity in *Xenopus* larvae under hypoxia were measured. Accordingly, the spike discharge of the trochlear motor nerve was recorded, as described in Sec. 4.2. External Ringer oxygen levels were reduced to $\sim 40\,\mu mol/l$ O_2 by ventilation of the Ringer solution with N_2 in a small chamber directly upstream the recording chamber (see Sec. 3.4). To control external bath oxygen levels, an oxygen sensor

was placed in the measurement chamber as described above, and also in the IVth ventricle to monitor the brain's O_2-consumption, cf. Fig. 4.10. The light induced neuronal recovery is shown in Fig. 4.32. When bath O_2-levels were decreased to $\sim 40\,\mu mol/l$, neuronal firing ceased after a short period. Because of the algal distribution in the vascular system, light illumination (5400 lux, yellow boxes) provoked the photosynthetic production of oxygen which rescued the nerve firing activity. This was repeatable within a given experiment by altering between light and dark periods. Nerve activity was absent in darkness, where photosynthesis was inactive and algae and cyanobacteria did not produce oxygen. During illumination, algae or cyanobacteria produced oxygen and released it into their surroundings, specifically into the blood vessels. From there, the oxygen diffused through the vascular walls into brain tissue, where it became metabolized for ATP production. That oxygen is crucial for maintained neuronal activity is seen during the dark periods, when all oxygen became depleted and nerve cell activity ceased after a few minutes. Bath oxygen levels remained constant at hypoxic levels, indicating that an external oxygen supply was absent. Furthermore, the ventricular O_2-concentrations remained largely unaltered, and maintained at a depleted level throughout the whole experiment, which suggests that the algal produced oxygen was immediately consumed within the brain. However, a slight increase after a few minutes of light illumination was generally observed, seen in the last illumination period shown in Fig. 4.32 (arrow). This increase was likely due to the delay of O_2-consumption of the tissue after algae or cyanobacteria had produced sufficient oxygen and it remained in the ventricle, where it was detected by the O_2-sensor.

The temporal parameters until neuronal discharge vanished following hypoxia are shown in Fig. 4.33 a). During low external oxygen levels ($\sim 40\,\mu mol/l\ O_2$), the nerve activity ceased, which is called the nerve cessation time. Following a decrease of the external oxygen in the bath Ringer, the trochlear nerve activity ceased after ~ 25 min and ~ 20 min in *Synechocystis* and *C.reinhardtii*, respectively, as can be seen Fig. 4.33 a). In the control experiments, non-injected larval preparations were used. Control measurements showed that neuronal activity can be maintained also for ~ 25 min. The temporal persistence was not significantly different between algae, cyanobacteria, and controls, indicating that microorganisms inside blood vessels do not interfere with nerve firing or the oxygen availability for nerve activity. In particular, in *C.reinhardtii*, where oxygen is consumed by their mitochondria, neuronal firing is not affected. The sufficiency of photosynthetic oxygen for restoring energy equivalents, required for neuronal maintenance, is analyzed in Fig. 4.33 b). With light activation of 5400 lux, algae and cyanobacteria produced oxygen that recovered the neuronal discharge, called restart time, within 14 min and 22 min for *Synechocystis* and *C.reinhardtii*, respectively. Light was switched on when the discharge ceased for ~ 5 min during hypoxia. In control conditions, where no microorganisms were

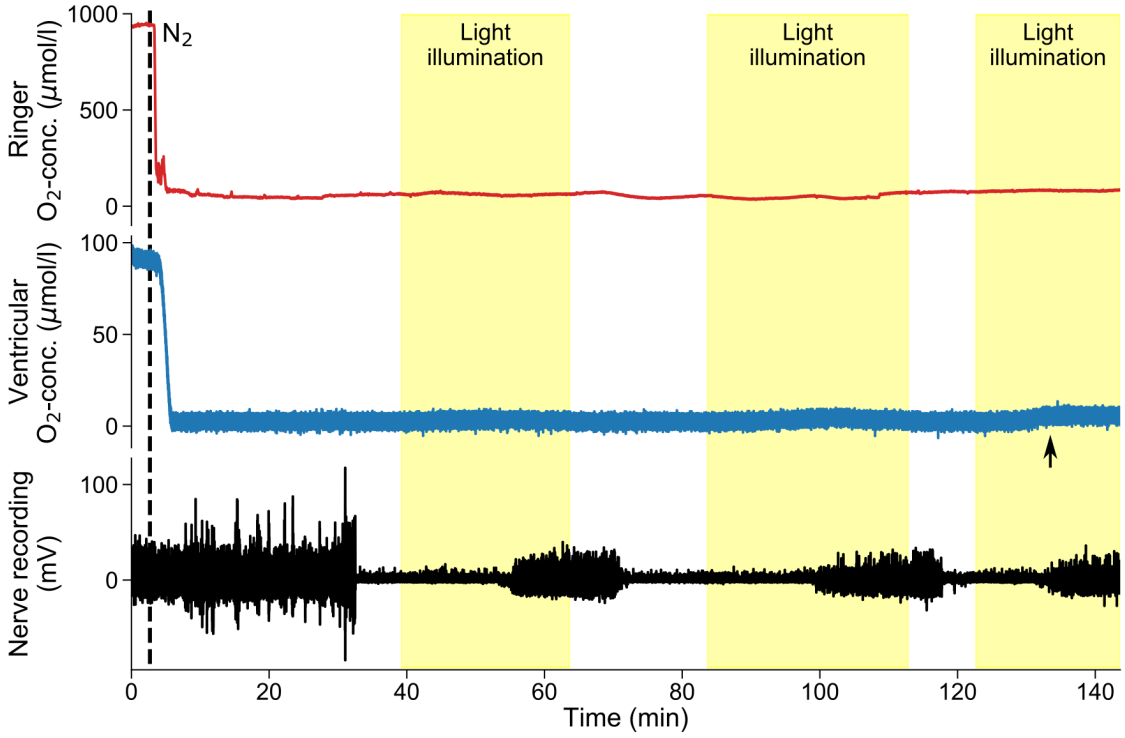

Figure 4.32.: Light induced neuronal recovery – Example recording of Ringer oxygen (red), ventricular O_2 (µmol/l, blue), and nerve firing rates (black), at decreased bath O_2-concentrations (µmol/l) in a semi-intact *in vitro* preparation of *Xenopus laevis* larvae, in which microorganisms were injected and spread throughout the vascular system. Nerve activity ceased at low O_2-levels, but could be rescued with light illumination (5400 lux, yellow boxes). This was repeated by alternating between light and dark periods. Black arrow indicates a slight increase of ventricular O_2-concentration due to fast photosynthetic O_2-production upon illumination and a diffusion delayed brain O_2-consumption.

injected, a recovery through external oxygen by aeration ($\sim$950 µmol/l O_2), required 35 min. Thus, the neuronal restart in controls took considerably longer than following light activation with either algae or cyanobacteria. Further, the recovery time of isolated larval preparations with injected *Synechocystis* was significantly faster compared to controls, where oxygen was supplied only through aeration of the Ringer solution.

As seen in Fig. 4.32, the rescued nerve activity seemed to be smaller than the nerve activity before the nitrogen treatment. To quantify the efficiency of photosynthetic oxygen to rescue the discharge rate, in Fig. 4.34 discharge rates were plotted for air-saturated (before the treatment, black), under hypoxia (N_2, black), and rescued discharge rates with carbogen (red), or light activation (yellow box). Oxygen production through both algae and cyanobacteria achieved similar discharge rates of the *Xenopus laevis* as compared to

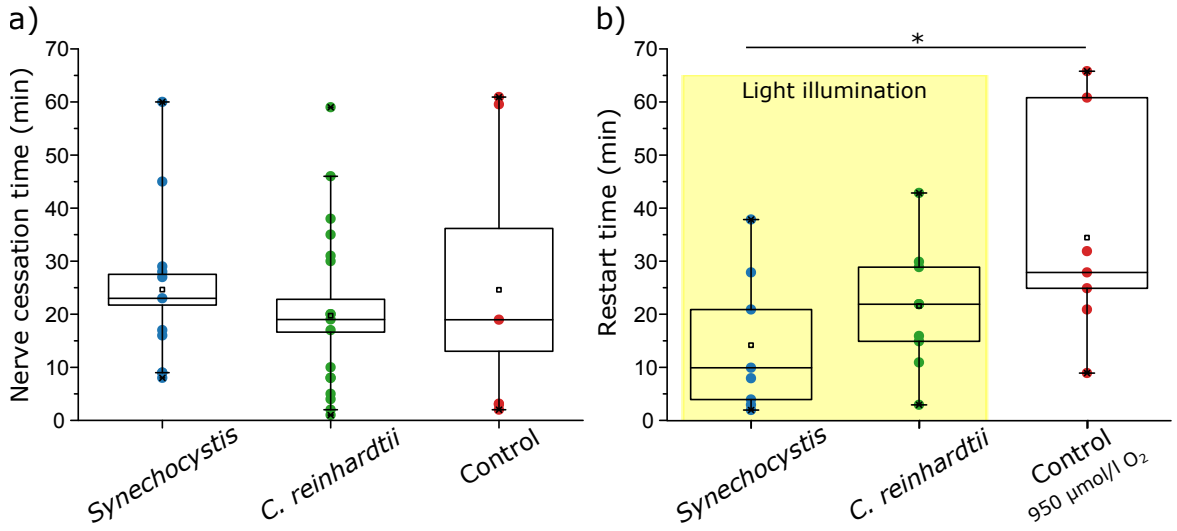

Figure 4.33.: Cessation and restart time of neuronal discharge under hypoxia with photosynthetic oxygen – Time (min) until neuronal activity ceased is called nerve cessation time, and time (min) until neuronal activity recovered is called restart time. a) Nerve cessation time of *Synechocystis* (blue, mean: $(24.6 \pm 16.1)\,\mathrm{min}$, $N = 10$ animals, $n = 11$ measurements) and *C.reinhardtii* (green, mean: $(19.7 \pm 16.9)\,\mathrm{min}$, $N = 13$ animals, $n = 18$ measurements), in comparison to the control (red, mean: $(24.6 \pm 28.3)\,\mathrm{min}$, $N = 6$ animals, $n = 6$ measurements). b) Time (min) until neuronal discharge is recovered under hypoxia ($\sim 40\,\mu\mathrm{mol/l}$), with light activation ($5400\,\mathrm{lux}$) for *Synechocystis* (blue, $(14.3 \pm 13.3)\,\mathrm{min}$, $N = 6$ animals, $n = 8$ measurements), *C.reinhardtii* (green, $(21.7 \pm 11.9)\,\mathrm{min}$, $N = 5$ animals, $n = 9$ measurements) and with external oxygen supply, through the Ringer solution (red, $950\,\mu\mathrm{mol/l}$, $(34.6 \pm 21.1)\,\mathrm{min}$, $N = 7$ animals, $n = 7$ measurements).

carbogen rescue. Moreover, algae and cyanobacteria provided sufficient oxygen to fire at comparable discharge rates as at the beginning of the experiments, i.e. under air-saturated conditions.

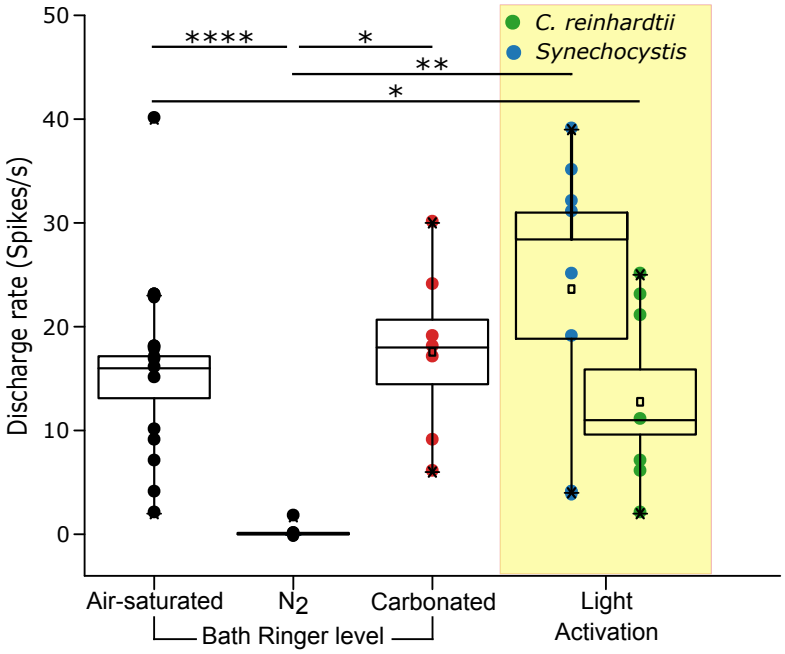

Figure 4.34.: Discharge rates before and after neuronal rescue with light activation – Discharge rates of air-saturated bath Ringer levels ($\sim 290\,\mu\mathrm{mol/l}$) at the beginning of the experiment were monitored as $(10.4 \pm 9.4)\,\mathrm{Hz}$, $N = 16$ animals, $n = 23$ measurements. As the nitrogen was infused into the bath Ringer, discharge rates decreased to $(0.1 \pm 0.4)\,\mathrm{Hz}$, $N = 16$ animals, $n = 23$ measurements. After $5\,\mathrm{min}$ without nerve activity, light illumination (yellow box) or carbonated Ringer solution was induced to rescue neuronal activity. Carbonated Ringer (red) re-establishes a discharge rate of $(12.9 \pm 6.5)\,\mathrm{Hz}$, $N = 7$ animals, $n = 7$ measurements. Illumination of the preparation and therefore photosynthetic oxygen supply with *Synechocystis* (blue) and *C. reinhardtii* (green) re-establishes a discharge rate of $(23.6 \pm 13.5)\,\mathrm{Hz}$, $N = 6$ animals, $n = 8$ measurements and $(12.6 \pm 9.0)\,\mathrm{Hz}$, $N = 5$ animals, $n = 8$ measurements, respectively. * $p \leq 0.1$, ** $p \leq 0.001$, **** $p \leq 0.0001$; Wilcoxon matched-pairs test for each individual experimental group.

5. Discussion

The present work investigated the role of O_2-consumption of the brain in a semi-intact *in vitro* preparation of *Xenopus laevis* larvae by monitoring the O_2-concentration in the IVth ventricle. Additionally, extraocular motor nerve activity was recorded from the superior oblique muscle-innervating trochlear nerve as functional readout. For the first time, the role of O_2-consumption in such an intact preparation during different physiological and pathological conditions was investigated. The thesis identified the function and flexibility of the neuronal network when specific metabolic cycles were inhibited or oxygen was restricted, quantified brain oxygen needs, analyzed oxygen diffusion into the brain, and linked O_2-consumption to neuronal activity by studying the consequences during inhibited (MS-222 application) and increased (spontaneous appearing bursts) neuronal activity. This first part of this thesis is published in Özugur *et al.* [132]. Further, neuronal discharge rescue under hypoxia was accomplished by using photosynthetically produced oxygen from algae and cyanobacteria. The injection of an algae or cyanobacteria suspension into the vascular system distributed the microorganisms through the blood vessels, also into the brain. With light illumination, the internal oxygen supply from microorganisms was sufficient to rescue the neuronal activity from external hypoxia.

5.1. O_2-Consumption due to Neuronal Activity

This thesis showed that the oxygen depletion in the vicinity of neuronal tissue, especially in the IVth ventricle, is due to the O_2-consumption of the brain. Under air-saturated Ringer levels ($\sim$290 µmol/l O_2) all available oxygen is consumed in the vicinity of the tissue of the preparation, started to drop drastically at around 0.8 mm distance to the ventricular floor, and was fully depleted at the floor of the IVth ventricle, see Fig. 4.1. In Fig. 4.2 the generation of the concentration map from Fig. 4.1 is shown. The stepwise positioning of the oxygen sensor into the depth of the IVth ventricle, as shown in Fig. 4.2 a), revealed for all 31 measurements an s-shaped curve of O_2-concentration dependency inside the ventricle, as shown in Fig. 4.2 b). These results indicate an O_2-consumption by the brain, as long as the preparation is metabolically active. This finding was confirmed by using metabolically inactive preparations as will be discussed in the following.

Monitoring EtOH fixed brain samples and after KCN inhibition of the mitochondria during an experiment showed that the brain O_2-consumption is a true sign of metabolic activity and not an artificial morphology driven effect of poor ventilation in the ventricular zone. Increasing external oxygen levels in the bath and simultaneously monitoring the O_2-concentration in the bath and the IV$^{\text{th}}$ ventricle of an EtOH fixed preparation showed a delayed oxygen increase in the ventricle of ~ 15 min relative to the bath concentration, cf. Fig. 4.3 a). The same was found during an inhibition of mitochondrial activity with KCN in an intact preparation, cf. Fig. 4.3 b). To see if there is a possible higher O_2-consumption by the brain with KCN, the oxygen in the surrounding Ringer was increased, but showed the same slope reaching bath concentrations within ~ 15 min, cf. Fig. 4.3 b). This implies that no additional oxygen is consumed when OXPHOS in the mitochondria is inhibited by KCN. Furthermore, in specific cases of the isolated tadpole preparations ~ 15 min are required to adapt to changed environmental conditions, such as external O_2-concentration or inhibitor application. This time is most probably diffusion limited, as blood flow is inactive in the semi-intact *in vitro* preparation. O_2-concentrations in the ventricle showed no significant difference to bath levels in EtOH fixed preparations or after inhibitor (KCN) application. Control measurements of intact *Xenopus laevis* larvae preparations expressed a significant difference between the O_2-concentration in the ventricle or brain tissue, compared to bath values, see Fig. 4.3 c). In addition, when increasing external bath oxygen levels, EtOH and KCN application show the same linear increase in the ventricle, see Fig. 4.3 d). This indicates that an active O_2-consumption is absent in these metabolically-inhibited preparations. Further, the results presented here have shown that there is no limitation for oxygen diffusion in the IV$^{\text{th}}$ ventricle due to the morphological shape, specifically when increasing or decreasing O_2-concentrations in the bath. This highlights once more the application benefits of the semi-intact *in vitro* preparation. Furthermore, the results show that blocking metabolic function with KCN or inactivating the whole preparation with EtOH leads to the same increase in oxygen level in the ventricle. This suggests that mitochondrial activity is coupled to O_2-consumption. Further, the data suggests that mitochondria are the major ATP production source and are required for maintained functionality. This implies that OXPHOS is the metabolic pathway with the largest oxygen turnover.

However, the inhibition of complex IV of OXPHOS with KCN, as part of mitochondrial respiration, might not be the best target for inhibition to entirely block metabolic function. In previous findings the inhibition of complex I was the most effective method to block ATP production and therefore mitochondrial activity [133]. It was shown that inhibition of complex IV with KCN would not lead to a total decrease in ATP production, but to a reduction that is not affecting the overall mitochondrial activity. However, complex IV is

the part of the ATP process where O_2 is consumed. Therefore blocking with KCN may be insufficient to block ATP production completely, however the major O_2-consumption of the mitochondria will be blocked. Comparing the findings following inhibition with KCN and EtOH, no difference was observed, indicating at least a major contribution of complex IV to mitochondrial respiration. In the study of Davey *et al.* the inhibitor application in cell culture took only 5 min [133], which might work in cell cultures, but is too short for a full effect in whole brain preparations, as shown by the present results, cf. Fig. 4.3. The diffusion of the drug through the tissue into the preparation is the likely reason why the application time is longer than in cell cultures to reach a full effect.

Further, the oxygen dynamics in the ventricular zone were analyzed under increased external O_2-concentrations. Higher external oxygen levels lead to a delayed increase in oxygen at the ventricular floor, see Fig. 4.4. The s-shaped relation of the O_2-concentration along the dorso-ventral depth track towards the ventricular floor is shifted to higher O_2-concentrations, as shown in Fig. 4.5 a). Retaining the s-shape when increasing external oxygen levels suggests a more complex correlation of available oxygen and O_2-consumption. However, even though the slope varies with altered external Ringer levels, the vertical oxygen gradient remains. To get a better idea of the O_2-consumption in the brain, external oxygen levels were increased and ventricular oxygen levels were monitored, cf. Fig. 4.5 b). It was shown that for external O_2-concentrations above $\sim 700\,\mu mol/l\ O_2$ the ventricular oxygen increased in a linear manner, indicating an oxygen saturation concentration in the brain around $\sim 700\,\mu mol/l\ O_2$. Beyond this level, all additional oxygen applied to the Ringer solution appears in the ventricle as leftover oxygen. This demonstrated that oxygen levels under air-saturated condition ($\sim 290\,\mu mol/l\ O_2$) are below the saturation level of brain oxygen demands, and thus this is the reason why the ventricle is fully oxygen-depleted in Fig. 4.1. A study by Ivanov *et al.* claims that a relatively low oxygen environment is natural for a significant fraction of cortical neurons [134]. However, not only the O_2-level in the ventricular area but also neuronal discharge rates are not fully saturated under air-saturated Ringer conditions, cf. Fig. 4.17. Carbonated Ringer levels revealed higher discharge rates. This suggests that also the spike firing activity is dependent on oxygen availability. The phenomenon of oxygen toxicity during higher O_2-concentration in the Ringer solution did not appear, showing once more that higher O_2-levels are required for physiological brain function.

Measurements in the ventricular zone showed the same oxygen levels and dynamics as in the nervous tissue in the vicinity of the vestibular nucleus, as shown in Fig. 4.3 c) and Fig. 4.5 b). This is also true for increased oxygen levels up to $\sim 1000\,\mu mol/l\ O_2$. Even the saturation point is the same when measuring the oxygen in the vestibular nucleus and comparing it to the IVth ventricle. Further, the diffusion dynamics of oxygen in the larval

preparation were analyzed within the vestibular nucleus, the ventricle following removal of the choroid plexus, and the ventricle with the choroid plexus above the ventricular zone, as shown in Fig. 4.6. No significant difference of the diffusion duration was found in the three conditions. This indicates that oxygen diffusion is not limited by morphological structures such as the choroid plexus. Introducing the oxygen electrode into the vestibular nucleus on the other hand has some drawbacks. First, measurements in the vestibular nucleus requires the removal of the choroid plexus. Since the aim was to keep the conditions as natural as possible, the removal of the plexus impairs any future comparison with *in vivo* conditions. Second, the insertion of the electrode into the brain destroys tissue, even with the smallest electrode tip with a diameter of 10 µm. The destroyed tissue itself is not the problem but leads to a potential destruction of neuronal networks or pathways of cellular oxygen turnover, thus causing stress and changing cellular response and network interaction. Hence, throughout this work, the electrode was systematically placed in the IV^{th} ventricle at the floor, without touching the tissue to avoid tissue or cell damage.

The oxygen depletion in the IV^{th} ventricle was not solely due to neuronal activity, but strongly dependent on it. This was studied by systematically blocking neuronal activity as shown in Fig. 4.8 and Fig. 4.10. A sodium channel blocker (MS-222) inhibited the neuronal discharge completely, cf. Fig. 4.8 a). Simultaneously monitoring the O_2-concentration in the ventricle during inhibitor application revealed an increase in ventricular O_2-concentration, which was reversible after inhibitor wash-out, cf. Fig. 4.8 b). The oxygen increase, measured in the ventricle, is due to the fact that MS-222 inhibits neural cell activity and O_2-consumption by neuronal processes. MS-222 was used for neuronal inhibition because of the advantage of quickly recovered nerve activity after wash-out. MS-222 has analgesic, sedative, and paralytic characteristics [46]. The inhibitor blocks all excitable cells and therefore also mechanosensory responses. Furthermore, the water solubility of the drug allows amphibians the uptake via the skin. Inhibitory characteristics were shown above 100 µmol/l (0.0026 %), with a total block of neuronal activity at 1000 µmol/l (0.026 %) MS-222 [135]. Further, 0.05 % MS-222 completely inhibits extraocular motor discharge in fish and amphibians including isolated larval *Xenopus* preparations, as was shown by Ramlochansingh *et al.* [46]. According to Ramlochansingh *et al.*, inhibition of motoneurons with 0.05 % MS-222 takes 15 min in semi-intact *in vitro* preparations of *Xenopus laevis* larvae, and a full recovery of neuronal discharge was reported after 4 h [46]. According to Palmer *et al.* lower concentrations of MS-222 have a faster nerve firing recovery [136], that, however, is dependent on the application duration. Since the aim of this study was to recover the neuronal discharge, a reduced drug application time was necessary to guarantee a faster recovery of nerve activity. On the other hand, a complete block of the nerve discharge was necessary in the first place. In this study,

discharge was still ongoing within 40 min of application of 0.05 % MS-222. To reversibly inhibit neuronal discharge, 0.5 % and 0.05 % MS-222 for 10 min and 40 min, respectively, were applied.

The inhibitor wash-in leads to an immediate oxygen increase in the ventricle, together with a cessation of nerve firing, demonstrating the relevance of oxygen for neural activity, cf. Fig. 4.8 b), Fig. 4.10. Comparing O_2-concentrations in the ventricle after 10 min 0.5 % MS-222 and 40 min 0.05 % MS-222 application, respectively, revealed a significant difference to control measurements in both cases, see Fig. 4.9 a).

However, concentrations in the ventricle in both applications (10 min 0.5 % MS-222 and 40 min 0.05 % MS-222) did not reach bath oxygen levels, indicating a residual O_2-consumption likely by non-neuronal tissue and/or house-keeping processes in neurons. In case of 10 min bath application of the local anesthetic 0.5 % MS-222 reduced the O_2-consumption by $\sim$50 %, cf. Fig. 4.9. Similar results were shown before by Huchzermeyer *et al.*, where O_2-consumption in brain slices was found to experience a reduction in oxygen needs by $\sim$40 % during neuronal inhibition [25]. The most likely explanation is that the homeostasis related to spike generation and repolarization, at least in the isolated amphibian brain under *in vitro* conditions, consumes about half of the available oxygen in air-saturated Ringer solutions. This indicates a possible glial cell metabolism and metabolic activity (unrelated to action potential generation in neurons) that utilize a similar amount of oxygen as required for neuronal spike firing. It is well known from mammalian brains that the maintenance of the resting membrane potential, non-signaling processes, and cellular housekeeping (e.g. maintenance of cytoskeleton, membrane structure, etc.) are metabolically demanding processes [64, 137, 138]. As an example, O_2-consumption in mouse hippocampal slices was still substantial during tetrodotoxin-blocked action potentials [24]. A further contribution to O_2-consumption during MS-222-blocked neuronal signaling might be attributed to O_2-diffusion into neighboring areas, where blockage of neural firing might be incomplete.

Washing out the inhibitor leads to a recovery of neuronal firing. This recovery from drug application is time- and dose-dependent [46]. The recovery phase of neuronal discharge was quantified in regard to O_2-consumption, as shown in Fig. 4.11. A strong correlation between O_2-consumption and neuronal discharge rate during the recovery after inhibitor wash-out was observed. MS-222 not only blocks action potential generation through tetrodotoxin-sensitive voltage-dependent Na-channels [139], but also tetrodotoxin-insensitive types of voltage-gated sodium (Nav)-channels as well as calcium (Ca)- and potassium (K)-channels, although with lower sensitivity [140, 141]. These processes are not involved in action potential generation, however, need energy and thus consume oxygen. These and other cellular metabolic pathways unrelated to action potential generation

in neurons explain the early increase in O_2-consumption shortly after MS-222 washout, where nerve firing is still absent. Alternatively, this could be due to the fact that the resting discharge of extraocular motoneurons depends on upstream synaptic activity and intact spike firing in nerve fibers from the inner ear to central vestibular neurons, which activate extraocular motoneurons. While the openly accessible brainstem and IV^{th} ventricle allows a relatively fast Ringer exchange during drug wash-out, the encapsulated inner ear might pose a diffusion barrier both for the washing in and out of MS-222, although the wash-out might be more critical for the initial phase of the recovery.

A late recovery of nerve activity was observed in Fig. 4.10 and Fig. 4.11. Measurements over a long time period showed delayed responses of neuronal activity following MS-222 inhibition. During the late recovery phase, neuronal activity and O_2-consumption in the ventricle are increasing after wash-out of the sodium channel blocker (0.5 % MS-222). The different numbers of multi-unit axonal recordings, which is the basis of different neuronal discharge rates, is the reason for the different slopes of the linear correlation of O_2-consumption and discharge rate in Fig. 4.11 c). Therefore, neither a direct nor an absolute correlation, but rather a strong dependency between neuronal activity and O_2-consumption emerges.

Turning to the O_2-concentration in the depth track of the ventricular zone for the MS-222 inhibition and control, both show an s-shaped correlation between oxygen and distance to the ventricular floor, cf. Fig. 4.9 b). Thereby, a steeper slope for washed in 0.05 % MS-222 as compared to the control was observed. The slope was even steeper if 0.5 % MS-222 was applied. This is in contrast to EtOH brain dead samples [cf. Fig. 4.2 b)], where the O_2-concentration stayed constant throughout the entire depth track. The different slopes can be explained by the oxygen consumers still active during the different conditions. In the control measurement, the entire brain is active and consumes oxygen, including the O_2-consumption by nerve activity. For the MS-222 inhibited cases, the slope is steeper since nerve activity is absent and, as discussed above, other consumers are still active. The constant oxygen along the depth track in inactive brain samples shows that the brains were dead. Thus, the oxygen depletion in the ventricular zone, shown in Fig. 4.1 is due to both, neuronal firing activity and other consumers, in almost equal parts as discussed above.

With the inhibition of extraocular motor commands and mechanosensory responses, it was shown that the semi-intact *in vitro* preparation is an ideal model to study the impact of drugs on specific cells, as neuronal discharge rates and motor outputs can be recorded. Further, the accessibility to the central nervous system (CNS) and the possibility of behavioral readout makes the *in vitro* preparation of *Xenopus laevis* larvae an ideal alternative to *in vivo* experiments [46]. As an alternative to MS-222, there is a

variety of additional drugs that could be applied to test inhibition of activities. Moreover, a combination of multiple drugs washed in as a cocktail could test the complete inhibition of pathways.

5.2. O_2-Consumption Dependency on Burst Duration

During spontaneously occurring bursts (high neuronal activity), the O_2-concentration in the ventricle dropped almost immediately after the start of a burst and recovered quickly to normal O_2-concentrations after the burst ended, cf. Fig. 4.12. At normal Ringer O_2-concentrations ($\sim 290\,\mu mol/l$) brain oxygen needs were not saturated and the ventricular oxygen was completely depleted during a burst. In contrast, at a level of $\sim 626\,\mu mol/l$ O_2, the ventricular oxygen was not fully depleted, cf. Fig. 4.7. Bursts were monitored under elevated external oxygen levels and revealed that the O_2-concentration in the IV^{th} ventricle was not fully depleted, indicating that the brain does not consume all available oxygen during increased neuronal activity, see Fig. 4.13. When measurements are performed not in the saturated condition, see Fig. 4.5 b), O_2-consumption could not be measured correctly and could lead to wrong assumptions. Ivanov *et al.* showed that low oxygenation in the surrounding CSF has an influence on neuronal discharge rates in brain slices of mice [134]. This indicates that an adequate oxygen supply is crucial for maintaining neuronal activity. Therefore, the difference in the O_2-consumption integral in Fig. 4.14 d) was not due to different discharge rates, but to the low external oxygen level.

However, increasing oxygen levels could also have effects on discharge rates. Hence, neuronal activity during varying external bath O_2-concentrations was analyzed, see Fig. 4.17, which showed that external oxygen has an effect on neuronal discharge. This suggests that oxygen, as a key molecule in the energy pathways, limits neuronal activity under air-saturated conditions. This finding was important for the measurements in this thesis, since it allowed to study the O_2-consumption and use of neuronal activity as functional readout. Increasing external oxygen levels is crucial to maintain neuronal cell function.

Further, it was shown that elevated bath O_2-concentrations had neither an impact on the O_2-consumption during a burst, cf. Fig. 4.15, nor on the latency of O_2-consumption onset triggered by a burst, cf. Fig. 4.16 a). After a burst the O_2-concentration recovery time (which was normalized to the burst duration) was dependent on external bath concentrations, cf. Fig. 4.16 b). This suggests that the O_2-diffusion is faster at higher oxygen concentrations. The latency represents the oxygen diffusion time and was quantified as $\sim 14\,s$ until increased neuronal activity affected the O_2-consumption, cf. Fig. 4.16. These measurements, however, differ from previous *in vivo* studies in rats, which have shown a shorter latency of $1.2\,s$ [142]. A possible reason for this difference is that the brain is

consuming oxygen from the tissue storage before external oxygen is consumed, causing the drop that was monitored. Another explanation is that the oxygen drop is not directly linked with the discharge, because recordings were not made directly in the vicinity of the neurons which were activated, but rather in the ventricle where other processes influence the O_2-concentration. The most plausible explanation for the 10× faster oxygen diffusion onset is that the measurements were performed *in vivo* with an functional blood supply, which is faster in oxygen delivery than *in vitro* oxygen diffusion through a solution.

Next, the dependency of burst duration on O_2-consumption was studied. Therefore, the integral of the discharge rate, see Fig. 4.18 a) and c), and integral of the O_2-consumption, see Fig. 4.18 b) and d), at various Ringer O_2-concentrations (O_2 min: 40 µmol/l, O_2 max: 1100 µmol/l) were analyzed, see Fig. 4.15. The O_2-consumption showed a slight increase under higher external O_2-concentrations in comparison to air-saturated Ringer conditions, cf. Fig. 4.19 b), which is most likely due to the fact that at air-saturated Ringer conditions brain oxygen levels were not saturated, as shown in Fig. 4.5. The linear tendency, however broadly scattered, indicating that the O_2-consumption might vary during the bursts.

Brosel *et al.* monitored changes in oxygen during a burst, but not how oxygen levels influenced the discharge rates [22]. In this study the O_2-consumption during increased neuronal activity was ∼ 10 µmol/l to ∼ 50 µmol/l, linearly dependent on the burst duration, as shown in Fig. 4.21. When setting the O_2-consumption in relation to the respective burst duration per second, 0.4 µmol/l O_2 were consumed during high neuronal activity. This indicates, in comparison to the resting O_2-consumption of ∼ 626 µmol/l shown in Fig. 4.7, the oxygen need of motoneuronal activity with a duration of 100 s, is with ∼ 40 µmol/l comparatively small. The oxygen need for neuronal activity in the activated lateral superior olive of gerbil brain slices ranges between 8 µmol/l and 129 µmol/l, is equally small and dependent on stimulus frequency [22]. This suggests that each neuronal pathway and activation of a distinct behavior might not contribute much to the O_2-consumption in total, but collectively cause a substantial oxygen need. Therefore, the understanding and study of the whole brain as a complex network is important.

5.3. Comparison of Oxygen Monitoring *In Vivo* and *In Vitro*

Direct measurements of oxygen in the brain, such as in the IVth ventricle, prove to be very difficult under *in vivo* conditions. This is mostly due to the inaccessibility of the brain tissue, but also due to the need for the correct placement of monitoring instruments, such as oxygen electrodes. Further, *in vivo* experiments need a constant control of vi-

tal parameters of the animal, such as neuronal recording, with simultaneously changing external O_2-concentrations. Oxygen measurements in brain slices (*in vitro*) are easier to perform compared to *in vivo* studies, however, show much higher oxygen values [21]. The O_2-concentration in slice preparation is decreasing with distance to the surface [143], thus *in vitro* studies usually focus on tissue close to the surface. *In vivo* monitoring, on the other hand, is usually performed deeper in the tissue. Additionally, *in vitro* tissue lacks an active blood flow, which *in vivo* experiments still have. Therefore, comparing *in vitro* data to *in vivo* data could lead to wrong assumptions as the oxygen supply is different. To estimate the O_2- / energy-consumption for defined neuronal activity in experiments, semi-intact *in vitro* preparations of *Xenopus laevis* larvae [29] were used. This preparation can maintain sensory and motor function for several days in a Ringer solution and allows to monitor *in vivo*-like behaviors using an *in vitro* approach.

The goal of most experiments is to draw conclusions for human physiology to get a better understanding of key pathways, such as energy or signalling pathways, or the consequence for developing a disease. Additionally, there are also studies on humans which are, however, limited in its applications due to the living suspects. Human fMRI studies showed an O_2-consumption of $\sim 140\,\mu mol/100g/\,min$ in grey matter [144]. As 103.2 g brain tissue is equivalent to 100 ml [145], $\sim 1445\,\mu mol/l/\,min$ O_2 is consumed. These data were collected without stimulation but as an assumption of basal $CMRO_2$ in the human brain. The measurements revealed that the O_2-consumption in the amphibian brain is $\sim 626\,\mu mol/l$ (Fig. 4.7) and that the oxygen diffusion due to increased neuronal activity is reached after ~ 100 s, cf. Fig. 4.15 (oxygen drop until minimum). With these assumptions, the brain O_2-consumption of *Xenopus laevis* larvae is $\sim 376\,\mu mol/l/\,min$, and thus lower than in human studies. It should be noted that these assumptions are based on the above mentioned ~ 100 s since O_2-consumption was not measured as a flow rate but as a concentration. Another plausible explanation for the difference between human and *Xenopus laevis* oxygen monitoring could be that in this study only O_2-concentrations in the ventricle were monitored and other brain areas were not included in the O_2-consumption. Additionally, it is difficult to adjust the brain weight of the *Xenopus laevis* larva to the human brain (density). Further, measurements in humans are usually performed at body temperature (37 °C), whereas O_2 monitoring in the *Xenopus laevis* preparation was performed at (17 ± 0.5) °C. Since O_2-concentration also depends on temperature, oxygen measurements at different temperatures vary. Furthermore, the preparation is a semi-intact *in vitro* preparation, which lacks blood oxygen supply and other vital parameters that would allow a direct comparison to human monitoring. Moreover, and most importantly, the amphibian brain could not be compared that easily to the human brain; even though most pathways, cycles, and metabolic networks are identical, amphibians are

known to have a lower metabolism as mammals, mostly due to lower preferential body temperature. Furthermore, amphibians are more robust, which allows them to live with lower oxygen levels. However, this only means that the animal is able to perform at low oxygen levels, but in total it should need the same oxygen for cell functionality especially since the cells and networks are similar in all vertebrates.

Brain oxygen monitoring was performed in earlier studies with different methods, mostly by monitoring oxygen in brain slices [22]. Some studies measured pO_2 in mmHg [20, 23, 25] or $CMRO_2$ mmol/l/ min [24]. The different approaches in oxygen monitoring make it hard to compare absolute values. In brain slices, oxygen recordings indicated an O_2-consumption of $\sim 3400\,\mu mol/l$ during 37 Hz stimulation for 60 s [24] and an O_2-consumption of $\sim 40\,\mu mol/l$ during an 20 Hz stimulus for 2 s [22]. Huchzermeyer *et al.* reported an O_2-consumption of 179 mmHg during 20 Hz for 10 s [20], whereas Galeffi *et al.* described 120 mmHg for a stimuli of 10 Hz and 20 s [23]. *In vivo* oxygen monitoring in the rodent cortex were performed by Offenhauser *et al.* and Takanao *et al.* provided O_2-consumption values of 38 mmHg for a stimulus of 10 Hz for 15 s [146] and 23 mmHg for a natural appearing O_2-consumption for 60 s [147].

Schneider *et al.* [24] determined the following relation:

$$1\,pO_2\,[\text{mmHg}] \;=\; 0.73\,\mu mol/l, \tag{5.1}$$

with the oxygen partial pressure pO_2 in mmHg and its relation to the O_2-concentration in solution in µmol/l. The data from the following studies of brain activity were converted with Eq. (5.1) to compare results of *in vitro* rodent brain slices [20, 22–24] and *in vivo* rodent cortex measurements [146, 147], and are summarized in Tab. 5.1. To get an idea

Table 5.1.: O_2-consumption *in vitro* vs *in vivo* as found in literature and compared to the results in the present study.

Reference	Exp. design	Stimuli (Hz)	Stimuli (s)	O_2-consumption (mmHg)	O_2-consumption (µmol/l)	O_2-consumption (µmol/l/s)
Schneider [24]	*in vitro*	37	60		3400	57
		spontaneous	60		1700	28
Brosel [22]	*in vitro*	20	2		40	20
Huchzermeyer [20]	*in vitro*	20	10	179	130	13
Galeffi [23]	*in vitro*	10	25	120	88	3.52
Offenhauser [146]	*in vivo*	10	15	38	28	1.8
Takanao [147]	*in vivo*	spontaneous	60	23	17	0.3
Present study	*in vitro*	spontaneous	100		40	0.4

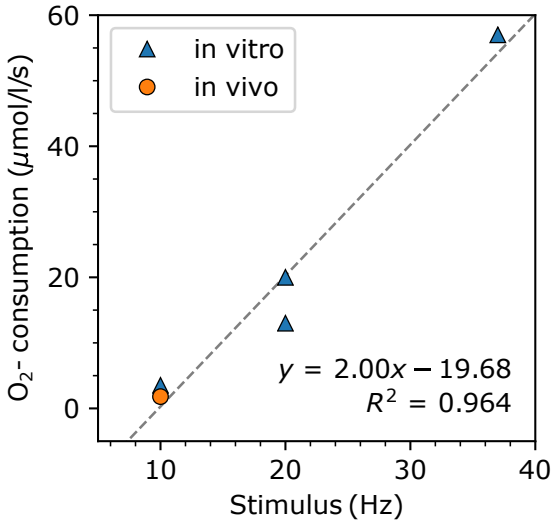

Figure 5.1.: O_2-consumption in previous studies – O_2-consumption dependence on stimulus frequency (Hz) plotted from previous studies. Data taken from Ref. [20, 22–24, 146, 147].

how the different stimulus intensities influence the O_2-consumption, Fig. 5.1 plots the O_2-consumption as function of stimulus, showing a linear correlation. Data recorded from *in vivo* show the smallest values for both, stimulation and O_2-consumption. However, it is not clear why *in vivo* experiments were not performed with stimulation > 10 Hz (as *in vitro* studies were). Regarding only the O_2-consumption of the spike bursts, cf. Fig. 4.15 (oxygen drop until minimum reached after ~ 100 s), an additional O_2-consumption of 0.4 µmol/l per second burst duration to the resting activity is observed, cf. Fig. 4.21. It is nicely demonstrated that the semi-intact *in vitro* preparation recordings are close to *in vivo* studies, as can be seen in Tab. 5.1. This suggests that the experimental setup from this study is more realistic to compare with human studies, than slice recordings.

Hemmingsen's equation, cf. Eq. (2.1), determined an O_2-consumption of 59.11 µl/h, cf. Sec. 2.3, for a whole *Xenopus laevis* larvae of 0.3 g body weight (stage 53, see Fig. 2.2). This is converted into 0.0164 µl/s, which accounts for 0.0007 µmol/s, using the density of O_2 (1.4 g/l) and the atomic weight of O_2 (32 g/mol). In comparison to *in vivo* measurements of the entire O_2-consumption of the *Xenopus laevis* larvae [148], where 0.1109 ml/g/h would be 0.0092 µl/s for a 0.3 g larvae (Stage 53). This is converted into an O_2-consumption of 0.0004 µmol/s and is approximately the same as calculated with Hemmingsen's equation.

5.4. Brain Oxygen Dynamics under Air-Saturated and Increased O_2-Levels

Spontaneously increased neuronal activity, so called spike bursts, resulted in an oxygen drop which depletes all the available oxygen in the ventricle, indicating that higher external oxygen levels were required, cf. Fig. 4.12. This was also shown before by Huchzermeyer *et al.* in rat hippocampal slices, where they monitored larger oxygen transients and larger gamma oscillations during activation with 95 % oxygenation in comparison to 20 % of the surrounding CSF [20]. Further, Hall *et al.* showed that in rat hippocampal slices the monitoring of NADH responses due to activity is not reached with 20 %, but only with 95 % O_2-concentration [21]. This demonstrates that even in brain slices, where oxygen diffusion is not as limited as in intact brain preparations, oxygen needs are not saturated under air-saturated oxygen and a higher external oxygen supply is required to guarantee correct interpretation of the obtained results. In Fig. 4.7 it is shown that the oxygen in the surrounding Ringer solution has to be increased to $\sim 626\,\mu mol/l$ to saturate the IV^{th} ventricle. This can also be seen in Fig. 4.15 c), where for 0 O_2 in the ventricle, the shape of the curve suggests that the oxygen drop is below the maximum extent in response to the burst. The monitored oxygen drop in the ventricle during a burst, with the subsequent recovery back to the initial O_2-level, is unreliable for the cases when the entire O_2-supply is depleted as the consumption and recovery might have been different if more oxygen would have been available. However, it could be that the brain oxygen demand is below the measured value in Fig. 4.7. As others claimed before, a relatively low oxygen environment is natural for a significant fraction of cortical neurons [134]. It might be that oxygen storage in the tissue is used for maintained functionality. Further, it is possible that the O_2-concentration in *in vivo* brains is lower in the brain tissue and higher in the supporting CSF, enabling a constant supply of oxygen and other nutrients. The same O_2-concentrations are measured in the vestibular nucleus and the ventricle, and, moreover, both show the same dynamic when increasing external oxygen levels, as illustrated in Fig. 4.5. This shows that the fluid in the IV^{th} ventricle and the brain tissue form an equilibrium. This is true at least for the O_2-concentration, but most likely also for other (if not all) molecules.

Cilia located on the choroid plexus and the ventricular surface are responsible for the circulation of CSF [149, 150]. The CSF itself has an important function in protecting the brain from shock and vibration, and further, an active circulation of the fluid is important for the removal of waste products from the side of its production and also to transport signal molecules. Nelson *et al.* could show that cilia motion is active up to 3 h following the establishment of an *in vitro* preparation [149]. It was shown in the semi-intact *in vitro*

preparation that the flow inside the ventricle, where the O_2-consumption was measured, was still intact. This explains the same pattern in O_2-concentration in relation to distance of the ventricle floor, when increasing external oxygen levels cf. Fig. 4.5. Cilia movement can circulate the CSF up to a distance of 100 µm [149]. It can be seen in Fig. 4.5 a) that stirring of the solution in the ventricle is effective, because of the lower oxygen concentration rise below 200 µm. This is followed by a steeper rise between 200 µm and 800 µm suggesting a less active circulation, with a slower diffusion driving the exchange of fluid. The s-shape in Fig. 4.5 a), however, can also been explained by the cells in the brain tissue consuming oxygen, with a higher cell number closer to the bottom of the ventricle. Thus, fluid closer to the ventricular floor has less oxygen. Above 800 µm the open ventricle leads to an increase of diffusion, which is above 1000 µm linear and independent of increasing external O_2-concentrations, indicating a fast diffusion process outside the ventricle. This is most likely due to the constant Ringer flow in the setup. In the following experiments, the choroid plexus remained attached to the preparation and only a small hole at the very rostral end of the choroid plexus was made to provide access for the oxygen sensor to reach the ventricle. The circulation by the cilia also on the choroid plexus likely forms a closed circulation. It would be interesting to study the effectiveness of the circulating CSF, as the *in vitro* preparation lacks blood circulation.

5.5. Hypoxia Consequences and Application in Experiments

In humans, the availability of oxygen could be restricted through different external limitations, such as deep-water diving, flying at high altitudes, or strangulation. On the other hand, there are also internal limitations that include smoke inhalation, exposure to toxic chemicals, drug abuse, asthma, stroke, and shock. In particular, the brain is very vulnerable, as oxygen changes could lead to severe injuries, such as cerebral anoxia or Hypoxic Ischemic Encephalopathy (HIE) [10]. Not only long-term damage is observed, but also short-term oxygen shortages could lead to severe damages and to disturbances in cell and network functionality. These shortages could further develop into diseases depending on the affected area, which include Alzheimer's disease, Epilepsy, and Schizophrenia [15]. While for mild hypoxic cases treatments such as inhalation of pure oxygen could help to avoid harmful aftereffects, for severe hypoxic cases, however, these methods are insufficient. Creating new methods based on methodological approaches in non-mammalian vertebrates, such as semi-intact *in vitro* preparations, is of particular clinical interest.

Previously studied characteristics of algae which produce oxygen upon light illumina-

tion [126] were used in the present study to prevent brain damage from hypoxia. Since neuronal damage is complicated to heal after surgical intervention, transplants which can supply oxygen and other nutrients could be beneficial and expedite the healing process. Even to prevent neurodegeneration, transplants are considered to be a possible application. Moreover, the continuous effort to improve the vitality and functionality of isolated amphibian brains [78] or whole heads [29], algae or cyanobacteria application for internal oxygen supply facilitate the survival in experiments and might also be beneficial for *in vivo* approaches. Isolated preparations of *Xenopus* tadpoles, which allow concurrent measurements of behavior-specific neuronal computations as well as O_2-concentrations under controllable conditions, are promising model systems to test the applicability of algae and cyanobacteria in an animal model and for quantification of intrinsic oxygen supply. In this study, a new methodological approach was performed to rescue neuronal activity from hypoxia. Using algae or cyanobacteria as oxygen source itself is not novel. In clinical environments, algae-skin-transplants have previously been used for wound recovery [52, 54]. However, injection into the vascular system allows the microorganisms to spread into every blood vessel of the body, including those in the brain. The novel method developed within the framework of this thesis, called 'Synthetic Oxygen Supply' (SOS), could be used in *in vivo* or in *in vivo*-like experiments, where oxygen supply is critical.

An environmental hypoxia was produced by enriching the Ringer solution with N_2 causing a decrease of the oxygen level to a minimum of $\sim 40\,\mu mol/l$. From previous hypoxia experiments in fish (*Gnathonemus petersii*) it is known that activity is severely affected below $25\,\mu mol/l$ [151]. However, the study from Nilsson claims that air-saturation is reached with $156\,\mu mol/l$, which is almost half the concentration of what was monitored when air-saturation ($290\,\mu mol/l$) was achieved in the present study, cf. App. A.3. It might be that the O_2-concentration differs from a variation in salt content in the solution, but as they used a similar CSF Ringer solution the difference is probably negligible. Therefore, their minimum oxygen value was assumed to correspond to minimum of $40\,\mu mol/l$ in this study. Due to diffusion and surface exchange of gas molecules, it might only be possible to reach lower oxygen values if closing the measurement chamber. Additional gas in the closed chamber at slightly higher concentrations than in the solution avoids a larger diffusion into the air as the pressure works against it. The diffusion was minimized and bubbling in a high-rise chamber directly upstream to the measurement chamber was applied. The high rise of the bubbling chamber had the advantage of a decreased surface, as the opening diameter was only $\sim 0.5\,cm$.

Inducing hypoxia in the semi-intact *in vitro* preparation while recording neuronal discharge lead to a maintained firing for $\sim 25\,min$ with a wide variety or rates that ranged

from 2 min to 60 min, cf. Fig. 4.33 a) (Control). In adult *Xenopus laevis*, diving periods can last up to 40 min [100], assuming that this time represents the oxygen storage after air-breathing without considering oxygen uptake via the skin. As oxygen reservoirs in the skin are small and negligible [101], oxygen supply is only covered by the lung reservoir and, to a small amount, by skin diffusion. Folkow *et al.* monitored hypoxia in mice and seal (*Cystophora cristata*) brain slices and recorded neuronal activity up to 5 min (mouse) and 19 min (seal) [152]. Seals are known to be rather hypoxia tolerant as they can dive for long time periods without breathing. However, cell responses to hypoxia are not only species dependent but also changes based on cell type and brain region [152]. In slices of rat brainstem tissue, hypoglossal neurons and layer II/III neocortical neurons were studied by O'Reilly *et al.* and the response to oxygen deprivation of these neuronal population was quantified [153]. They showed that hypoglossal neurons did not recover from long anoxic periods, which was better tolerated by neocortical neurons. For hypoglossal neurons, hypoxia-induced depolarizations lasted only 3 min, while neocortical neurons were more heterogeneous and the depolarization lasted for 19 min [153].

Taken together, this demonstrates that the maintenance of neuronal oxygen deprivation is not only area and cell population dependent but also shows heterogeneity between populations. Measurements in the present study showed likewise a broad variability in different outcomes, leading to the conclusion that the maintenance of hypoxia is difficult to measure and not often quantifiable within a study or comparable between different neuronal populations. For the present study the most important aspect, however, was to rescue neuronal activity during hypoxia and the extraocular motor nerve recording served as functional readout. For the interpretation of these experiments, the calculated time until neuronal discharge ceased was not a focus, while the time until neuronal discharge recovered was systematically quantified.

5.6. Algae and Cyanobacteria as Oxygen Supply

Measurements of O_2-production in isolated algae and cyanobacteria (Sec. 4.3.1) showed a significant difference between both, *Synechocystis* and *C.reinhardtii*. Whereas *Synechocystis* produced $\sim 2800\,\mu mol/l$ upon 5400 lux light illumination with a concentration of 0.5×10^9 cells/ml, *C.reinhardtii* produced only $\sim 1500\,\mu mol/l$ under the same conditions. *Synechocystis* produced almost two times the amount of oxygen with the same amount of light as *C.reinhardtii*. This changed when the concentration of both algae and cyanobacteria were reduced to 0.1×10^9 cells/ml, where *Synechocystis* produces $\sim 18\,\%$ less than the same amount of *C.reinhardtii* when illuminating with 5400 lux. For the larger-sized algae *C.reinhardtii* (10 µm) variation in cell concentration does not make a

difference in maximal O_2-production. For *Synechocystis* (2 µm), on the other hand, a change in concentration from 0.1×10^9 cells/ml to 0.5×10^9 cells/ml yields an increase in O_2-production, which amounts to about 55 % for the 5400 lux and 137 % for 30 500 lux. This indicates that higher cell numbers produce larger oxygen quantities in *Synechocystis*, as most likely these single celled organisms were activated by light more easily than the larger-sized cells of *C.reinhardtii*. However, in general *C.reinhardtii* was as good as *Synechocystis* at higher concentrations, leading to the assumption that the O_2-production is more efficient in these eukaryotic algae. Larger cells overlap in the solution and during light illumination not all cells might be reached by the light, thus less cells were activated, especially at higher cell concentrations.

A phototoxic effect was not observed for illuminations of up to 30 500 lux. However, an increase in oxygen productivity in both species, especially at higher cell concentrations, was observed. There was an increase in O_2-production at lower cell concentrations as well when the illumination was more intense, particularly for *C.reinhardtii*. This could mean that the bigger cells of *C.reinhardtii* are able to exploit higher light intensities more efficiently than *Synechocystis*. Haraguchi *et al.* provided data from isolated and co-cultivated algae of *Chlorococcum littorale* [154], a green algae comparable in size to *C.reinhardtii*, which were used in experiments in the present study. They monitored O_2-concentrations produced by the isolated algae of ~ 2800 µmol/l for 0.1×10^9 cells/ml, comparable to the measurements in the present study of ~ 2200 µmol/l during 5400 lux light activation, cf. Fig. 4.22. Previous reports claim that the optimal light intensity for *C.reinhardtii* is 6000 lux, which is below the illumination from indirect sunlight [130] and close to the light illumination of 5400 lux, used in the present study. Direct sunlight has a luminance of 10 000 lux, which leads to a reduction in productivity [130]. However, Akimoto *et al.* found that at 12 000 lux *C.reinhardtii* had less lipid yields, but positive growing rates per day [155]. In the present study, at least for the O_2-production rate a reduction in productivity was not the case for isolated algae and cyanobacteria, as both species showed an increase with both concentrations at 30 500 lux. To further study the capacity of algae and cyanobacteria to transform sunlight into oxygen without harm or negative effects, it would be necessary to further increase light intensities. The maximum intensity that was achieved with the light source was 30 500 lux. Even if it is not intended by nature to cope with such high light levels, algae and cyanobacteria could be more productive. On the other hand, if the microorganisms are not isolated in pure media, but in an experimental context such as in the vascular system of an animal, phototoxicity could become a problem, since the cells are more diluted and vulnerable.

The results presented here showed that algae or cyanobacteria injections into the vascular system, by entering the injection electrode into the heart of the anesthetized larvae,

spread the microorganisms throughout the blood vessels. Through the distribution inside the blood vessels, microorganisms reached the choroid plexus above the IVth ventricle and were even able to spread into small blood vessels in the brain tissue, cf. Fig. 4.24. To show that algae and cyanobacteria were located in the blood vessels, blood vessel walls were stained with Isolectin and imaged through coronal sections of a blood vessel, cf. Fig. 4.25, Fig. 4.26, and Fig. 4.27. Applying microorganisms directly into the blood vasculature is a new approach and could be highly relevant, especially since it was shown that the algae and cyanobacteria could reach areas deep inside the brain tissue. Alvarez *et al.* reported that injected *C.reinhardtii* did not move in the zebrafish body, except if the algae entered the blood vascular system [53]. If algae or cyanobacteria could cross the vasculature, actively or passively, the injection into the vasculature would lead to a distribution throughout the whole body and the brain tissue, which could not be confirmed in the present study. It would be also problematic if the microorganism could cross vascular walls, because other interactions like neuron-microorganism could cause problems for the signal transduction. However, the oxygen supply would be more effective as the diffusion distance becomes minimal. Since in nature the oxygen supply originates from haemoglobin in the blood (at least in most vertebrates) the injected algae or cyanobacteria in the vasculature, as in this study, should prove sufficient.

From Lametschwandtner *et al.* it is known that arteries in the IVth ventricle of *Xenopus laevis* are located ventral and dorsal on top of the choroid plexus [156], which was removed for the confocal imaging in the present study, and with it also the blood vessels. Isolectin staining was used for visualizing the vasulature, which does not differentiate between veins and arteries. The location of veins in contrast to the arteries is more distributed. The stainings showed the distribution of algae and cyanobacteria in larger and smaller vasculature, cf. Fig. 4.25. That leads to the assumption that the microorganisms are distributed in both, veins and arteries. Since the preparation after the surgical isolation lacks an active blood circulation, algae and cyanobacteria remained distributed for the purpose of the present study to supply the brain with oxygen. Algae or cyanobacteria inside the vasculature of the preparation simply replaces blood cells.

Naturally, algae and cyanobacteria form clumps, which has a negative effect with larger clumps blocking light from reaching other algae or cyanobacteria [157]. However, those clump formation did not occur in the injection experiments. Either because the concentration of the algae and cyanobacteria was too high and they would clump at lower concentrations, or they were stressed through the high pressure during the injection such that they were not behaving the same in the vessels as isolated microorganisms. Long-term studies to follow algae or cyanobacteria behavior in the blood vessels, such as their motion or survival, would be a necessary study for future experiments. It might be cru-

cial to inject further nutrients that the microorganisms need for survival or add them into the Ringer solution constantly such that the supply does not become limited. Long-term measurements were performed before, however, at smaller algae concentration. Alvarez *et al.* injected 10 000 algae/µl *C.reinhardtii* into zebrafish yolk and analyzed the viability within the following 5 days in the developing embryo [53]. The algae remained metabolically active for at least 3 days and did not activate immune responses in the zebrafish. They recognized the algal appearance in pairs, which might be a hint to replication within the fish body [53] and therefore a sign for viability.

To monitor the photosynthetic O_2-production capacity of algae and cyanobacteria in the preparation, external bath O_2-concentration was increased to ~ 900 µmol/l to avoid that brain O_2-consumption interferes with the algal O_2-production, cf. Fig. 4.30. The O_2-production triggered by light activation of the microorganisms was ~ 174 µmol/l. The data was divided to monitor the O_2-production of *C.reinhardtii* and *Synechocystis* separately, and compared to control measurements of their respective photomutants, cf. Fig. 4.30. The O_2-production from *Synechocystis* (190 µmol/l) and *C.reinhardtii* (159 µmol/l) showed no statistical significance in difference. *Chlorococcum littorale* (green alga) was co-cultivated with mammalian cells (C2C12 mouse myoblasts) and revealed an O_2-concentration during light illumination of 218.75 µmol/l for 2.5×10^7 cells [154], which translates to $\sim 0.218\,75$ µmol/l for the cell concentration that was calculated in the brain vasculature in the present study (250 000 cells). In comparison, the amount of oxygen measured in the ventricle produced from injected microorganisms produced 190 µmol/l (*Synechocystis*) and 159 µmol/l (*C.reinhardtii*), respectively, cf. Fig. 4.31. However, in the study by Haraguchi *et al.* on *Chlorococcum littorale* only 1103 lux for illumination was used, which is a relatively low intensity. Potentially the cells in culture are more vulnerable and sensitive to high light intensities. It might be possible that the O_2-production of algae in their setup would be higher if they would have increased light illuminance to 5400 lux, the optimum of the photosystem activation. However, *Chlorococcum littorale* alga's O_2-production efficiency could be less than in *C.reinhardtii* or *Synechocystis*. Further, they performed their experiments under air-saturated conditions (20 % oxygen), which might be less of a problem in cell culture, as gas diffusion is fast because of the small diffusion distances, but could lead to wrong assumptions as algae were co-cultivated with mammalian cells, which were consuming oxygen that the algae had just produced. Furthermore, the authors found in cell culture a decrease in glucose consumption, lactate production, and much less ammonium concentration if algae were co-cultivated with cardiac cells from rats [154]. This hints to a shift in energy metabolism. ATP is produced mostly by OXPHOS if enough oxygen is available, which seemed to be the case in algal-co-cultivation. Glycolysis and lactate shuttle are reduced, since they are not as efficient in ATP produc-

tion in comparison to OXPHOS. Further, ammonia, a waste product in the amino acid degradation in animal cells, is reduced through the consumption of ammonia by the algae or cyanobacteria in order to maintain their own functionality. Ammonia is important for algae and cyanobacteria growth and survival, as it contains nitrogen [154]. The advantage behind reduced ammonia concentrations in the co-cultivated cells is that the cells degraded amino acids for their own metabolism, setting ammonia free as a waste product. The ammonia is taken up by the algae and cyanobacteria as precious nitrogen source and, further, chloroplasts also produce glutamate [158]. This indicates that a combination of algae or cyanobacteria and mammalian cell is beneficial for both parties and could be developed further, to fit the needs of both.

Monitoring O_2-production of photomutants helped to facilitate the demonstration that the oxygen was exclusively produced by the algae and cyanobacteria through photosynthesis. These photomutants fail to produce oxygen upon light illumination, as they are lacking PS II. The O_2-production of the photomutants (together with WT and CTL) is shown in Fig. 4.31. The negative value of O_2-production in *C.reinhardtii* photomutants reflects a light-dependent O_2-consumption which is likely due to chlororespiratory effects in *C.reinhardtii* chloroplasts [159]. In the prokaryote *Synechocystis*, the cells contain no organelles and thus no separation of respiratory and photosynthetic electron transport pathways, no such light-dependent O_2-consumption is observed [160]. The monitored O_2-consumption from Fig. 4.31 is also in agreement with the theoretical calculations in App. A.6, where it is shown that *C.reinhardtii* consume more oxygen than *Synechocystis*. Also in the isolated experiments, *C.reinhardtii* consume more O_2 than *Synechocystis*, cf. Fig. 4.22. The slightly positive O_2-production of *Synechocystis* mutants in Fig. 4.31 could be caused by a reduced O_2 need of the brain. This reduced O_2 need could also be present in *C.reinhardtii* mutants and most likely also in the WT of both species, however, is masked by the light induced O_2-production (WT) or O_2-consumption (*C.reinhardtii*, mutant). This is in comparison to controls, where no microorganisms were present in the brain's vasculature, and no O_2-production or O_2-consumption was measured.

Using the photosynthetic oxygen as brain oxygen supply, it could be shown that enough oxygen is produced by the microorganisms to rescue neuronal activity, cf. Fig. 4.32. Comparing neuronal rescue with external bath oxygen supply (carbogen treatment of $\sim 950\,\mu mol/l$) O_2, which took 34.6 min, light activation of algae and cyanobacteria, was faster for both microorganisms, *C.reinhardtii* with 22 min and significantly faster for *Synechocystis* with 14 min, cf. Fig. 4.33. A plausible explanation for the faster recovery with algal oxygen is that this oxygen is directly produced in the brain tissue, even distributed in deep brain tissue. In controls, where the external bath O_2-concentration was increased by carbogen, the oxygen requires more time to diffuse from the Ringer solution into the

ventricular zone and from there into the tissue. This alone might not explain the large difference in recovery time. However, the diffusion process is most likely not homogeneous and oxygen does not reach all brain regions simultaneously. This is in contrast to algae and cyanobacteria, which could supply oxygen to every region given the distribution in the blood vessels.

The discharge rate as functional readout served here as an important measurement to proof the sufficiency of photosynthetic oxygen. In Fig. 4.34 the discharge rate before nitrogen treatment was used as control (10.4 Hz). During nitrogen treatment (hypoxia) discharge rate dropped to 0.1 Hz and was rescued either with carbogen treatment of the external Ringer solution (12.9 Hz) or with light activation, thus photosynthetic oxygen from microorganisms (*Synechocystis*: 23.6 Hz, *C.reinhardtii*: 12.6 Hz). Therefore, the vascular microorganisms could provide enough oxygen to drive neuronal activity under external hypoxia.

During hypoxia the nerve activity ceased, which is called the nerve cessation time. In Fig. 4.33 a) the data from the cessation time was not significantly different for both microorganisms and the control, where no algae or cyanobacteria were injected. It is important to find out whether there are consequences for the animal to have algae or cyanobacteria located inside its blood vessels. However, the control measurement without algae or cyanobacteria showed no difference in cessation time. This indicates that algae or cyanobacteria inside blood vessels did not alter oxygen availability in the brain for cell activity. In particular, in *C.reinhardtii* where oxygen is consumed by their own mitochondria, cf. Fig. 4.31, neuronal firing maintenance due to oxygen availability is not affected. This indicates that microorganisms in the vasculature do not affect *Xenopus laevis* larvae at least with regard to oxygen use or need.

The shift of energy production from OXPHOS to glycolysis, which occurs during high energy needs as in wound recovery [49], is critical for the healing process. Energy production cannot rely on oxygen delivery, as oxygen delivery is diminished in wounded tissue. The shift to glycolysis, which is not dependent on oxygen supply to produce ATP, is the only logic step to prevent energy loss. However, glycolysis is less efficient to produce ATP in comparison to OXPHOS [58]. This decreased ATP supply could be a reason why wound recovery is diminished. Instead of down-regulating mitochondrial ATP production, additional oxygen supply by algae or cyanobacteria could prevent the shift to glycolysis and promote OXPHOS in the energy production for a faster recovery.

6. Concluding Remarks

Brain activity requires large amounts of energy, mostly provided by oxygen-dependent metabolic processes. In many animals and humans alike, oxygen derives from respiration through lungs or gills and is transported by red blood cells within the vascular system to all regions of the body. The brain of most animals and humans require a constant supply of oxygen through persistent blood flow. If this persistent supply becomes imbalanced or interrupted, short- and long-term effects including severe brain diseases could evolve. Therefore, a basic understanding of the network, the flexibility of the brain to endure oxygen deprivation, and an alternative oxygen supply is important to study. This was done successfully in this thesis.

6.1. Conclusion

Experiments on the brain in *in vivo* studies are complicated to perform, because animal surgery is complex and during experiments a constant maintenance of vital parameters is necessary and extensive. The ease of maintaining *in vitro* brain slices, on the other hand, often lack the comparability to an intact brain. Here, entire head preparations of *Xenopus laevis* tadpoles with intact brains were used, which are comparable to *in vivo* studies, as they still have functional sensory- and motor-control. *Xenopus laevis* is, as an amphibian, a less oxygen-demanding organism, and allows to perform experiments on O_2-consumption in the brain even at physiological conditions that normally become very critical. These conditions include extreme external oxygen levels (e.g. 40 µmol/l O_2 or 1200 µmol/l O_2), inhibition of mitochondria as the major energy source, and inhibition of neuronal activity.

The present study showed that the ventricular depletion of oxygen is due to metabolic activity of the adjacent brain tissue, cf. Sec. 4.1, and that the external oxygen level has to be above $\sim$626 µmol/l to saturate brain O_2-consumption. Further, neuronal activity has a major contribution to the O_2-consumption in the ventricle, cf. Sec. 4.2, as shown by neuronal inhibition (MS-222). The recovery phase of inhibitor wash-out revealed a strong correlation of oxygen depletion and neuronal activity, as the neuronal discharge and O_2-consumption increased both in a linear manner. Furthermore, an increased neuronal

activity (spike burst) consumed more oxygen and the O_2-consumption was dependent on the duration of the increased firing phase. The additional oxygen need for a spike burst was found to be $\sim 0.4\,\mu mol/l/s$, cf. Fig. 4.21. Furthermore, it was shown that increased external O_2-concentrations had an effect on neuronal discharge rates, cf. Fig. 4.17, and on the recovery time to original O_2-concentrations in the ventricle after a burst was encountered, cf. Fig. 4.16 b). However, external oxygen levels had no influence on the latency for the onset of the oxygen drop during a burst [Fig. 4.16 a)]. That makes external oxygen levels an important contributor for neuronal discharge activity.

On the other hand, several implications or diseases have to cope with an inadequate oxygen supply, thus studying hypoxia in the brain is important to get a better understanding of compensating mechanisms or possible intrusion points for therapy. The major advantage of *Xenopus laevis* is that the survival under hypoxia for several minutes is possible. This makes *Xenopus laevis* larvae an ideal model to test new approaches that could overcome hypoxia. Algae or cyanobacteria can supply photosynthetic oxygen to the larvae, even faster than external oxygen, if the microorganisms are inside the larva, such as in the vasculature. During the present study it was shown that injections of algae or cyanobacteria into the vascular system of *Xenopus laevis* enables a distribution through the entire animal, and even into the brain. Thus, oxygen can be produced where it is needed, simply by light illumination—via photosynthesis—, permitting the larvae to be fully independent from external oxygen sources. This approach is called 'Synthetic Oxygen Supply' (SOS). In the first step, the parameters (light illumination and cell concentration) were characterized for optimizing O_2-production in isolated algae (*C.reinhardtii*) and cyanobacteria (*Synechocystis*), cf. Sec. 4.3. Distribution of microorganisms through the vasculature after the injection into the heart of the larvae was visible by the tadpole's overall green vasculature. With the injection, the blood in the vasculature was replaced with algae or cyanobacteria. Imaging the brain and the choroid plexus above the ventricle, which is usually filled with oxygen supplying blood cells, revealed a distribution of microorganisms throughout the brain blood vessels. Removal of the choroid plexus revealed that the microorganisms were distributed through the entire brain vasculature. Comparing *C.reinhardtii* (10 µm in size) and *Synechocystis* (2 µm in size) inside blood vessels at a higher magnification of single blood vessels showed that both types of microorganisms fit into the larva's vasculature. The O_2-production capacity of microorganisms in the *Xenopus laevis* brain was quantified with illumination of the preparation at higher external oxygen levels. *C.reinhardtii* produced 159 µmol/l O_2 and *Synechocystis* produced 190 µmol/l O_2, cf. Fig. 4.31. The present study showed that the O_2-consumption of the larva's brain remains unaltered by the algae or cyanobacteria, cf. Fig. 4.33 a). Further, under hypoxia, photosynthetic oxygen via light illumination was sufficient to rescue neu-

ronal activity, cf. Fig. 4.32. Microorganisms inside the brain vasculature could supply oxygen faster (*Synechocystis*: 14 min, *C.reinhardtii*: 22 min) than external oxygen supply (35 min), cf. Fig. 4.33 b). External oxygen supply has longer diffusion distances from the surrounding Ringer solution through tissue and skin into the brain. Further, the discharge recovery from hypoxia, showed that the photosynthetic oxygen derived from microorganisms is sufficient to drive neuronal activity, cf. Fig. 4.34.

Experiments on *in vitro* preparations lack blood perfusion and therefore could limit the experiment. Algae or cyanobacteria can replace blood cells in the vasculature and supply the tissue with oxygen upon illumination. With SOS as internal oxygen source, *in vitro* preparations are closer to *in vivo* experiments and open a new field that enables approaches on intact brains.

6.2. Outlook

SOS is a promising method to study and represents an excellent addition to *in vitro* experiments, where oxygen diffusion is diminished, to guarantee permanent oxygen supply during critical experiments. The variety of photosynthetic microorganisms enables applications within a broad field. The different sizes of green algae or the smaller cyanobacteria allow the application for vasculatures of various morphologies and can be coordinated to each application, for example the brain vasculature needs smaller microorganisms then the vasculature of the dermis. Further, besides oxygen production other nutrients could be produced additionally from genetically modified microorganisms [47, 126], allowing to adjust the supply for the individual approach. Modified algae or cyanobacteria can produce growth factors that help for instance to achieve a faster wound healing. With algae and cyanobacteria injections into the vasculature, such microorganisms can reach deep into tissue and supply oxygen and other nutrients to the whole body. This could be an advantage for *in vivo* experiments, where a quick supply is necessary or the influence of a nutrient, produced by the microorganisms, is of interest. SOS opens a new field of experiments that enables independent oxygen supply simply with light illumination.

A. Appendix

A.1. Chemicals

- Buffer solution pH 4,00 ± 0,02 (20 °C), ROTI®CALIPURE citric acid / sodium hydroxide / sodium chloride
- Buffer solution pH 7,00 ±0,01 (20 °C), ROTI®STAR potassium dihydrogenphosphate / sodium phosphate dibasic
- Buffer solution pH 9,00 ±0,02 (20 °C), ROTI®CALIPURE boric acid / sodium hydroxide / potassium hydroxide
- Ringer solution 75 mmol/l NaCl; 2 µmol/l KCl; 1.05 µmol/l MgCl; 12.1 µmol/l D-Glucose; 25 µmol/l $NaHCO_3$; and 25 µmol/l $CaCl_2$ were solved in ddH_2O to a end volume of 1 l. The Ringer was equilibrated with 10 µmol/l HEPES to hold the pH of 7.4 constant at low oxygen levels.
- NaOH 0.1 mol/l: 0.4 g NaOH in 100 ml Ringer
- Ascorbic acid 0.1 mol/l: 2 g in 100 ml 0.1 mol/l NaOH
- MS-222 0.5 %: 0.5 g in 100 ml Ringer
- MS-222 0.05%: 0.05 g in 100 ml Ringer
- KCN 500 µmol/l: 50 µmol/l Stock in ddH_2O, 1 ml 50 µmol/l Stock in 100 ml Ringer
- Isolectin GS-IB4 from *Griffonia simplicifolia*, Alexa Fluor™ 488 Conjugate from Thermo Fisher Scientific: 2 µl (Stock: 200 mmol/l) in 10 µl end-volume

A.2. Abbreviations

ATP	Adenosine triphosphate
C.reinhardtii	*Chlamydomonas reinhardtii*
Ca	Calcium
CB	Cerebellum
CNS	Central nervous system
CSF	Cerebrospinal Fluid
CTL	Control
EPSP	Excitatory postsynaptic potential
FADH2	Flavin adenine dinucleotide
Gly	Glycolysis
HIE	Hypoxic Ischemic Encephalopathy
K	Potassium
KCN	Potassium cyanide
MP	Mesencephalon
MS-222	3-Aminobenzoic acid ethyl ester methanesulfonate
Na	Sodium
Nav	Voltage-gated sodium channel
NADH	Nicotinamide adenine dinucleotide (reduced derivative)
NADPH	Nicotinamide adenine dinucleotide phosphate (reduced derivative)
OXPHOS	Oxydative phosphorylation
PS I	Photosystem I
PS II	Photosystem II
RB	Rhombencephalon
ROS	Reactive oxygen species
RT	Room temperature
SEM	Standard error of the mean
SO	Superior Oblique muscle-innervating trochlear nerve
SOS	Synthetic Oxygen Supply
Synechocystis	*Synechocystis* sp. PCC 6803
TAP	Tris-acetate-phosphate
TAPS	Tris-acetate-phosphate with 1 % (w/v) sorbitol
TCA	Tricaboxylic acid
WT	Wild type

A.3. Oxygen Sensor Calibration

Oxygen levels of the calibration Ringer were calculated following Ref. [161] with

$$GS_{\text{salt}} = GS - (k \times s), \tag{A.1}$$

where GS_{salt} is the concentration of soluble oxygen in saltwater (mg/l), GS the concentration of soluble oxygen in H_2O (mg/l), k the constant variable with temperature, and s (‰) the concentration of the salt in the liquid. The temperature dependence of the constant k and GS is summarized in Tab. A.1.

Table A.1.: Temperature dependence of k and GS (mg/l). Values for k and GS (mg/l) for temperatures between 15 °C and 19 °C. Taken from Ref. [161]

T (°C)	k	GS (mg/l)
15	0.05602	10.15
16	0.05456	9.94
17	0.05328	9.75
18	0.05201	9.54
19	0.05073	9.35

The oxygen content in the Ringer at 18 °C is obtained as follows:

$$\begin{aligned} GS_{\text{salt}}\,[\text{mg/l}] &= GS\,[\text{mg/l}] - (k \times s\,[‰]), \\ &= 9.54 - (0.05201 \times 6.9458), \\ &= 9.17875\,\text{mg/l}. \end{aligned} \tag{A.2}$$

With the molar mass of oxygen $n_{O_2} = 31.9988\,\text{g/mol}$, the oxygen concentration in the Ringer solution follows to

$$\begin{aligned} C_{O_2} &= \frac{GS_{\text{salt}}}{n_{O_2}}, \\ &= \frac{9.17875\,\text{mg/l}}{31.9988\,\text{g/ml}}, \\ &= 286.8466\,\mu\text{mol/l}. \end{aligned} \tag{A.3}$$

Table A.2.: Calculation of Ringer components and end salt concentration.

Ringer components	Stock (g/100ml)	End Conc. (g/l)
NaCl	43.83	4.383
$NaHCO_3$	21.002	2.1002
KCl	1.491	0.1491
Glucose	21.8	2.18
$MgCl_2$	4	0.1
$CaCl_2$	2.94	0.294
HEPES		2.38
H_2O		1000
SUM (g/l)		1011.5863
Salt (g/l)		7.0263
Salt (g/kg)		**6.9458**

Ringer Air-Saturated The Ringer components and end salt concentration are summarized in Tab. A.2. The calculations lead to a concentration of 286.85 µmol/l O_2, cf. Eq. (A.3), corresponding to 9.18 mg/l, in Ringer at 18 °C with respect to the salt concentrations indicated above. In comparison: Water without salt has 298.14 µmol/l O_2, corresponding to 9.54 mg/l, as $(k \times s)$ is close to 0, cf. Eq. (A.2), because the salt concentration is negligible and GS as concentration of soluble oxygen in H_2O is 9.54 mg/l.

A.4. Absorption Spectra of Chlorophyll a and b

Synechocystis has its absorption peaks at 430 nm and 662 nm, corresponding to chlorophyll a, whereas *Chlamydomonas reinhardtii* has chlorophyll a and b, hence has its absorption peaks also at 454 nm, 643 nm, cf. Fig. A.1 a). With the light source Zeiss CLS 6000 [orange line in Fig. A.1 b)] for the experiments with isolated algae and cyanobacteria and experiments with intact larval brains, absorption peaks of 450 nm and 550 nm could be reached. These wavelengths can activate both chlorophyll a and b.

A.5. Brain-Blood-Volume Calculation

The confocal image from Fig. 4.25 was reconstructed to calculate the blood volume, see Fig. A.2. With the reconstruction of the brain z-stack, blood vessel volume could be calculated with with the software Vision 4D from Arivis, cf. Tab. A.3. The calculation

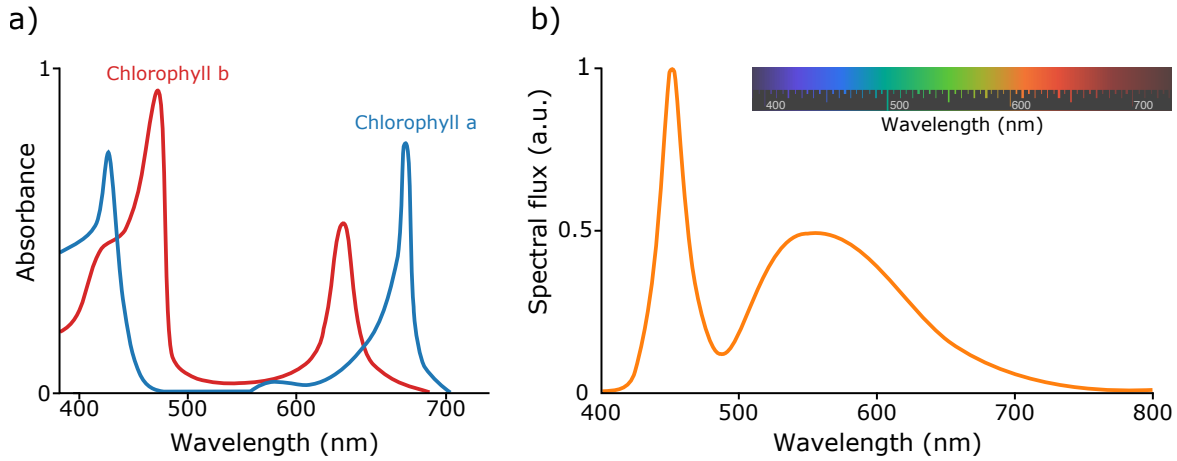

Figure A.1.: Absorbance spectra – a) Chlorophyll absorbance, figure adapted from https://en.wikipedia.org/wiki/Chlorophyll and is used under a CC BY-SA 3.0 licence, accessed: 09/06/2019 and b) emission spectra of the light source Zeiss CLS6000, orange line), figure adapted from: https://www.ehlert-partner.de/BILDER/ZettEmmissionsspektren.jpg, accessed: 09/06/2019.

revealed a blood vessel volume of 206 901 707 µm^3 and an algae or cyanobacteria volume of 32 698 686 µm^3, cf. Tab. A.4.

With the reconstruction of the entire brain, the blood vessels could be calculated to a total volume of 0.207 µl. The algae or cyanobacteria injection volume into the heart was 10 µl, cf. Sec. 3.2.3, where only 0.033 µl were measured in the brain, which is 0.3 %. The injection volume of 10 µl corresponds to 48 times the brain blood volume with 0.207 µl.

Table A.3.: Blood volume and algae and cyanobacteria volume calculation.

	Blood vessels Isolectin (AF488)	Algae / Cyanobacteria Chorophyll (autofluorescence)
Min µm^3	0.093	0.093
Max µm^3	201856945.636	4820373.047
Sum µm^3	206901707.194	32698686.577
Mean µm^3	72.342	755.954
Count	2860053	43255

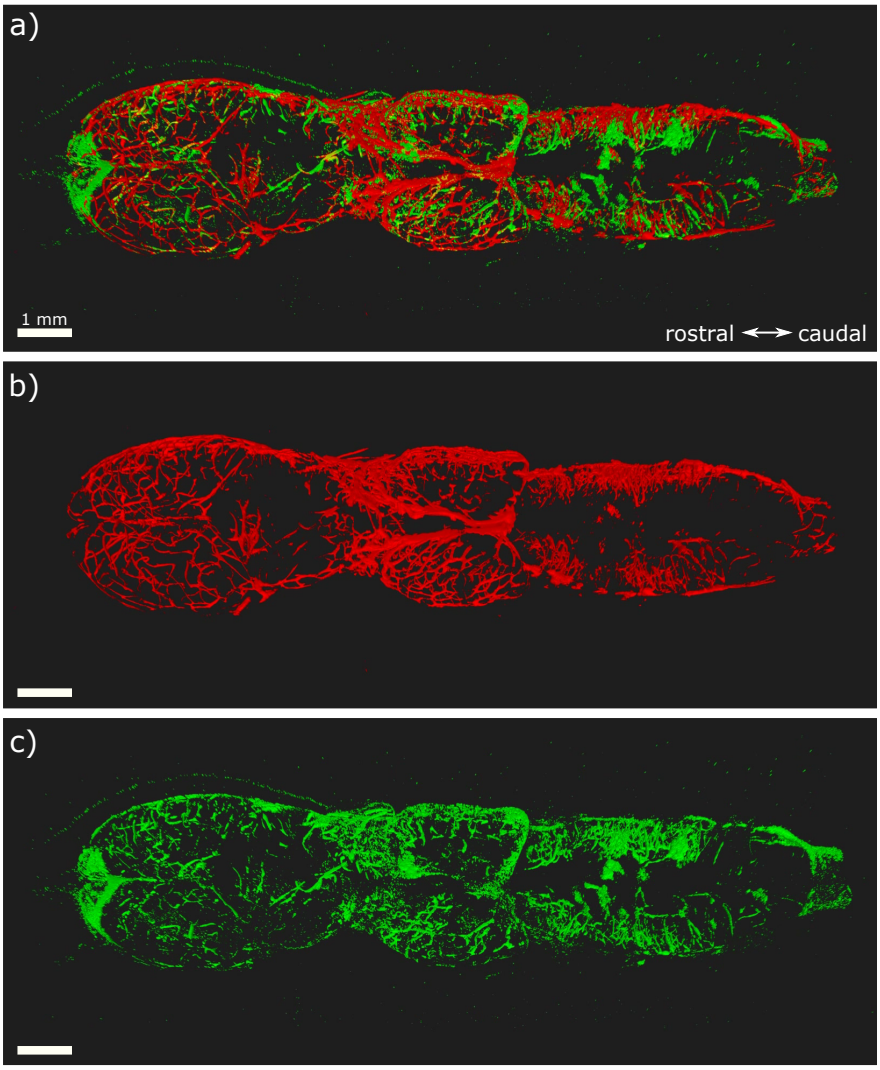

Figure A.2.: Reconstruction of the vascular system in the *Xenopus laevis* brain (the picture shows injected *Synechocystis*) – a) Confocal Image of the entire brain (z-stack) from a dorsal view shows the distribution of algae and cyanobacteria in the blood vessels. b) Blood vessels were stained with Isolectin Alexa Fluor $488\,\mathrm{nm}$ conjugate (red), c) algae and cyanobacteria autofluorescence $680\,\mathrm{nm}$ (green). Taken by Zeiss LSM 900-Airyscan-2 and reconstructed with the software Vision 4D from Arivis.

Table A.4.: Blood volume and algae and cyanobacteria volume conversion.

Blood vessels	Algae / Cyanobacteria	Dimension
206901707	32698686	$\mu\mathrm{m}^3$
0.20690171	0.032698686	mm^3
0.20690171	0.032698686	$\mu\mathrm{l}$

A.6. Theoretical Algae and Cyanobacteria O_2-Consumption

Usually the algae and cyanobacteria O_2-consumption is masked by their O_2-production. However, using photomutants, cf. Sec. 3.2 which can not produce oxygen and therefore only use oxygen from their surrounding, the O_2-consumption can be monitored.

A.6.1. Injected Algae and Cyanobacteria in the *Xenopus laevis* Brain

From the brain-blood-volume calculations in App. A.5, 0.033 mm^3 cells are filling the brain vasculature. Assuming that this volume is filled entirely with cells, and that a single cell of *Synechocystis* has a volume of 4.2 µm^3 (2 µm in diameter), a total of 7.8×10^6 cells are in the brain vasculature. For the *Synechocystis*, measurements performed by the Nickelsen lab determined that 1 mg Chlorophyll consumes 14 nmol oxygen per hour. Further, our OD measurements determined that 10.2×10^6 cells contain 1 µg Chlorophyll. With that, the oxygen consumption of 7.8×10^6 cells cyanobacteria in the brain consume 0.011 nmol oxygen per hour. To compare this number to the oxygen measurements using the oxygen microsensors, which measure the oxygen concentration in µmol/l, the theoretical O_2-consumption is then calculated to 5.45 µmol/l/min O_2.

The same calculation can be done for the *C.reinhardtii*. Beardall *et al.* determined that 1 mg Chlorophyll consumes 2.4 µmol oxygen per hour [122]. Note the much higher O_2-consumption as compared to the *Synechocystis*. Here, our OD measurements determined that 1.3×10^6 cells contain 1 µg Chlorophyll. Since *C.reinhardtii* are much larger (10 µm in diameter) than *Synechocystis*, the volume of 0.033 mm^3 cells in the brain only contain 6.2×10^4 cells. These 6.2×10^4 cells algae in the brain consume 0.11 nmol oxygen per hour, or 57.9 µmol/l/min O_2.

A.6.2. Isolated Algae and Cyanobacteria

Similarly, measurements in isolated *C.reinhardtii* and *Synechocystis* were performed with their respective photomutants, cf. Sec. 3.2.4. These photomutans were lacking a gene to encode PS II. Therefore, these algae and cyanobacteria mutants were not able to produce oxygen upon light illumination. However, the O_2-consumption is still present. The photomutant microorganisms are not masking the oxygen measurements because of the lack of oxygen production and therefore were used to compare the O_2-consumption to the theoretical O_2-consumption. The cell concentration of the isolated microorganisms was 100×10^6 cells per ml.

Under the same assumption as in App. A.6.1, the O_2-consumption of the isolated *Synechocystis* is 0.14 nmol/h and of the isolated *C.reinhardtii* is 181.9 nmol/h, respectively.

Table A.5.: O_2-consumption of injected and isolated algae and cyanobacteria.

	Synechocystis		*C.reinhardtii*	
	brain	isolated	brain	isolated
cell number	7.8×10^6	100×10^6	0.062×10^6	100×10^6
nmol/h	0.011	0.14	0.11	181.9
µmol/l/min	5.45	5.45	57.89	57.89

Bibliography

[1] R. J. Youle and D. P. Narendra, Mechanisms of Mitophagy, Nat. Rev. Mol. Cell. Biol. **12**, 9 (2011).

[2] M. Damiano, L. Galvan, N. Déglon, and E. Brouillet, Mitochondria in Huntington's Disease, Biochimica et Biophysica Acta (BBA) - Molecular Basis of Disease **1802**, 52 (2010).

[3] S. Brosel, C. Laub, A. Averdam, A. Bender, and M. Elstner, Molecular Aging of the Mammalian Vestibular System, Ageing Res. Rev. **26**, 72 (2016).

[4] E. Bullmore and O. Sporns, The Economy of Brain Network Organization, Nat. Rev. Neurosci. **13**, 336 (2012).

[5] D. Attwell and S. B. Laughlin, An Energy Budget for Signaling in the Grey Matter of the Brain, J. Cereb. Blood Flow Metab. **21**, 1133 (2001).

[6] J. W. Mink, R. J. Blumenschine, and D. B. Adams, Ratio of Central Nervous System to Body Metabolism in Vertebrates: Its Constancy and Functional Basis, Am. J. Physiol. Regul. Integr. Comp. Physiol. **241**, R203 (1981).

[7] A. Ames, CNS Energy Metabolism as Related to Function, Brain Res. Rev. **34**, 42 (2000).

[8] D. Singer, Neonatal Tolerance to Hypoxia: A Comparative-Physiological Approach, Comp. Biochem. Physiol. A Mol. Integr. Physiol. **123**, 221 (1999).

[9] J. Larson, K. L. Drew, L. P. Folkow, S. L. Milton, and T. J. Park, No Oxygen? No Problem! Intrinsic Brain Tolerance to Hypoxia in Vertebrates, J. Exp. Biol. **217**, 1024 (2014).

[10] J. Bernat and E. Wijdicks, Coma, Vegetative State, and Brain Death, in *Goldman L, Schafer Al, Eds. Goldman-Cecil Medicine* (Elsevier Saunders, 2016).

[11] Maryland Institute for Emergency Medical Services Systems, *The Maryland Medical Protocols for Emergency Medical Services Providers*, Tech. Rep. (Insitute for emergency medical services systems, 2019).

[12] R. F. Butterworth, Hypoxic Encephalopathy, Basic Neurochemistry: Molecular, Cellular and Medical Aspects. 6th edition (1999).

[13] L. Flicker, The Handbook of Geriatric Assessment, 4th Edition Editors: J. J. Gallo, H. R. Bogner, T. Fulmer and G. J. Paveza Sudbury, Massachusetts: Jones and Bartlett Publishers, 2006, U.S. Hardback, 471 Pp. ISBN-10 0 7637 3056 4, Int. Psychogeriatr. **19**, 796 (2007).

[14] J. Engel, T. A. Pedley, and J. Aicardi, *Epilepsy: A Comprehensive Textbook* (Lippincott Williams & Wilkins, 2008).

[15] P. M. Conn, *Neuroscience in Medicine* (Springer Science & Business Media, 2008).

[16] P. Gancia and G. Pomero, Brain Cooling Therapy, Minerva Pediatr. **62**, 173 (2010).

[17] P. Popovic and V. Popovic, Survival of Newborn Ground Squirrels after Supercooling or Freezing, Am. J. Physiol. Legacy Content **204**, 949 (1963).

[18] J. Laurance, Cooling 'cure' Averts Infant Brain Damage — The Independent, https://www.independent.co.uk/life-style/health-and-families/health-news/cooling-cure-averts-infant-brain-damage-1795740.html (2009).

[19] Mayo Clinic, Hyperbaric Oxygen Therapy, https://www.mayoclinic.org/tests-procedures/hyperbaric-oxygen-therapy/about/pac-20394380 (2017).

[20] C. Huchzermeyer, K. Albus, H.-J. Gabriel, J. Otáhal, N. Taubenberger, U. Heinemann, R. Kovács, and O. Kann, Gamma Oscillations and Spontaneous Network Activity in the Hippocampus Are Highly Sensitive to Decreases in pO2 and Concomitant Changes in Mitochondrial Redox State, J. Neurosci. **28**, 1153 (2008).

[21] C. N. Hall, M. C. Klein-Flügge, C. Howarth, and D. Attwell, Oxidative Phosphorylation, Not Glycolysis, Powers Presynaptic and Postsynaptic Mechanisms Underlying Brain Information Processing, J. Neurosci. **32**, 8940 (2012).

[22] S. Brosel, B. Grothe, and L. Kunz, An Auditory Brainstem Nucleus as a Model System for Neuronal Metabolic Demands, Eur. J. Neurosci. **47**, 222 (2018).

[23] F. Galeffi, G. G. Somjen, K. A. Foster, and D. A. Turner, Simultaneous Monitoring of Tissue pO2 and NADH Fluorescence during Synaptic Stimulation and Spreading Depression Reveals a Transient Dissociation between Oxygen Utilization and Mitochondrial Redox State in Rat Hippocampal Slices, J .Cereb. Blood Flow Metab. **31**, 626 (2011).

[24] J. Schneider, N. Berndt, I. E. Papageorgiou, J. Maurer, S. Bulik, M. Both, A. Draguhn, H.-G. Holzhütter, and O. Kann, Local Oxygen Homeostasis during Various Neuronal Network Activity States in the Mouse Hippocampus, J. Cereb. Blood Flow Metab. **39**, 859 (2019).

[25] C. Huchzermeyer, N. Berndt, H.-G. Holzhütter, and O. Kann, Oxygen Consumption Rates during Three Different Neuronal Activity States in the Hippocampal CA3 Network, J. Cereb. Blood Flow Metab. **33**, 263 (2013).

[26] C. S. Drapaca, Mathematical Modeling of a Brain-on-a-Chip: A Study of the Neuronal Nitric Oxide Role in Cerebral Microaneurysms, Emerg. Sci. J. **2**, 366 (2018).

[27] N. Berndt, O. Kann, and H.-G. Holzhütter, Physiology-Based Kinetic Modeling of Neuronal Energy Metabolism Unravels the Molecular Basis of NAD(P)H Fluorescence Transients, J .Cereb. Blood Flow Metab. **35**, 1494 (2015).

[28] W. W. Burggren and A. W. Pinder, Ontogeny of Cardiovascular and Respiratory Physiology in Lower Vertebrates, Annu. Rev. Physiol. **53**, 107 (1991).

[29] H. Straka and J. Simmers, Xenopus Laevis: An Ideal Experimental Model for Studying the Developmental Dynamics of Neural Network Assembly and Sensory-Motor Computations, Dev. Neurobiol. **72**, 649 (2012).

[30] H. Straka and N. Dieringer, Electrophysiological and Pharmacological Characterization of Vestibular Inputs to Identified Frog Abducens Motoneurons and Internuclear Neurons In Vitro, Eur. J. Neurosci. **5**, 251 (1993).

[31] F. Branoner, B. P. Chagnaud, and H. Straka, Ontogenetic Development of Vestibulo-Ocular Reflexes in Amphibians, Front. Neural Circuits **10** (2016), 10.3389/fncir.2016.00091.

[32] F. M. Lambert, J. C. Beck, R. Baker, and H. Straka, Semicircular Canal Size Determines the Developmental Onset of Angular Vestibuloocular Reflexes in Larval Xenopus, J. Neurosci. **28**, 8086 (2008).

[33] H. Straka, Basic Organization Principles of the VOR: Lessons from Frogs, Prog. Neurobiol. **73**, 259 (2004).

[34] H. Straka, B. Fritzsch, and J. C. Glover, Connecting Ears to Eye Muscles: Evolution of a 'Simple' Reflex Arc, Brain. Behav. Evol. **83**, 162 (2014).

[35] H. Straka, S. Biesdorf, and N. Dieringer, Canal-Specific Excitation and Inhibition of Frog Second-Order Vestibular Neurons, J. Neurophysiol. **78**, 1363 (1997).

[36] H. Straka, R. Baker, and E. Gilland, The Frog as a Unique Vertebrate Model for Studying the Rhombomeric Organization of Functionally Identified Hindbrain Neurons, Brain Res. Bull. **57**, 301 (2002).

[37] H. Straka, S. Holler, and F. Goto, Patterns of Canal and Otolith Afferent Input Convergence in Frog Second-Order Vestibular Neurons, J. Neurophysiol. **88**, 2287 (2002).

[38] F. Goto, H. Straka, and N. Dieringer, Expansion of Afferent Vestibular Signals After the Section of One of the Vestibular Nerve Branches, J. Neurophysiol. **84**, 581 (2000).

[39] C. M. Gravot, A. G. Knorr, S. Glasauer, and H. Straka, It's Not All Black and White: Visual Scene Parameters Influence Optokinetic Reflex Performance in *Xenopus Laevis* Tadpoles, J. Exp. Biol. **220**, 4213 (2017).

[40] S. Hänzi and H. Straka, Developmental Changes in Head Movement Kinematics during Swimming in *Xenopus Laevis* Tadpoles, J. Exp. Biol. **220**, 227 (2017).

[41] B. Sakmann and E. Neher, Patch Clamp Techniques for Studying Ionic Channels in Excitable Membranes, Annu. Rev. Physiol. **46**, 455 (1984).

[42] M. Djupsjöbacka, H. Johansson, M. Bergenheim, and U. Sandström, A Multichannel Hook Electrode for Simultaneous Recording of up to 12 Nerve Filaments, J. Neurosci. Methods **52**, 69 (1994).

[43] E. Florey and M. E. Kriebel, A New Suction-Electrode System, Comp. Biochem. Physiol. **18**, 175 (1966).

[44] D. Combes, S. D. Merrywest, J. Simmers, and K. T. Sillar, Developmental Segregation of Spinal Networks Driving Axial- and Hindlimb-Based Locomotion in Metamorphosing Xenopus Laevis, J. Physiol. **559**, 17 (2004).

[45] F. Branoner and H. Straka, Semicircular Canal-Dependent Developmental Tuning of Translational Vestibulo-Ocular Reflexes in Xenopus Laevis, Dev. Neurobiol. **75**, 1051 (2015).

[46] C. Ramlochansingh, F. Branoner, B. P. Chagnaud, and H. Straka, Efficacy of Tricaine Methanesulfonate (MS-222) as an Anesthetic Agent for Blocking Sensory-Motor Responses in Xenopus Laevis Tadpoles, PLOS ONE **9**, e101606 (2014).

[47] C. Centeno-Cerdas, M. Jarquín-Cordero, M. N. Chávez, U. Hopfner, C. Holmes, D. Schmauss, H.-G. Machens, J. Nickelsen, and J. T. Egaña, Development of Photosynthetic Sutures for the Local Delivery of Oxygen and Recombinant Growth Factors in Wounds, Acta Biomater. **81**, 184 (2018).

[48] A. L. Farris, A. N. Rindone, and W. L. Grayson, Oxygen Delivering Biomaterials for Tissue Engineering, J. Mater. Chem. B **4**, 3422 (2016).

[49] L. Gould, P. Abadir, H. Brem, M. Carter, T. Conner-Kerr, J. Davidson, L. DiPietro, V. Falanga, C. Fife, S. Gardner, E. Grice, J. Harmon, W. R. Hazzard, K. P. High, P. Houghton, N. Jacobson, R. S. Kirsner, E. J. Kovacs, D. Margolis, F. M. Horne, M. J. Reed, D. H. Sullivan, S. Thom, M. Tomic-Canic, J. Walston, J. Whitney, J. Williams, S. Zieman, and K. Schmader, Chronic Wound Repair and Healing in Older Adults: Current Status and Future Research, Wound Repair Regen. **23**, 1 (2015).

[50] F. M. Davis, A. Kimball, A. Boniakowski, and K. Gallagher, Dysfunctional Wound Healing in Diabetic Foot Ulcers: New Crossroads, Curr. Diab. Rep. **18**, 2 (2018).

[51] M. Gholipourmalekabadi, S. Zhao, B. S. Harrison, M. Mozafari, and A. M. Seifalian, Oxygen-Generating Biomaterials: A New, Viable Paradigm for Tissue Engineering? Trends Biotechnol. **34**, 1010 (2016).

[52] T. L. Schenck, U. Hopfner, M. N. Chávez, H.-G. Machens, I. Somlai-Schweiger, R. E. Giunta, A. V. Bohne, J. Nickelsen, M. L. Allende, and J. T. Egaña, Photosynthetic Biomaterials: A Pathway towards Autotrophic Tissue Engineering, Acta Biomater. **15**, 39 (2015).

[53] M. Alvarez, N. Reynaert, M. N. Chávez, G. Aedo, F. Araya, U. Hopfner, J. Fernández, M. L. Allende, and J. T. Egaña, Generation of Viable Plant-Vertebrate Chimeras, PLOS ONE **10**, e0130295 (2015).

[54] U. Hopfner, T.-L. Schenck, M.-N. Chávez, H.-G. Machens, A.-V. Bohne, J. Nickelsen, R.-E. Giunta, and J.-T. Egaña, Development of Photosynthetic Biomaterials for in Vitro Tissue Engineering, Acta Biomater. **10**, 2712 (2014).

[55] X. Zheng, L. Boyer, M. Jin, J. Mertens, Y. Kim, L. Ma, L. Ma, M. Hamm, F. H. Gage, and T. Hunter, Metabolic Reprogramming during Neuronal Differentiation from Aerobic Glycolysis to Neuronal Oxidative Phosphorylation, eLife **5**, e13374 (2016).

[56] U. Bai and M. D. Seidman, A Specific Mitochondrial DNA Deletion (mtDNA4977) Is Identified in a Pedigree of a Family with Hearing Loss, Hear. Res. **154**, 73 (2001).

[57] R. W. Baloh, I. Lopez, K. Beykirch, A. Ishiyama, and V. Honrubia, Clinical-Pathologic Correlation in a Patient with Selective Loss of Hair Cells in the Vestibular Endorgans, Neurology **49**, 1377 (1997).

[58] OpenStax, Rice University, Glycolysis - Biology - OpenStax CNX, https://cnx.org/contents/GFy_h8cu@9.85:tYtpI6rX@6/Glycolysis.

[59] F. Eyassu and C. Angione, Modelling Pyruvate Dehydrogenase under Hypoxia and Its Role in Cancer Metabolism, R. Soc. Open Sci. **4** (2017), 10.1098/rsos.170360.

[60] M. Bonora, S. Patergnani, A. Rimessi, E. De Marchi, J. M. Suski, A. Bononi, C. Giorgi, S. Marchi, S. Missiroli, F. Poletti, M. R. Wieckowski, and P. Pinton, ATP Synthesis and Storage, Purinergic Signal. **8**, 343 (2012).

[61] B. Chance, H. Sies, and A. Boveris, Hydroperoxide Metabolism in Mammalian Organs. Physiol. Rev. **59**, 527 (1979).

[62] C. C. W. Hsia, A. Schmitz, M. Lambertz, S. F. Perry, and J. N. Maina, Evolution of Air Breathing: Oxygen Homeostasis and the Transitions from Water to Land and Sky, in *Comprehensive Physiology* (American Cancer Society, 2013) p. 849.

[63] J. Astrup, P. Sørensen, and H. Sørensen, Oxygen and Glucose Consumption Related to Na+-K+ Transport in Canine Brain, Stroke **12**, 726 (1981).

[64] C. Howarth, P. Gleeson, and D. Attwell, Updated Energy Budgets for Neural Computation in the Neocortex and Cerebellum, J. Cereb. Blood Flow Metab. **32**, 1222 (2012).

[65] T. Hashimoto, M. Yonetani, and H. Nakamura, Selective Brain Hypothermia Protects against Hypoxic-Ischemic Injury in Newborn Rats by Reducing Hydroxyl Radical Production, The Kobe journal of the medical sciences **49**, 83 (2004).

[66] T. Owen, R. D. Cess, and V. Ramanathan, Enhanced CO 2 Greenhouse to Compensate for Reduced Solar Luminosity on Early Earth, Nature **277**, 640 (1979).

[67] S. J. Gould, The Evolution of Life on the Earth, Scientific American **271**, 84 (1994).

[68] J. N. Maina, Structure, Function and Evolution of the Gas Exchangers: Comparative Perspectives, J. Anat. **201**, 281 (2002).

[69] J. B. Graham, An Evolutionary Perspective for Bimodal Respiration: A Biological Synthesis of Fish Air Breathing, Integr. Comp. Biol. **34**, 229 (1994).

[70] M. Tate, R. E. McGoran, C. R. White, and S. J. Portugal, Life in a Bubble: The Role of the Labyrinth Organ in Determining Territory, Mating and Aggressive Behaviours in Anabantoids, J. Fish Biol. **91**, 723 (2017).

[71] G. P. Wells, Lancelot Thomas Hogben. 9 December 1895-22 August 1975, Biographical Memoirs of Fellows of the Royal Society **24**, 183 (1978).

[72] M. Suzuki, A. Satoh, H. Ide, and K. Tamura, Nerve-Dependent and -Independent Events in Blastema Formation during Xenopus Froglet Limb Regeneration, Dev. Biol. **286**, 361 (2005).

[73] H. Liu, P. Etter, S. Hayes, I. Jones, B. Nelson, B. Hartman, D. Forrest, and T. A. Reh, NeuroD1 Regulates Expression of Thyroid Hormone Receptor $B2$ and Cone Opsins in the Developing Mouse Retina, J. Neurosci. **28**, 749 (2008).

[74] K. M. Gibbs and B. G. Szaro, Tracing Central Nervous System Axon Regeneration in Xenopus, Cold Spring Harb. Protoc. **2018**, pdb.prot101030 (2018).

[75] J. B. Gurdon and N. Hopwood, The Introduction of Xenopus Laevis into Developmental Biology: Of Empire, Pregnancy Testing and Ribosomal Genes, Int. J. Dev. Biol. **44**, 43 (2000).

[76] P. Nieuwkoop and J. Faber, *Normal Table of Xenopus Laevis (Daudin): A Systematical and Chronological Survey of the Development from the Fertilized Egg till the End of Metamorphosis*, Vol. 2 (Garland Pub., 1994).

[77] Y. Yaoita, Tail Resorption During Metamorphosis in Xenopus Tadpoles, Front. Endocrinol. **10** (2019), 10.3389/fendo.2019.00143.

[78] J. Hackett, Electrophysiological Properties of Neuronal Circuits in the Frog Cerebellum in Vitro, Brain Res. **48**, 385 (1972).

[79] S. L. Cochran, P. Kasik, and W. Precht, Pharmacological Aspects of Excitatory Synaptic Transmission to Second-Order Vestibular Neurons in the Frog, Synapse **1**, 102 (1987).

[80] H. Straka and N. Dieringer, Internuclear Neurons in the Ocular Motor System of Frogs, J. Comp. Neurol. **312**, 537 (1991).

[81] L. Sun, M. M. Bertke, M. M. Champion, G. Zhu, P. W. Huber, and N. J. Dovichi, Quantitative Proteomics of Xenopus Laevis Embryos: Expression Kinetics of Nearly 4000 Proteins during Early Development, Sci. Rep. **4**, 1 (2014).

[82] J. Voyles, D. C. Woodhams, V. Saenz, A. Q. Byrne, R. Perez, G. Rios-Sotelo, M. J. Ryan, M. C. Bletz, F. A. Sobell, S. McLetchie, L. Reinert, E. B. Rosenblum, L. A. Rollins-Smith, R. Ibáñez, J. M. Ray, E. J. Griffith, H. Ross, and C. L. Richards-Zawacki, Shifts in Disease Dynamics in a Tropical Amphibian Assemblage Are Not Due to Pathogen Attenuation, Science **359**, 1517 (2018).

[83] C. Martin, R. Ibáñez, L.-F. Nothias, C. Boya, L. K. Reinert, L. A. Rollins-Smith, P. C. Dorrestein, and M. Gutiérrez, Viscosin-like Lipopeptides from Frog Skin Bacteria Inhibit Aspergillus Fumigatus and Batrachochytrium Dendrobatidis Detected by Imaging Mass Spectrometry and Molecular Networking, Sci. Rep. **9**, 1 (2019).

[84] M. Leslie, Study of Frog Tuberculosis May Help Unlock Secrets of Human Disease, https://news.stanford.edu/news/2000/may31/frogTB-531.html (2000).

[85] H. Liu, Z. Duan, J. Tang, Q. Lv, M. Rong, and R. Lai, A Short Peptide from Frog Skin Accelerates Diabetic Wound Healing, FEBS J. **281**, 4633 (2014).

[86] D. R. Buchholz, More Similar than You Think: Frog Metamorphosis as a Model of Human Perinatal Endocrinology, Dev. Biol. **408**, 188 (2015).

[87] A. Bernareggi, Z. Dueñas, J. M. Reyes-Ruiz, F. Ruzzier, and R. Miledi, Properties of Glutamate Receptors of Alzheimer's Disease Brain Transplanted to Frog Oocytes, PNAS **104**, 2956 (2007).

[88] G. Zucca, A. Maracci, V. Milesi, M. Trimarchi, E. Mira, M. Manfrin, S. Quaglieri, and P. Valli, Osmolar Changes and Neural Activity in Frog Vestibular Organs, Acta Oto-Laryngo. **115**, 34 (1995).

[89] N. Dieringer, The Role of Compensatory Eye and Head Movements for Gaze Stabilization in the Unrestrained Frog, Brain Res. **404**, 33 (1987).

[90] W. K. Milsom, Intermittent Breathing in Vertebrates, Annu. Rev. Physiol. **53**, 87 (1991).

[91] J. N. Maina and G. M. O. Maloiy, A Scanning and Transmission Electron Microscopic Study of the Lung of a Caecilian Boulengerula Taitanus, J. Zool. **215**, 739 (1988).

[92] D. Toews and D. Macintyre, Respiration and Circulation in an Apodan Amphibian, Can. J. Zool. **56**, 998 (1978).

[93] H. Lillywhite and P. Maderson, Structure and Permeability of Integument1 — Integrative and Comparative Biology — Oxford Academic, https://academic.oup.com/icb/article/28/3/945/99248 (2019).

[94] G. J. Tattersall and W. W. Burggren, Xenopus and the Art of Oxygen Maintenance, J. Exp. Biol. **220**, 4084 (2017).

[95] D. L. Levy and R. Heald, Biological Scaling Problems and Solutions in Amphibians, Cold Spring Harb. Perspect. Biol. **8**, a019166 (2016).

[96] H. Szarski, The Structure of Respiratory Organs in Relation to Body Size in Amphibia, Evolution **18**, 118 (1964).

[97] M. G. Emilio and G. Shelton, Carbon Dioxide Exchange and Its Effects on pH and Bicarbonate Equilibria in the Blood of the Amphibian, Xenopus Laevis, J. Exp. Biol. **85**, 253 (1980).

[98] G. J. Tattersall, S. Currie, and D. M. LeBlanc, Pulmonary and Cutaneous O2 Gas Exchange: A Student Laboratory Exercise in the Frog, Adv. Physiol. Educ. **37**, 97 (2013).

[99] G. Gottlieb and D. Jackson, Importance of Pulmonary Ventilation in Respiratory Control in the Bullfrog, Am. J. Physiol. Legacy Content **230**, 608 (1976).

[100] R. G. Boutilier and G. Shelton, The Effects of Forced and Voluntary Diving on Ventilation, Blood Gases and pH in the Aquatic Amphibian, Xenopus Laevis, J. Exp. Biol. **122**, 209 (1986).

[101] R. G. Boutilier and G. Shelton, Gas Exchange, Storage and Transport in Voluntarily Diving Xenopus Laevis, J. Exp. Biol. **126**, 133 (1986).

[102] R. J. Wassersug and M. E. Feder, The Effects of Aquatic Oxygen Concentration, Body Size and Respiratory Behaviour on the Stamina of Obligate Aquatic (Bufo Americanus) and Facultative Air-Breathing (Xenopus Laevis and Rana Berlandieri) Anuran Larvae, J. Exp. Biol. **105**, 173 (1983).

[103] M. G. Emilio and G. Shelton, Gas Exchange and Its Effect on Blood Gas Concentrations in the Amphibian, Xenopus Laevis, J. Exp. Biol. **60**, 567 (1974).

[104] H. J. Rhodes, R. J. Stevenson, and C. L. Ego, Male-Male Clasping May Be Part of an Alternative Reproductive Tactic in Xenopus Laevis, PLoS One **9** (2014), 10.1371/journal.pone.0097761.

[105] E. R. Miller and M. E. Fowler, *Fowler's Zoo and Wild Animal Medicine, Volume 8 - E-Book* (Elsevier Health Sciences, 2014).

[106] R. G. Boutilier and G. Shelton, Respiratory Properties of Blood from Voluntarily and Forcibly Submerged Xenopus Laevis, J. Exp. Biol. **121**, 285 (1986).

[107] A. N. Hemmingsen, Energy Metabolism as Related to Body Size and Respiratory Surfaces, and Its Evolution, Rep. Steno meml. Hosp. **9**, 1 (1969).

[108] H. S. Winwood-Smith and C. R. White, Short-Duration Respirometry Underestimates Metabolic Rate for Discontinuous Breathers, J. Exp. Biol. **221** (2018), 10.1242/jeb.175752.

[109] Y. Tanaka, T. Miyajima, I. Koike, T. Hayashibara, and H. Ogawa, Translocation and Conservation of Organic Nitrogen within the Coral-Zooxanthella Symbiotic System of Acropora Pulchra, as Demonstrated by Dual Isotope-Labeling Techniques, J. Exp. Mar. Biol. Ecol. **336**, 110 (2006).

[110] W. K. Fitt, B. E. Brown, M. E. Warner, and R. P. Dunne, Coral Bleaching: Interpretation of Thermal Tolerance Limits and Thermal Thresholds in Tropical Corals, Coral Reefs **20**, 51 (2001).

[111] A. M. Szmant and N. J. Gassman, The Effects of Prolonged "Bleaching" on the Tissue Biomass and Reproduction of the Reef Coral Montastrea Annularis, Coral Reefs **8**, 217 (1990).

[112] D. Allemand, P. Furla, and S. Bénazet-Tambutté, Mechanisms of Carbon Acquisition for Endosymbiont Photosynthesis in Anthozoa, Can. J. Bot. **76**, 925 (1998).

[113] M. L. Neo, W. Eckman, K. Vicentuan, S. L. M. Teo, and P. A. Todd, The Ecological Significance of Giant Clams in Coral Reef Ecosystems, Biol. Conserv. **181**, 111 (2015).

[114] M. E. Rumpho, J. M. Worful, J. Lee, K. Kannan, M. S. Tyler, D. Bhattacharya, A. Moustafa, and J. R. Manhart, Horizontal Gene Transfer of the Algal Nuclear Gene psbO to the Photosynthetic Sea Slug Elysia Chlorotica, PNAS **105**, 17867 (2008).

[115] A. A. Venn, J. E. Loram, and A. E. Douglas, Photosynthetic Symbioses in Animals, J. Exp. Biol. **59**, 1069 (2008).

[116] C. Molnar and J. Gair, *Concepts of Biology - 1st Canadian Edition* (BCcampus, 2019).

[117] E. H. Harris, *The Chlamydomonas Sourcebook: Introduction to Chlamydomonas and Its Laboratory Use* (Academic Press, 2009).

[118] D. Sahoo and P. Baweja, General Characteristics of Algae, in *The Algae World*, edited by D. Sahoo and J. Seckbach (Springer Netherlands, 2015) p. 3.

[119] Green Algae Chase Light With The Help Of 'Eyespots', https://www.asianscientist.com/2016/05/in-the-lab/chlamydomonas-reinhardtii-algae-eyespots-phototaxis/ (2016).

[120] V. G. Bruce, The Biological Clock in Chlamydomonas Reinhardi, J. Protozool. **17**, 328 (1970).

[121] S. Sasso, H. Stibor, M. Mittag, and A. R. Grossman, From Molecular Manipulation of Domesticated Chlamydomonas Reinhardtii to Survival in Nature, eLife **7**, e39233 (2018).

[122] J. Beardall, A. Quigg, and J. A. Raven, Oxygen Consumption: Photorespiration and Chlororespiration, in *Photosynthesis in Algae*, edited by A. W. D. Larkum, S. E. Douglas, and J. A. Raven (Springer Netherlands, 2003) p. 157.

[123] T. Bosak, B. Liang, M. S. Sim, and A. P. Petroff, Morphological Record of Oxygenic Photosynthesis in Conical Stromatolites, PNAS **106**, 10939 (2009).

[124] L. O. Björn, G. C. Papageorgiou, R. E. Blankenship, and n. Govindjee, A Viewpoint: Why Chlorophyll a? Photosyn. Res. **99**, 85 (2009).

[125] A. A. Tandara and T. A. Mustoe, Oxygen in Wound Healing—More than a Nutrient, World J. Surg. **28**, 294 (2004).

[126] M. N. Chávez, T. L. Schenck, U. Hopfner, C. Centeno-Cerdas, I. Somlai-Schweiger, C. Schwarz, H.-G. Machens, M. Heikenwalder, M. R. Bono, M. L. Allende, J. Nickelsen, and J. T. Egaña, Towards Autotrophic Tissue Engineering: Photosynthetic Gene Therapy for Regeneration, Biomaterials **75**, 25 (2016).

[127] Dittmer and Grebe, *Handbook of Circulation. Analysis and Compilation by Philip L. Altman. Dorothy S. Dittmer and Rudolph M. Grebe, Eds. Saunders, Philadelphia, Pa., 1959. Xv + 393 Pp. Paper*, Vol. 59 (Saunders, 1960).

[128] Unisense, Oxygen Sensor User Manual, (2014).

[129] J. Neupert, D. Karcher, and R. Bock, Generation of Chlamydomonas Strains That Efficiently Express Nuclear Transgenes, Plant J. **57**, 1140 (2009).

[130] A. Chang, M. Chang, P. Feng, J. Khural, T. Luo, J. McCarthy, C. Mekelburg, K. Nadig, C. Perry, S. Thaper, R. Urbanski, P. Vohra, C. Weber, and J. Wong, *Characterization and Analysis of the Exogenous Application of Selected Phytohormones on C. Reinhardtii Metabolism*, Ph.D. thesis, University of Maryland (2011).

[131] C. E. D. Limited, CED Spike2, http://ced.co.uk/de/products/spkovin.

[132] S. Özugur, L. Kunz, and H. Straka, Relationship between Oxygen Consumption and Neuronal Activity in a Defined Neural Circuit, BMC Biology **18**, 76 (2020).

[133] G. P. Davey, S. Peuchen, and J. B. Clark, Energy Thresholds in Brain Mitochondria Potential Involvement in Neurodegeneration, J. Biol. Chem. **273**, 12753 (1998).

[134] A. Ivanov and Y. Zilberter, Critical State of Energy Metabolism in Brain Slices: The Principal Role of Oxygen Delivery and Energy Substrates in Shaping Neuronal Activity, Front. Neuroenerg. **3** (2011), 10.3389/fnene.2011.00009.

[135] M. S. Hedrick and R. E. Winmill, Excitatory and Inhibitory Effects of Tricaine (MS-222) on Fictive Breathing in Isolated Bullfrog Brain Stem, Am. J. Physiol. Regul. Integr. Comp. Physiol. **284**, R405 (2003).

[136] L. M. Palmer and A. F. Mensinger, Effect of the Anesthetic Tricaine (MS-222) on Nerve Activity in the Anterior Lateral Line of the Oyster Toadfish, Opsanus Tau, J. Neurophysiol. **92**, 1034 (2004).

[137] B. Trattner, C. M. Gravot, B. Grothe, and L. Kunz, Metabolic Maturation of Auditory Neurones in the Superior Olivary Complex, PLOS ONE **8**, e67351 (2013).

[138] F. Hyder, D. L. Rothman, and M. R. Bennett, Cortical Energy Demands of Signaling and Nonsignaling Components in Brain Are Conserved across Mammalian Species and Activity Levels, Proc Natl Acad Sci USA **110**, 3549 (2013).

[139] A. Scholz, Mechanisms of (Local) Anaesthetics on Voltage-Gated Sodium and Other Ion Channels, British Journal of Anaesthesia **89**, 52 (2002).

[140] S. Attili and S. M. Hughes, Anaesthetic Tricaine Acts Preferentially on Neural Voltage-Gated Sodium Channels and Fails to Block Directly Evoked Muscle Contraction, PLoS ONE **9**, e103751 (2014).

[141] J. Scholz and C. J. Woolf, Can We Conquer Pain? Nature Neuroscience **5**, 1062 (2002).

[142] K. Masamoto, J. Kershaw, M. Ureshi, N. Takizawa, H. Kobayashi, K. Tanishita, and I. Kanno, Apparent Diffusion Time of Oxygen from Blood to Tissue in Rat Cerebral Cortex: Implication for Tissue Oxygen Dynamics during Brain Functions, J. Appl. Physiol. **103**, 1352 (2007).

[143] E. Engl, R. Jolivet, C. N. Hall, and D. Attwell, Non-Signalling Energy Use in the Developing Rat Brain, J. Cereb. Blood Flow Metab. **37**, 951 (2017).

[144] F. Xu, Y. Ge, and H. Lu, Noninvasive Quantification of Whole-Brain Cerebral Metabolic Rate of Oxygen (CMRO2) by MRI, Magn. Reson. Med. **62**, 141 (2009).

[145] H.-J. Kretschmann, *Brain Growth* (Karger Medical and Scientific Publishers, 1986).

[146] N. Offenhauser, K. Thomsen, K. Caesar, and M. Lauritzen, Activity-Induced Tissue Oxygenation Changes in Rat Cerebellar Cortex: Interplay of Postsynaptic Activation and Blood Flow, J. Physiol. **565**, 279 (2005).

[147] T. Takano, G.-F. Tian, W. Peng, N. Lou, D. Lovatt, A. J. Hansen, K. A. Kasischke, and M. Nedergaard, Cortical Spreading Depression Causes and Coincides with Tissue Hypoxia, Nat. Neurosci. **10**, 754 (2007).

[148] M. E. Feder and W. W. Burggren, *Environmental Physiology of the Amphibians* (University of Chicago Press, 1992).

[149] D. J. Nelson and E. M. Wright, The Distribution, Activity, and Function of the Cilia in the Frog Brain, J. Physiol. **243**, 63 (1974).

[150] K. Mogi, T. Adachi, S. Izumi, and R. Toyoizumi, Visualisation of Cerebrospinal Fluid Flow Patterns in Albino Xenopus Larvae in Vivo, Fluids and Barriers of the CNS **9**, 9 (2012).

[151] G. Nilsson, Brain and Body Oxygen Requirements of Gnathonemus Petersii, a Fish with an Exceptionally Large Brain, J. Exp. Biol. **199**, 603 (1996).

[152] L. P. Folkow, J.-M. Ramirez, S. Ludvigsen, N. Ramirez, and A. S. Blix, Remarkable Neuronal Hypoxia Tolerance in the Deep-Diving Adult Hooded Seal (Cystophora Cristata), Neurosci. Lett. **446**, 147 (2008).

[153] J. P. O'Reilly, C. Jiang, and G. G. Haddad, Major Differences in Response to Graded Hypoxia between Hypoglossal and Neocortical Neurons, Brain Res. **683**, 179 (1995).

[154] Y. Haraguchi, Y. Kagawa, K. Sakaguchi, K. Matsuura, T. Shimizu, and T. Okano, Thicker Three-Dimensional Tissue from a "Symbiotic Recycling System" Combining Mammalian Cells and Algae, Sci. Rep. **7**, 1 (2017).

[155] M. Akimoto, H. Yamada, K. Ohtaguchi, and K. Koide, Photoautotrophic Cultivation of the Green Alga Chlamydomonas Reinhardtii as a Method for Carbon Dioxide Fixation and α-Linolenic Acid Production, J. Amer. Oil. Chem. Soc. **74**, 181 (1997).

[156] A. Lametschwandtner and B. Minnich, Microvascular Anatomy of the Brain of the Adult Pipid Frog, Xenopus Laevis (Daudin): A Scanning Electron Microscopic Study of Vascular Corrosion Casts, J. Morphol. **279**, 950 (2018).

[157] A. Melis, Solar Energy Conversion Efficiencies in Photosynthesis: Minimizing the Chlorophyll Antennae to Maximize Efficiency, Plant Sci. **177**, 272 (2009).

[158] E. Sanz-Luque, A. Chamizo-Ampudia, A. Llamas, A. Galvan, and E. Fernandez, Understanding Nitrate Assimilation and Its Regulation in Microalgae, Front. Plant Sci. **6** (2015), 10.3389/fpls.2015.00899.

[159] G. Peltier and L. Cournac, Chlororespiration, Annual Review of Plant Biology **53**, 523 (2002).

[160] D. J. Lea-Smith, P. Bombelli, R. Vasudevan, and C. J. Howe, Photosynthetic, Respiratory and Extracellular Electron Transport Pathways in Cyanobacteria, Biochimica et Biophysica Acta (BBA) - Bioenergetics **1857**, 247 (2016).

[161] TechniScience, Optischer Sensor Für Gelösten Sauerstoff (ODO-BTA), https://www.techniscience.com/de/cmsdata/mediabrowser/files/vernier%20duitse%20handleidingen/sensor%20fur%20sauerstoff%20optisch%20odo-bta.pdf (2013)

Acknowledgments/Danksagungen

First of all, I would like to thank my supervisor Prof. Hans Straka for the opportunity to do my PhD on such a fascinating project in his lab. Thank you for the countless discussions, advice, and your help when ever needed. Also a big thanks for the possibility to participate in all the conferences, workshops, and my research stay in the Boston.

A big thanks also to PD Lars Kunz for the fruitful discussions right from the beginning of my PhD. And thanks for reviewing my thesis.

I would also like to thank my TAC commitee, Prof. Hans Straka, PD Lars Kunz, Prof. Marianne Dieterich, and Dr. Martin Stemmler for their input to my project, and to Prof. Ansgar Büschges for reviewing my thesis.

A great thank you to Prof. Jörg Nickelsen and Dr. Myra Chávez for a very successful and fruitful collaboration and for the scientific discussions that helped me to interpret my results. Thank you Myra for the fun time during the algae project and for providing the microorganisms anytime we needed them.

Thank you to my lab members—former and current—for all the support and feedback. A big thank you Clayton for the fun trips to conferences, especially for accompanying me on my first trip to the US.

A great thank you Klara and Veronika for all the mental support especially during the last part of my PhD. It was always fun to grab a coffee. Thank you for always being there, having time for a chat, and making work so enjoyable.

Further, a big thanks to my office colleagues Yannik, Eli, and Zhizi who always pushed my mood, helped me whenever I had issues with my computer or questions concerning python.

Further, a special thanks to Prof. Lisa Goodrich for the opportunity to join your lab for a research stay. Thank you for all the support and advice, for the fun and heart-warming moments also outside the lab. It was a great experience that I would not have missed.

I would also like to thank to Dr. Roberto Banchi and Dr. Babak Azimifar from MAVIG GmbH for their help in taking images of the brain blood vessels and Matthias Gaenge from Carl Zeiss Microscopy GmbH for his help in taking detailed images of blood vessels, imaging a full brain, and running calculations.

A grateful thanks to the animal housekeeping for taking care of our frogs and tadpoles and always being up for a chat. Further, I want to thank the mechanical workshop of the Biocenter Martinsried for their help in assembling parts of the setup.

A big thanks to the GSN for all the great opportunities in workshops guiding through my PhD and developing myself. Financial support throughout my PhD, provided by GSN, IFB (01 EO 0901), and SFB 870 (B12), is acknowledged.

Last but not least, a herzlichs Dankschee an meine Familie und Freind, de mi in dea turbulendn Zeid unterstützt hom. Measse fia de wohltuendn Woate de i gebraucht hob wenn i Zwoafl kabd hob. Gejts God an Oma und Opa für de ohoidende Begeisterung und Unterstützung. Dankschee fia de finanzielle Unterstützung Mama und Babba, ohne eich waarad i heid ned an dem Punkt und voaoiem ned da Mensch da i bin. Und a oia liabsts Dankschee an Steffen, der mia üba Nah und Fean so unterstützt hod wia koa andera. Measse dia fia ois!